Investigation of platinum-free ORR catalysts at agglomerate scale : from local probe characterizations to modeling studies

Alice Boudet

université PARIS-SACLAY

Investigation of platinum-free ORR catalysts at agglomerate scale: from local probe characterizations to modeling studies

Étude à l'échelle de l'agglomérat de catalyseurs sans platine pour l'ORR : caractérisations à sonde locale et modélisation en pile

Thèse de doctorat de l'université Paris-Saclay

École doctorale n° 571 : Sciences chimiques : molécules, matériaux, instrumentation et biosystèmes (2MIB)
Spécialité de doctorat : Chimie
Unité de recherche : Université Paris-Saclay, CEA, CNRS, NIMBE, 91191, Gif-sur-Yvette, France
Référent : Faculté des sciences d'Orsay

Thèse présentée et soutenue à Paris-Saclay, le 20/10/2021, par

Alice BOUDET

Composition du Jury

Hynd REMITA Directrice de recherche, Université Paris-Saclay (LCP)	Présidente
Jonathan DESEURE Maître de conférences (HDR), Université Grenoble Alpes (LEPMI)	Rapporteur et Examinateur
Mathieu ETIENNE Directeur de recherche, CNRS (LCPME)	Rapporteur et Examinateur
Gaël MARANZANA Professeur, Université de Lorraine (LEMTA)	Examinateur

Direction de la thèse

Bruno JOUSSELME Chercheur, CEA (NIMBE, LICSEN)	Directeur de thèse
Renaud CORNUT Chercheur, CEA (NIMBE, LICSEN)	Co-directeur de thèse

Thèse de doctorat

NNT : 2021UPASF037

Remerciements

Ce manuscrit marque l'achèvement de trois années de thèse réalisées au sein du Laboratoire d'Innovation en Chimie des Surfaces et Nanosciences (LICSEN) du Commissariat à l'Energie Atomique et aux Energies Alternatives (CEA). Ces trois années ont été une belle aventure, tant sur le plan humain que scientifique, notamment grâce aux nombreuses personnes que j'ai pu côtoyer au CEA et ailleurs. Je tiens ici à remercier tous ceux qui ont contribué, de près ou de loin, à l'accomplissement de cette thèse.

Je remercie tout d'abord les membres de mon jury de thèse pour avoir pris le temps d'examiner mes travaux. La multidisciplinarité de ce jury a permis de générer des discussions très intéressantes lors de la soutenance et c'était un plaisir de pouvoir échanger sur mes travaux avec des chercheurs aux profils si différents. Merci à Hynd Remita d'avoir accepté de présider ce jury et merci à Jonathan Deseure et à Mathieu Etienne d'avoir accepté d'être les rapporteurs de ce manuscrit. Un grand merci à Gaël Maranzana dont j'ai apprécié la curiosité qui a grandement enrichi la discussion lors de la soutenance.

Que serait une thèse sans l'aide inconditionnelle apportée par les encadrants ? Merci à Bruno Jousselme et Renaud Cornut de m'avoir accompagnée tout au long de ces trois ans dans mon apprentissage du métier de chercheuse. Merci à toi Renaud de m'avoir enseigné toutes les ficelles du métier, de la SECM à la modélisation, en passant par la rhétorique pour « se vendre » dans le milieu professionnel. Ta culture et ta vivacité intellectuelle rendent chaque conversation avec toi extrêmement intéressante. Merci d'avoir toujours su te rendre disponible pour répondre à mes questions, et ce malgré tes très nombreuses occupations qui faisaient que les conversations commençaient souvent par une course poursuite effrénée dans le labo pour avoir ton attention, ce qui me faisait beaucoup rire. Merci également à toi Bruno pour ta bonne humeur permanente, ton calme, ta pédagogie et ta disponibilité. Mon sujet était parfois un peu éloigné de ton domaine d'expertise mais tu as toujours été présent pour donner des remarques très pertinentes. Merci à tous les deux pour la confiance que vous accordez à vos doctorants et l'autonomie que vous leur laissez.

Je tiens également à remercier Frédéric Oswald, avant-dernier chercheur permanent arrivé au LICSEN, qui s'est bien intégré dans le duo formé par Renaud et Bruno et dont la participation aux réunions concernant ma thèse a permis d'apporter un point de vue supplémentaire aux riches discussions qui pouvaient durer tout un après-midi.

Je remercie Joël Pauchet et Pascal Schott du CEA de Grenoble pour leur expertise du modèle EuROPIUM que j'ai utilisé pour mes travaux de modélisation en pile.

Merci aux membres du projet européen PEGASUS, et notamment à son coordinateur Pierre-André Jacques. Il était très intéressant pour moi de pouvoir inscrire mes travaux dans une perspective plus globale apportée par ce projet. Les réunions organisées à Madrid, à la Grande-Motte, puis en visioconférence m'ont permis de rencontrer et d'avoir des échanges très intéressants avec des chercheurs venant de toute l'Europe.

On se sent parfois seul devant la complexité de la SECM. Heureusement, j'ai pu partager mes questions et plus tard mon expérience avec d'autres étudiants au sujet proche du mien. Merci à Olivier Henrotte pour avoir mis en place les premières briques du protocole expérimental. Même si tu avais déjà quitté le CEA à mon arrivée, nos échanges de mails m'ont permis de prendre en main au mieux cette machine capricieuse. I switch in English to thank Ndrina Limani, even if I kwow that your French is much better than what you affirm 😉. Thank you for your patience while I was teaching you a protocol that I did not yet master completely. It was a pleasure to collaborate with you and I learnt from you as much as you learnt from me. Now you are the master of the SECM and I wish you all the best for the end of your PhD!

Je remercie chaleureusement Estelle Romeuf, ma première stagiaire grâce à qui j'ai pu découvrir et apprécier l'expérience d'encadrement. Tu étais une stagiaire intéressée, réactive et sympathique et j'ai apprécié te recroiser durant ton alternance.

Merci à Serge Palacin, directeur du NIMBE, et Vincent Derycke, responsable du LICSEN, pour leur accueil et leur disponibilité. Merci à Céline Delobel, secrétaire du NIMBE, pour sa réactivité et son efficacité dans toutes les tâches administratives. Merci à Thierry Bernard, mécanicien, à qui je dois la fabrication et le SAV du dispositif de dépôt des catalyseurs. Sa sympathie, sa créativité et son talent en font un atout essentiel pour le NIMBE.

Je remercie également les personnels de l'infogérence EXTRA et INTRA qui m'ont donné les moyens de travailler en collaboration avec le CEA de Grenoble, puis qui ont rendu possible le télétravail lors de la crise sanitaire. Merci en particulier à Sylvie Jubera qui a permis d'accélérer les nombreuses et complexes démarches pour me donner accès aux serveurs nécessaires à ma thèse.

Merci à toutes les autres personnes ayant partagé mon quotidien durant ces trois années. Les permanents, toujours disponibles pour un coup de main, un conseil, ou simplement pour discuter : Guy Deniau, Fanny Hauquier, Ariana Filoramo, Maud Fayos, Nabila Debou, Jocelyne Leroy, Pascal Viel, Stéphane Campidelli, Géraldine Carrot, Philippe Surugue et Jean-Christophe Gabriel. Merci également à tous les non-permanents dont j'ai croisé le chemin plus ou moins longtemps durant cette thèse. Je pense tout d'abord à Gaëlle Charrier et à Aurélien Doublet qui m'ont accueillie au bâtiment 131, temple de la SECM isolé et vétuste mais avec une

ambiance sans pareille ! Avec Fatima El Orf, nous formions une équipe de choc, soudée par les sorties restos à midi et la tradition de la « musique du jour » qui nous a permis de confronter nos goûts souvent très différents. Merci aux thésards et CDD du 466, Sarah Bernardi, Thomas Petenzi, Florian Lebon, Robin Dürr, Julie Machado, Cédric Zobrist, puis plus tard Nicolas Blanchard, Lina Cherni, Yuemin Deng, et tout récemment Alexandre Pistol. C'était un plaisir de partager des repas avec vous, de temps en temps des cafés, et même de m'intégrer dans le bureau du rez-de-chaussée pour mes derniers mois de thèse. Le 125 est malheureusement plus loin, mais ça ne m'a pas empêchée d'apprécier les différents thésards qui s'y sont succédés : Kévin Jaouen, Manel Hanana, Hanine Kamaleddine, Joffrey Pijeat, Marta Reig, puis Nathan Ullberg et Daniel Medina-Lopez. J'espère pouvoir tous vous recroiser à l'emblématique repas de Noël du LICSEN.

Ces trois ans n'ont pas été composés que de science et heureusement ! La musique occupe en effet une grande place dans ma vie et je remercie toutes les personnes que j'ai rencontrées durant cette thèse et avec qui j'ai partagé de précieux moments musicaux, essentiels à mon équilibre : l'orchestre symphonique du COGE, Vital Chauve, Emma Crochet et Philippe Duême pour l'association des Clefs d'Orsay, ainsi que Haï Son Lê.

Je remercie également l'ensemble de ma famille et belle-famille qui a pu faire le déplacement à ma soutenance. Cette cérémonie a été l'occasion pour vous de comprendre un peu plus le monde étrange des chercheurs dans lequel j'évolue, et j'ai été ravie de voir que ma maman a enfin saisi le concept de catalyseur ! Vous avoir tous à Saclay pour cette journée n'a pas été facile à organiser, mais vous avez réussi et nous avons pu partager un merveilleux repas polonais réunissant pour la première fois en six ans de relation mes deux parents et mes deux beaux-parents. Merci également à mes frères et à ma sœur pour votre présence dans ma vie. Vous êtes les personnes avec qui j'ai grandi et chaque moment passé avec vous est précieux. Au cours de ces trois ans, je vous ai vu vous épanouir chacun dans votre domaine, et vous avez même atteint certaines étapes de la vie avant votre grande sœur (CDI, achat immobilier). Bravo à vous quatre, je suis fière de vous !

Enfin, je remercie de tout mon cœur Maxence Dauphin, qui m'accompagne et me supporte depuis six ans. C'est toi qui étais en première ligne dans les moments les plus difficiles et tu as toujours su me soutenir. Je ne te remercierai jamais assez pour tout ce que tu m'apportes au quotidien, tes câlins, ton humour et ton amour. C'est en pensant à toi que je mets un point final à ce manuscrit, en t'envoyant tous mes encouragements pour que tu viennes à bout du tien. Tu verras, un jour on se retrouve docteur et c'est vachement bien !

Notations

AFM	Atomic Force Microscopy
BDD	Boron doped diamond
BEV	Battery Electric Vehicle
CCM	Catalyst Coated Membrane
CEA	Commissariat à l'Energie Atomique et aux Energies Elternatives
CL	Catalyst Layer
CT	Computed Tomography
CV	Cyclic Voltammetry
DLS	Dynamic Light Scattering
EDX	Energy Dispersive X-ray Spectroscopy
EIS	Electrochemical Impedance Spectroscopy
EuROPIUM	ElectRochemistry OPtImization Understanding Modeling
FCEV	Fuel Cell Electric Vehicle
FCH JU	Fuel Cells and Hydrogen Joint Undertaking
FOV	Field Of View
GDE	Gas Diffusion Electrode
GDL	Gas Diffusion Layer
H_2	Dihydrogen
H_2O_2	Hydrogene Peroxide
HER	Hydrogen Evolution Reaction
HOR	Hydrogen Oxidation Reaction
LICSEN	Laboratory of Innovation in Surface Chemistry and Nanosciences
LITEN	Laboratoire d'Innovation pour les Technologies des Energies Nouvelles et les Nanomatériaux
LSV	Linear Sweep Voltammetry
MEA	Membrane Electrode Assembly
MOF	Metal Organic Framework
MPL	Microporous Layer
O_2	Dioxygen
OER	Oxygen Evolution Reaction
ORR	Oxygen Reduction Reaction

PANI	Polyaniline
PEGASUS	PEMFC based on platinum Group metAl free StrUctured cathodeS
PEMFC	Proton Exchange Membrane Fuel Cell
PGM	Platinum Group Metal
Pt	Platinum
RC	Redox Competition (mode of SECM)
RDE	Rotating Disk Electrode
RH	Relative Humidity
RRDE	Rotating Ring Disk Electrode
SCE	Saturated Calomel Electrode
SECCM	Scanning Electrochemical Cell Microscopy
SECM	Scanning ElectroChemical Microscopy
SEI	Solid electrolyte interface
SEM	Scanning Electron Microscopy
SG-TC	Substrate Generation-Tip Collection (mode of SECM)
SICM	Scanning Ion Conductance Microscopy
TEM	Transmission Electron Microscopy
TG-SC	Tip Generation-Substrate Collection (mode of SECM)
UME	Ultramicroelectrode

Contents

Synthèse en français

La transition énergétique, indispensable à la diminution des émissions de gaz à effet de serre par nos sociétés, demande d'importants changements technologiques pour décarboner les secteurs les plus polluants. Dans le secteur des transports, les véhicules électriques à pile à combustible font partie des solutions envisagées pour remplacer les véhicules thermiques actuels. En effet, même si cette technologie est moins mature que les véhicules électriques à batterie, la grande autonomie des véhicules à pile à combustible, leur poids moins important et la rapidité du remplissage des réservoirs à hydrogène sont des atouts qui rendent cette technologie attractive pour certaines applications comme le transport de fret ou pour des véhicules utilisés de manière intensive (transports en commun, livraison, etc.). Cependant, le coût des piles à combustible reste un frein majeur à leur développement. Ce coût est principalement dû au platine utilisé comme catalyseur des réactions électrochimiques. De nouveaux matériaux catalytiques sont donc développés pour remplacer le platine et réduire les coûts des piles à combustible à membrane échangeuse de protons (PEMFC). Ces matériaux, plus abordables mais moins actifs que le platine, sont intégrés en grande quantité dans les couches catalytiques des piles afin d'atteindre les performances requises pour une application automobile. De nouvelles problématiques font alors leur apparition, concernant notamment le transport des espèces électroactives au sein des couches catalytiques. En effet, la mise en forme de ces couches est essentielle pour garantir l'accès des réactifs aux sites catalytiques et assurer l'évacuation de l'eau produite par la réaction. L'agglomérat est la structure clé de ces problématiques de transport. Sa taille et sa composition vont influer grandement sur les performances globales de la pile.

Dans cette thèse, nous proposons d'étudier des catalyseurs sans platine pour la réduction de l'oxygène (ORR) à l'échelle de l'agglomérat, en apportant des outils permettant de caractériser finement ces structures et leur impact sur l'activité catalytique du matériau.

Dans un premier temps, un protocole expérimental a été développé pour étudier un dépôt d'agglomérats à l'aide de deux techniques de caractérisation à sonde locale : la microscopie électrochimique à balayage (SECM) qui donne accès à l'activité catalytique du dépôt, et la microscopie à force atomique (AFM) qui mesure son état d'agglomération. Nous avons pu, grâce à ce protocole, expliquer des différences d'activité catalytique par un état d'agglomération différent des dépôts. Le protocole a été appliqué à plusieurs catalyseurs sans platine développés dans le cadre du projet européen PEGASUS, et nous avons pu identifier, pour chaque catalyseur, la contribution de l'activité intrinsèque du matériau et celle de l'état d'agglomération du dépôt. Nous avons montré que l'effet de l'agglomération est prédominant sur l'activité intrinsèque du

catalyseur, même à très bas chargement (quelques dizaines de microgrammes par centimètre carré). Cette étude a également permis de mettre en évidence les comportements très variables des différents matériaux face à une formulation d'encre et un protocole de dépôt identiques. Ceci souligne l'importance du travail de mise en forme des couches catalytique qui doit être optimisé pour chaque matériau afin d'en tirer les meilleures performances en pile.

Le protocole expérimental développé dans cette thèse donnant accès à l'activité intrinsèque des catalyseurs, une méthode pour extraire des paramètres cinétiques à partir des mesures SECM et à l'aide d'un modèle numérique a été mise en place. La densité de courant d'échange et la sélectivité d'un catalyseur ont été déterminées et comparées à la littérature. Une résistance ohmique entraînant d'importantes pertes de performance a été mise en évidence et interprétée comme un phénomène local de chute ohmique à l'intérieur des agglomérats, pouvant provenir de résistances de contact entre les agglomérats et le substrat.

Finalement, un modèle numérique de pile à combustible a été développé afin d'étudier les paramètres d'agglomérat et de couche active influençant les performances globales en pile. Les paramètres cinétiques déterminés à partir des mesures SECM ont été inclus dans le modèle. Ce modèle a été utilisé pour simuler différentes structures de couche catalytique et d'agglomérat et confirme l'importance de contrôler l'agglomération du catalyseur pour optimiser les performances d'une pile à combustible.

Cette thèse a donc permis d'étudier, expérimentalement et à l'aide de modèles numériques, l'influence de l'état d'agglomération de catalyseurs sans platine pour l'ORR sur leur activité électrochimique. Les différentes études réalisées soulignent l'importance du travail de mise en forme des catalyseurs pour obtenir des performances optimales. Le protocole de caractérisation mis en place ouvre le champ à de nombreuses études pour approfondir la compréhension des agglomérats et leur impact sur les performances d'un matériau électrocatalytique.

Introduction

The fuel cell is a technology that converts hydrogen and oxygen into electricity without any greenhouse gas emission. Its development in the sector of transportation is foreseen to be a part of the solution for the replacement of the current 800 million of thermal vehicles with non emitting ones. Policy makers all around the world are trying to accelerate the market introduction of the fuel cell electric vehicles, notably by involving the scientific community in order to overcome the last techno-economic barriers. In Europe, the Fuel Cells and Hydrogen Joint Undertaking (FCH JU) [1] gathers the European Commission, fuel cells and hydrogen industries and the research community. Several projects are financed by the FCH JU in order to develop efficient solutions for the development of fuel cells and hydrogen-based technologies.

In this context, the PEGASUS project (PEMFC based on platinum Group metAl free StrUctured cathodeS) [2] involves several academic and industrial partners across Europa and aims at developing a new generation of proton exchange membrane fuel cells (PEMFC) based on platinum group metal (PGM) free catalysts. Indeed, 50 % of the cost of current fuel cells comes from the catalyst material [3]. This catalyst is based on platinum metal, which is an expensive and scarce resource. The PEGASUS project aims at combining the skills of research institutes and fuel cells companies for developing high performance, durable and low-cost fuel cells based on PGM-free catalysts. While some of the partners focus on synthesis strategies of catalytic materials and their integration in single cell PEMFC, other partners aim at developing characterization techniques and test protocols adapted to this new type of materials.

This thesis fits into this last objective and aims at investigating the link between the structural properties and the electrocatalytic activity of materials developed within the PEGASUS project. An experimental methodology based on local probe techniques (SECM and AFM) has been developed and coupled with numerical modeling in order to study catalysts at agglomerate scale and extract intrinsic kinetic parameters. Then, the relationship between the structure and the activity of the materials is investigated through a modeling approach at single PEMFC cell scale including the kinetic parameters determined with the SECM and AFM based technique.

The first chapter discusses the main challenges concerning the development of fuel cells based on PGM-free catalysts. The various morphologies of the materials developed nowadays lead to issues for their formulation into catalytic layers, as well as for the characterization of their intrinsic properties.

The second chapter presents the experimental methodology developed in this thesis in order to characterize PGM-free catalysts at agglomerate scale. Two local probe techniques, scanning electrochemical microscopy (SECM) and atomic force microscopy (AFM) are combined in order to link the activity of the catalysts to their agglomeration state. Several catalysts developed by partners of the PEGASUS project are investigated with this technique.

The third chapter develops a numerical modeling approach of the SECM set-up in order to extract kinetic parameters from the SECM and AFM measurements. The exchange current density and the selectivity of a PGM-free catalyst developed in the LICSEN are determined. Local ohmic drop at the catalyst agglomerates is observed and quantified.

The fourth chapter aims at studying the relationship between the structure and the activity of PGM-free materials at the single cell scale, by performing numerical simulations of a membrane electrode assembly (MEA). An agglomerate model including the kinetic parameters determined with SECM and AFM is developed. The effects of the structure and composition of the catalyst layer are investigated with the model.

This thesis was conducted in the Laboratory of Innovation in Surface Chemistry and Nanosciences (LICSEN) in the CEA-Saclay. This laboratory combines an expertise in the chemistry of nanomaterials for various applications, from health technologies to renewable energies. Synthesis of PGM-free catalysts for fuel cells [4] and SECM characterizations of materials [5], [6] are performed for years at the LICSEN by the teams of Bruno Jousselme and Renaud Cornut. Joël Pauchet and Pascal Schott from the LITEN in CEA-Grenoble participated also to the supervision of this work, especially on the MEA simulation part.

Chapter I

Challenges on the development of fuel cells based on PGM-free catalysts

This chapter aims at giving an overview on the current research trends on PGM-free fuel cells. After a brief discussion about the place of the fuel cell technology in the energetic transition, the PEMFC will be presented. The main issues associated to the development of PGM-free catalysts and their integration in efficient membrane electrode assemblies will be reviewed. The importance of the characterization techniques will be highlighted and the main techniques used to study PEMFC will be presented.

I.1. The role of hydrogen and fuel cells in the energetic transition

Limiting the global warming to 1.5 °C demands that the greenhouse gases emissions drop by 45 % by 2030 compared to 2010 levels [7]. To meet such a challenge, the way our society generates, transports, stores and consumes energy needs to face radical changes. New energy carriers need to be deployed in replacement to the usual fuels like petrol, coal or gas, which are the major contributors to the CO_2 emissions. Electricity is easily produced by various clean energy sources (solar energy, wind energy, nuclear energy or hydraulic energy…) and is already used to energize the majority of our equipment. Its transportation requires however complex infrastructures and the storage capacities are far below the requirements of a society based only on this energy carrier. Thus, hydrogen could represent an interesting solution for overcoming the limitations of electricity in some sectors. This fuel can be stored and transported in tanks, almost similarly to the usual fuels. Its combustion generates only water, which does not take part in the global warming. Moreover, hydrogen can be easily combined with electricity, since electrolyzers and fuel cells enable to convert these two energy carriers into another.

Figure 1 shows the breadth of the decarbonization challenge and the contribution hydrogen can bring to this decarbonization [8]. The main domain in which hydrogen can have a significant contribution to the reduction of carbon emissions is the transportation sector. 99 % of the vehicles in 2019 were based on combustion engines [9]. The wide development of electric vehicles is thus needed in order to decrease the carbon emissions as fast as possible. The battery electric vehicle (BEV) is currently the more mature technology but the long time of recharging and the limited travel range are restraining the attractiveness of these vehicles to the general population. Fuel cell electric vehicles (FCEV) are based on the utilization of gaseous hydrogen, which is converted to electricity along the car journey. The main advantages of FCEV over BEV are the longer travel range, the rapidity of refueling and the lighter weight of the vehicle. These vehicles are yet more expensive than BEV. This high cost limits for now the development of FCEV in the market of personal vehicles. However, their development is foreseen to have an interesting growth in the sector of utility vehicles, especially heavy ones like trains, trucks or buses, or vehicles that are used over long periods of time (delivery, transport, etc.).

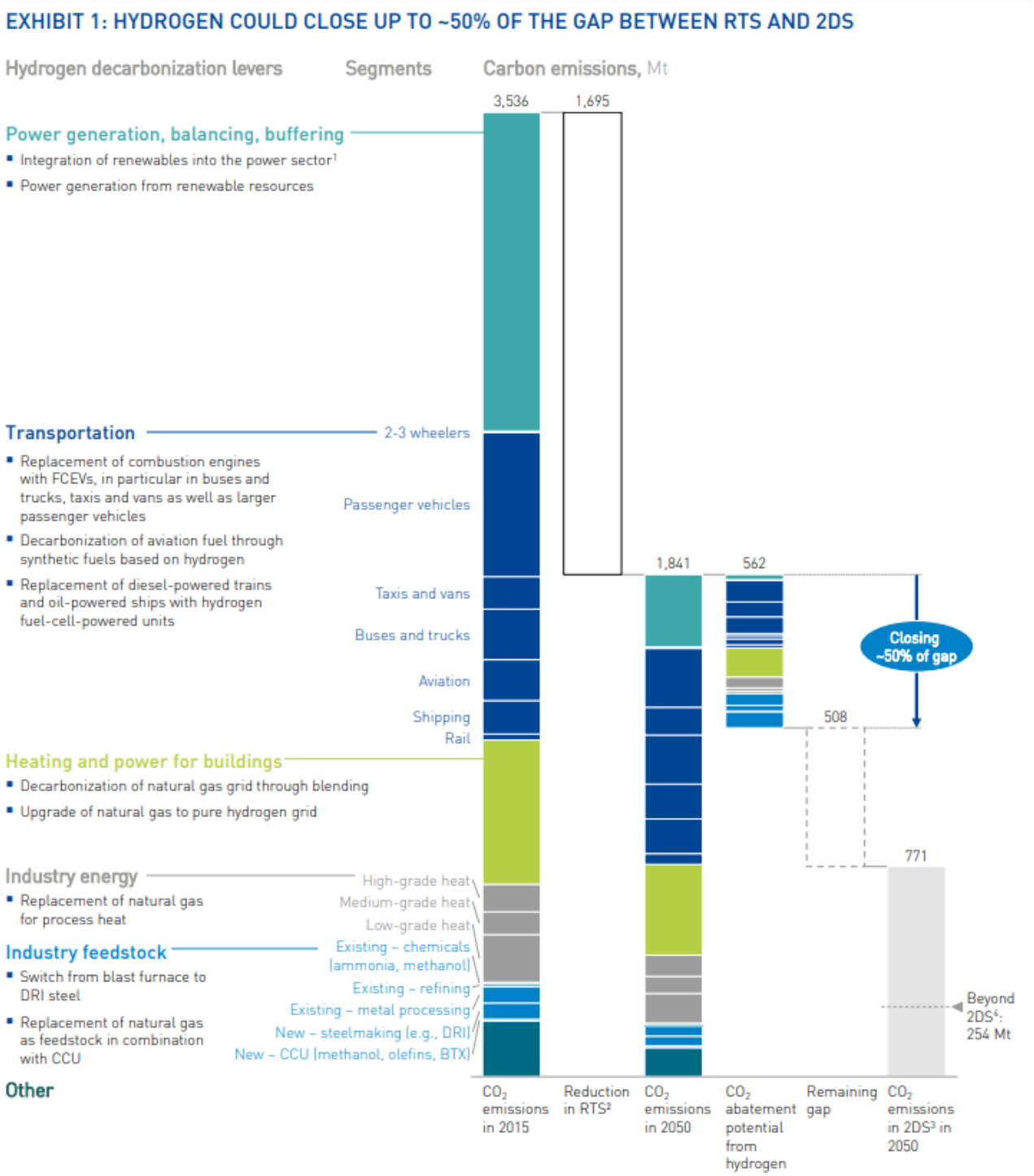

Figure 1: Hydrogen contribution in the decarbonization challenge. The first column depicts the carbon emissions in 2015, while the third column represents the objective of emissions in 2050 according to the commitments taken by countries during the Paris Agreement (Reference Technology Scenario). The fourth column shows the contribution of including hydrogen in the decarbonization process, and the sixth column represents the objectives of emissions for a 2 °C scenario and a 1.5 °C scenario. Figure taken from [8].

Fuel cells have also applications in other sectors such as stationary power sources for energy, or cogeneration in residential buildings for example. The cogeneration consists in using a fuel cell for producing both electricity and heat for a given application. The use of fuel cells in military and space domains is also very important since this was the first application of this technology in history. The NASA shuttles and the ISS are notably powered by alkaline fuel cells (AFC). In order to fulfill the requirements of the various applications of fuel cells, several systems are coexisting, with different power, operating temperature and start-up time. These systems are characterized by their fuel and their electrolyte. Table 1 presents the main existing systems. Among them, the proton exchange membrane fuel cell (PEMFC) is the best candidate for automotive application. This technology has been extensively studied by the scientific community over the last 30 years and will be presented in details in the following part.

Type of fuel cell	**Fuel**	**Electrolyte**	**System output (kW)**	**Operating temperature (°C)**	**Start-up time**	**Applications**
Alkaline fuel cell (AFC)	H_2	Aqueous solution of KOH	10-100	60-90	Few seconds	Military, space
Proton exchange membrane fuel cell (PEMFC)	H_2	Solid polymeric proton conductor	<1-250	60-100	Few seconds	Transportation, back-up power
Direct methanol fuel cell (DMFC)	Methanol	Solid polymeric proton conductor	<1-100	60-200	Few seconds	Transportation, back-up power
Phosphoric acid fuel cell (PAFC)	H_2	Phosphoric acid	50-1000	60-200	2-4 hours	Stationary power application, cogeneration
Solid oxide fuel cell (SOFC)	H_2, CO, CH_4	Yttria-stabilized zirconia	<1-3000	600-1000	> 10 hours	Stationary power application, cogeneration
Molten carbonate fuel cell (MCFC)	H_2, CO, CH_4	Molten Li_2CO_3, Na_2CO_3, K_2CO_3	<1-1000	600-700	> 10 hours	Stationary power application, cogeneration

Table 1: Characteristics of different fuel cell systems. Data taken from [10], [11].

I.2. The PEMFC technology and the challenges associated to its development

I.2.1. Presentation of the proton exchange membrane fuel cell

The operation of a PEMFC is based on two electrochemical reactions that occur in different places, leading to the generation of an electrical current. At the anode, hydrogen is decomposed into protons and electrons. The electrons pass to the electrical circuit while the protons are transported through the membrane into the cathode. At the cathode, oxygen reacts with the protons and electrons from the electrical circuit to form water. These reactions are formalized in the Eq. (1) and (2).

$$2\ H_2 \rightarrow 4\ H^+ + 4\ e^- \qquad (1)$$

$$O_2 + 4\ H^+ + 4\ e^- \rightarrow 2\ H_2O \qquad (2)$$

The global reaction over the full cell is thus :

$$2\ H_2 + O_2 \rightarrow 2\ H_2O \qquad (3)$$

Manufacturing a PEMFC consists in assembling different layers that aim at optimizing the encounter of the reactants. The bipolar plates (BP) collect the current and distribute the gases through their channels. The gas diffusion layers (GDL) serve to homogenize the repartition of the gases and evacuate the water produced by the reactions. They are composed of carbon fibers treated with a hydrophobic material in order to avoid the accumulation of water. The catalyst layers (CL) are the places where the electrochemical reactions occur. In addition to the reaction themselves, the layers have to ensure the transport of the reactants and products. Thus, the CL need to have good electronic and ionic conductivities, and a sufficient porosity to bring the gases and evacuate the water. The CL are generally composed of porous carbon particles supporting the catalyst and embedded in an ionomer, i.e. an ionic conductive polymer. This ionomer is often the same material than the membrane, which separates electrically the two electrodes while allowing the transport of protons. Nafion is the state-of-the-art material and is used in the majority of fuel cells nowadays. Figure 2 (a) presents the different layers of a PEMFC and Figure 2 (b) focuses on the complex architecture that need to be achieved in the catalyst layer.

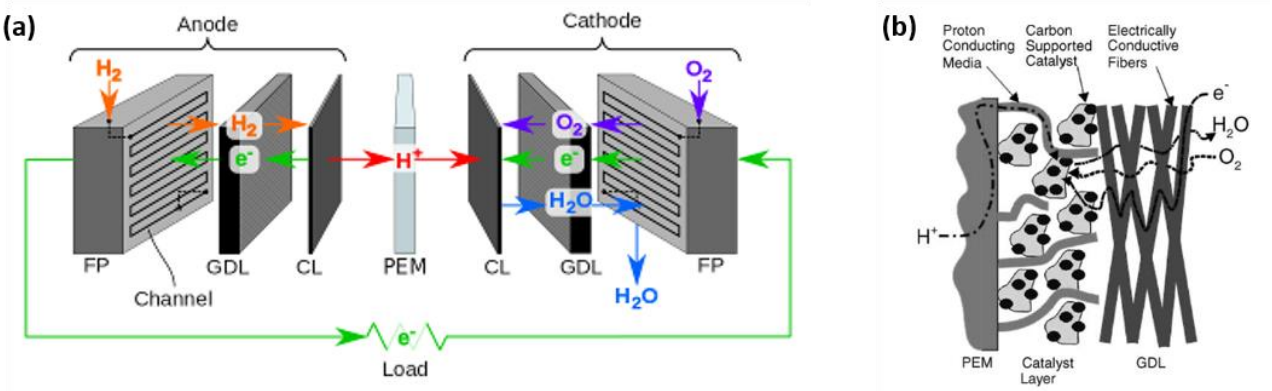

Figure 2: (a) Schematization of a PEMFC fuel cell. (b) Focus on the catalyst layer structure.

I.2.2. Towards the replacement of platinum in PEMFC

The electrocatalytic reactions in a PEMFC occur at the surface of a catalytic material added to the carbon phase. Platinum particles dispersed on a porous carbon material are the state-of-the-art catalysts for both the hydrogen oxidation reaction (HOR) presented in Eq. (1), and the oxygen reduction reaction (ORR) presented in Eq. (2). The HOR has rapid kinetics, hence a very low amount of platinum is needed at the anode (around 0.05 mg_{Pt}/cm^2 [12]). At the cathode however, the sluggish kinetics of ORR make the utilization of a larger amount of catalyst necessary (around 0.2 mg_{Pt}/cm^2). The high cost of this metal is the main reason why the PEMFC are so expensive, about 50 % of the costs in a PEMFC stack is due to the worth of platinum [3]. Moreover, this metal is rather scarce in the earth's crust and 71 % of the global production comes from South Africa. This can lead to strategical issues for the other countries. For all these reasons, the European commission is reporting since 2011 platinum group metals in the list of critical raw materials for strategic technologies [13]. Figure 3 shows the price and relative abundance of several metals used in catalysis, some of which are used in the strategies investigated to reduce the amount of platinum needed at the cathode, or even to replace it with other materials.

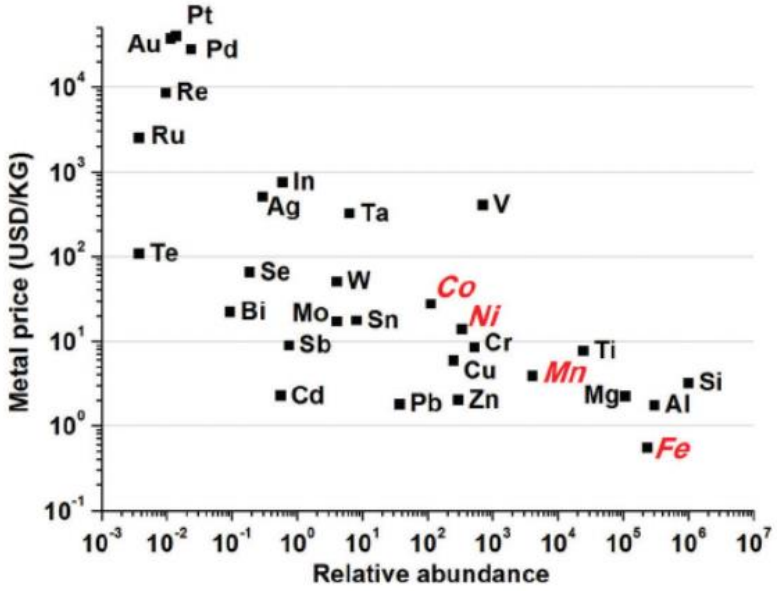

Figure 3: Relationship between the price and relative abundance in earth's crust of several metals used notably in catalysis. Figure taken from [14].

A first strategy consists in allowing platinum with other metals [15]. Noble metals like Ru, Au or Pd create a synergistic effect enhancing the catalytic activity and improving the tolerance of the catalyst to CO impurities [16]. Non-noble metals like Ni, Cu, Co or Fe enable to tune the structure of the material in order to improve the accessibility of the platinum sites. Core-shell structures [17], nanopolyhedra [18], nanodendrites [19], or hollow structures [20] have a high surface to volume ratio and expose a maximum of active sites to the ORR. Improving the support material can also lead to greater performance. For example, incorporating nitrogen into the carbon material modifies the catalyst electronic structure and enhances the performance [21]. However, at ultra-low loading of platinum, large performance losses are observed at high current density, preventing the further reduction of the amount of platinum [12].

The second strategy to get rid of the dependence on platinum and noble metals consists in developing platinum-group metal (PGM) free catalysts. The first materials were inspired by the natural enzymes able to perform the ORR, notably the cytochrome C oxidase whose active site is an iron porphyrine [22]. Jasisnki reported in 1964 the ORR activity in alkaline electrolyte of cobalt phtalocyanine [23]. In 1989, Gupta highlighted the importance of applying a heat-treatment to improve the activity of polyacrilonitrile-based catalysts containing Co and Fe [24]. Proietti from Dodelet's group developed in 2011 the first PGM-free catalyst nearing the performance of the Pt-based catalysts [25]. They notably highlighted the importance of the catalyst structure for the optimal accessibility of the active sites. Nowadays, the majority of the PGM-free catalysts for the ORR are based on transition metals (mainly Fe) coordinated with N atoms and mixed with a carbon matrix

before a heat-treatment under inert (N_2 or Ar) or active (H_2 or NH_3) atmosphere. The precursors are chosen in order to create a final material with an important microporosity. The active sites are indeed located in the micropores (1-2 nm) and their utilization depends on the accessibility of these pores. Several approaches are currently developed. Metal organic frameworks (MOF) such as ZIF-8 have an extremely high surface area and an important microporosity coupled with a substantial mesoporosity (2-50 nm), they constitute an ideal support for the active sites [26], [27]. The sacrificial support method consists in mixing the precursors with a sacrificial support material. This material is then removed by acid leaching and an open-pore structure is created. This method has been extensively used by Atanassov's group [28], [29], [30]. An additional method developed by Zelenay's group consists in using dual nitrogen precursors such as polyaniline (PANI) and cyanamide (CM). The latter undergoes a thermal decomposition which creates pores of various sizes [31], [32].

The European project PEGASUS aims at developing new high-performance PGM-free catalysts for the ORR in acidic media. Several synthesis strategies have been investigated by the different partners of the project. Three of the catalysts developed within the project will be investigated in this work. In Armines, Youling Wang and Sandrine Berthon-Fabry developed a one-pot synthesis of a Fe-N catalyst based on a carbon aerogel, a structure with a high surface area and pore volume and a tunable pore size distribution [33]. The group of Sergio Rojas in Spanish research institution CSIC synthesized a Fe/N/C catalyst using a triazine based porous organic polymer as precursor in order to improve the reaction yield and the durability of the material synthesized [34]. In CEA, Fatima El Orf and Bruno Jousselme mixed iron and nitrogen precursors with carbon nanotubes in order to use the high surface area and the good conductivity of this support to enhance the activity of the catalyst [35]. The commercial catalyst developed by Pajarito Powder with the sacrificial support method will be also investigated in this work [28]. Moreover, a member of the advisory board of the project, Pr. Zelenay, kindly provided two catalysts developed in his laboratory, so that they can be evaluated with our method. The first is a CM-PANI-Fe-C(Zn) catalyst based on the dual nitrogen precursors synthesis [32], the second one is an atomically dispersed MOF-derived catalyst [36]. The morphology of all these catalysts is presented in Figure 4. This figure highlights the fact that the different synthesis give materials with very different morphologies. It seems thus very interesting to evaluate to what extend the morphology of a material impacts its electrochemical activity. Notably, the fabrication process of the CL will be of primary importance for ensuring that the catalytic sites remain accessible once the material is embedded in a layer.

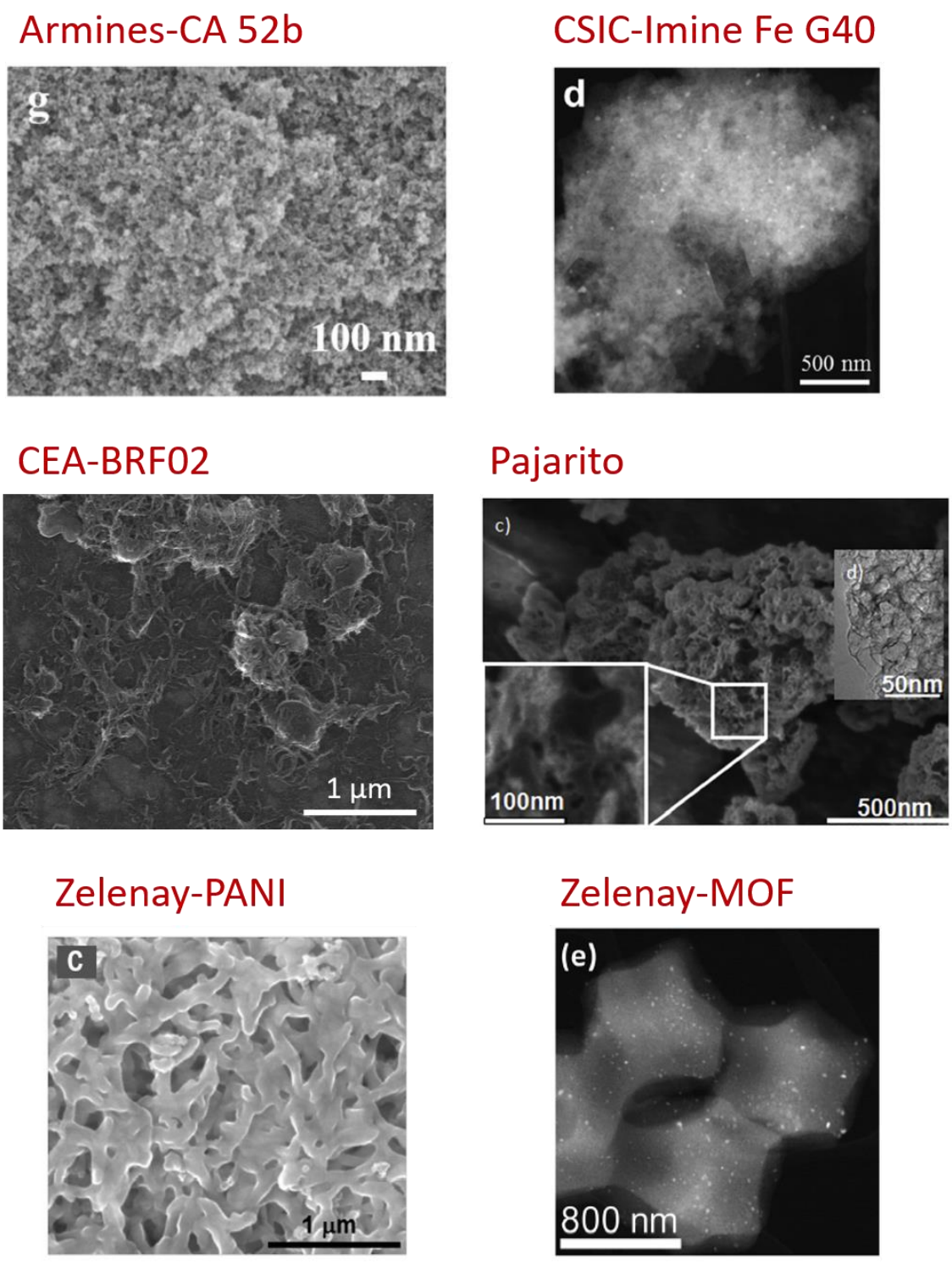

Figure 4: SEM, STEM and TEM images of the different PGM-free materials that will be studied in this work. Images taken from the publications cited in the text.

Beyond the electrocatalytic activity and accessibility of the active sites, the materials developed for ORR catalysis in PEMFC need to have a very good selectivity towards the production of water. Indeed, two pathways are coexisting for the ORR, the direct 4 e^- transfer that forms H_2O (4) and the indirect 2 e^- transfer that forms H_2O_2 (5):

$$O_2 + 4\,H^+ + 4\,e^- \rightarrow 2\,H_2O \qquad (4)$$

$$O_2 + 2\,H^+ + 2\,e^- \rightarrow H_2O_2 \qquad (5)$$

The indirect pathway is unwanted since the production of H_2O_2 lowers the overall efficiency in a fuel cell and degrades the membrane [37]. Quantifying the amount of H_2O_2 produced by the catalyst is thus very important. Practically, this quantification is not easy because some of the H_2O_2 produced within a layer of catalyst can react before being released in the solution and will not be detected.

I.2.3. Towards the optimization of PGM-free catalyst layer structure

With the recent progresses done over the last decade on the catalytic activity of PGM-free materials, more and more of them are now integrated in membrane electrode assemblies (MEA) and tested in full cell conditions. However, PGM-free catalysts still have a lower mass activity than the common Pt/C catalysts, principally because of their lower active site density and turnover frequency [38]. For comparable performance, a higher loading of catalytic material is used, leading to thicker layers than the one obtained with Pt/C catalysts. The thickness of the layer can lead to important transport losses. Indeed, an optimal architecture of the CL is very complex to obtain, each reactant needing to be brought to the catalytic site through different phases. The gases (O_2 at the cathode) arrive through the porosity of the material before dissolving in the ionomer, which transports the protons. The electrons are brought by the carbon structure. The water produced by the reaction at the cathode needs also to be evacuated efficiently through the pores. It is released under the form of vapor, but it can also condense into liquid water and fill the pores, making the active sites inaccessible to the reactants.

The structure of the CL depends on its fabrication process. A CL is fabricated by dispersing the different components (carbon supported catalyst and ionomer) in a solvent. The ink formed is then deposited on either the GDL or the membrane, creating a porous layer with the carbon phase and the ionomer phase embedded in each other. This process is illustrated on Figure 5:

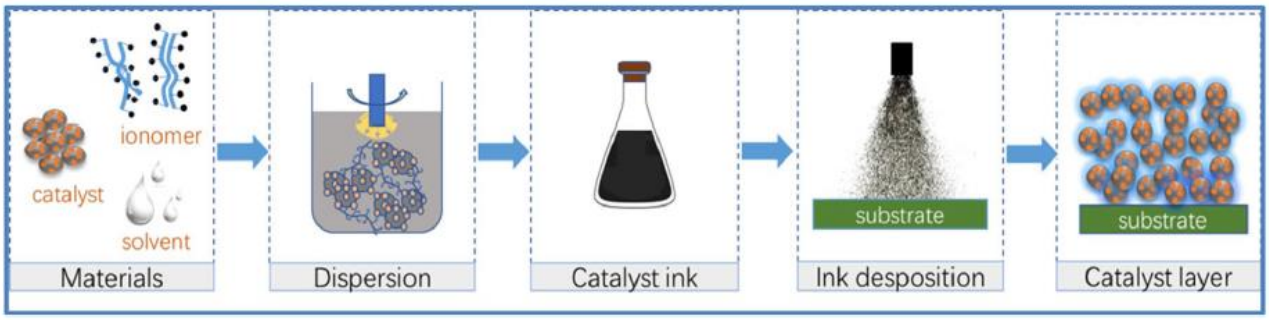

Figure 5: Illustration of the fabrication process of catalyst layer. Figure taken from [39].

The first step of the CL fabrication is the formulation of the ink. The catalytic material is mixed with the ionomer in a solvent and then dispersed in order to merge the two phases. The ionomer is a polymer composed of a polytetrafluoroethylene backbone and perfluorinated vinyl ether side chains whose length can vary. Depending on the length of these side chains, the ionomer can penetrate more or less the micropores. The diversity of the synthesis methods for PGM-free catalysts leads to various microporosities of the materials (see Figure 4). Moreover, the interactions between the active sites and the ionomer can vary depending on the catalyst [40]. It would thus be interesting to investigate the most adapted ionomer to each material. For now, Nafion is extensively used in the fabrication of PGM-free MEA. The ionomer content in the ink needs also to be optimized: a high amount of ionomer will increase the ionic conductivity but risks to block the gas pores and thus, the O_2 transport. This optimization has been done by Wang et al. [41] on the catalyst from Pajarito Powder: they found that a ionomer content of 35 %wt to 45 %wt leads to the better performance.

The dispersion step aims at producing particles of carbon bound with ionomer with the smallest size in order to optimize the accessibility of the active sites. The affinity of the catalyst and the solvent will strongly influence the quality of the dispersion, and thus the cell performance [42]. In general, PGM-free materials are highly hydrophobic and the solvents used are mixtures of water and alcohol (isopropanol, n-propanol, ethanol…). The dispersion techniques are also diverse: they can combine ultrasonication, ball milling and stirring.

Once the ink is sufficiently dispersed to be processed, it is deposited on a substrate (the membrane or the GDL) in order to form the catalyst layer. Several methods of deposition are coexisting: painting, drop casting, bar coating, spray coating, electrospinning, etc. When the catalyst is deposited on the membrane, the structure obtained is called a catalyst coated membrane (CCM). When it is deposited on the GDL, a gas diffusion

electrode (GDE) is formed. Afterwards, the MEA can be hot pressed in order to increase the connectivity between the different layers.

There is no consensus in the community about the best fabrication process, each group has a different expertise on the available techniques and work with different catalyst materials. For example, several fabrication methods have been used in the context of the PEGASUS project. The partners from CEA-Grenoble investigated different methods on the catalyst from Pajarito Powder [43]. In this study, CCM prepared with the decal transfer technique showed the best performance. Another partner of the project, Heraeus Precious Metals – Hydrogen Systems, used ball milling dispersion bar coating to fabricate CCM based on several catalysts from the project. Table 2 sums up the fabrication processes used in the literature over the past two years for PGM-free MEA:

Reference	**Catalyst**	**Ionomer**	**Solvent**	**Dispersion method**	**Deposition method**
Heraeus (PEGASUS)	Diverse	Nafion 40 %wt	1-propanol and water	Ball milling	Bar coating (CCM)
Toudret et al., 2021 [43] (PEGASUS)	PMF-011904 from Pajarito Powder	Nafion 47 %wt	Ethanol	Sonication 12 h + stirring (1 h)	Spray coating, bar coating (CCM and GDE)
Guo et al., 2021 [44]	Mn-N-C-S (ZIF-8 precursor)	Nafion (content not provided)	1-propanol and water (proportions not provided)	3 h stirring	Painting
Osmieri et al., 2021 [45]	PMF-011904 from Pajarito Powder	Nafion 35 %wt	isopropanol and water (1:1)	3 h sonication	Painting (CCM)
Park et al., 2020 [46]	(CM+PANI)-Fe-C(Zn))	Nafion 35 %wt	isopropanol and water (1:1)	2 h sonication	Spray coating (GDE)
Yang et al., 2020 [47]	Fe-N-C (ZIF-8 precursor)	Nafion 40 %wt	ethanol and water (1:1)	Sonication + stirring (1 h)	Drop casting (GDE)

Osmieri et al., 2020 [42]	PMF-011904 from Pajarito Powder	Nafion 35 %wt	n-propanol and water (0 %, 50 % and 82 % H_2O)	3 h sonication	Painting (CCM)
Wang et al., 2020 [41]	PMF-011904 from Pajarito Powder	Nafion 15-45 %wt	n-propanol and water (2:1)	1 h sonication	Spray coating (CCM)
Osmieri et al., 2019 [48]	(AD)Fe-N-C (ZIF precursor)	Nafion 45 %wt	isopropanol and water (1:1)	4 h sonication	Painting (CCM)

Table 2: Fabrication process of several PGM-free MEAs from the literature of the past two years.

The architecture of the CL obtained by the processes described before is a porous structure containing voids and agglomerates. Agglomerates are clusters of carbon particles embedded in the ionomer (see Figure 6). They contain the active sites, so their structure is very important for the accessibility of the reaction spots. If the agglomerates are too big, the reactants will have difficulties to reach the active sites located inside their core. If the ionomer phase and the carbon phase are not incorporated homogeneously, the protons will not be able to reach all the active sites. In both cases, the performance of the cell will be lower because of the poor utilization of the catalytic sites. Therefore, being able to control the size and the composition of the agglomerates is of key importance in the development of efficient PGM-free fuel cells. The various morphologies of the PGM-free materials and the various fabrication processes make the control of the agglomerates size and composition difficult. Thus, it is crucial to be able to characterize efficiently the material at different steps of the fabrication process and at different length scales. The main characterization techniques used nowadays by the scientific community will be presented in the following section.

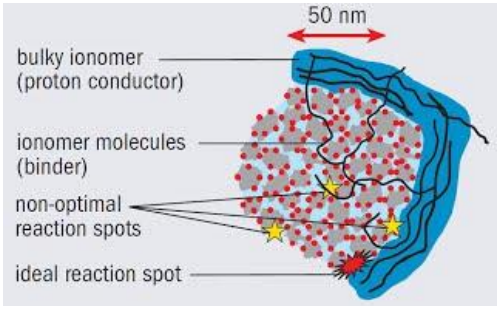

Figure 6: Illustration of the structure of an agglomerate.

I.3. Overview of the state-of-the-art PEMFC characterization methods

The performance of a fuel cell depends on both the intrinsic activity and the selectivity of the catalyst, and on its formulation within the catalytic layer. Being able to characterize these different aspects is the basis of improving PEMFC. This part aims at giving an overview of the main state-of-the-art techniques used to investigate the principal characteristics affecting the PEMFC performance.

I.3.1. Global cell performance

The most common way to evaluate the global performance of a PEMFC consists in acquiring a polarization curve on a single cell. While the fuel cell used in the automotive and stationary applications consists in a stack of several membrane electrode assemblies (MEA) connected through their bipolar plates, a single cell comprises a unique MEA pressed between two monopolar plates. The single cell can either have similar dimensions than the cells used in applicative stacks, or their dimensions can be reduced in order to limit current, compression or temperature inhomogeneities in the MEA plane [49]. In this case, they are called differential cells. The polarization curve consists in measuring the cell voltage in function of an imposed variation of the current. Different physical phenomena affecting the cell performance can be observed on the curve (see Figure 7).

The Nernst potential is the theoretical voltage of the cell depending on the Gibbs free energy of the reaction $\Delta G°$, the temperature T and the activities a_i of the reactants. It is calculated with the Nernst equation:

$$E = \frac{\Delta G°}{nF} + \frac{RT}{nF} \cdot log\left(\prod_{\nu_j} {a_i}^{\nu_i}\right) \quad (6)$$

with n the number of electrons exchanged during the reaction, F the Faraday constant, R the molar gas constant and ν_i the stoichiometry coefficients. The open circuit voltage V_{OCV} is the voltage measured when no current is applied to the cell, it differs from the Nernst potential because of the crossover of hydrogen through the membrane [51]. When the current applied to the cell is very low, the additional voltage losses are only due the kinetic limits of the electrochemical reactions, it is the activation losses. The ohmic losses are due to the transport of protons and electrons through the cell and increase linearly with the current following the Ohm's law. At high current, the supply of the reactants by the gas transfer through the electrodes is no longer sufficient

to maintain a constant concentration at the catalyst. The voltage decreases until it reaches zero when no more specie is available to the catalyst. A similar decrease of the current can be observed when the evacuation of the water produced at the cathode becomes ineffective. Liquid water accumulates in the pores and prevent the gases to access the active sites. This is called water flooding.

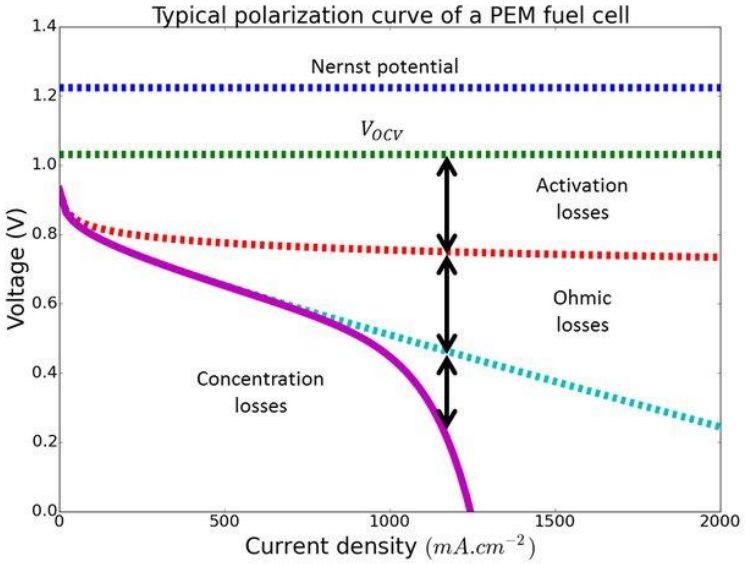

Figure 7: Visualization of the different physical phenomena visible on a polarization curve. Figure taken from [50].

Practically, the information contained in the polarization curve are difficult to deconvoluate without any supplementary information. This is why other characterization methods are used in order to investigate more precisely the phenomena governing the PEMFC.

I.3.2. Catalyst activity and selectivity

Rotating disk electrode (RDE) is a technique widely used for studying the ORR mechanism on a given catalyst. It consists in depositing a thin layer of catalytic material on a glassy-carbon electrode subjected to a rotation on its own axis. The rotation creates a laminar flow of solution towards and across the electrode, leading to a controlled supply of electroactive species to the active surface. The mass transport of the reactive species is thus controlled and depends on the rotation speed of the electrode. The Koutecky-Levich equation gives the expression of the electrode current:

$$\frac{1}{j} = \frac{1}{j_K} + \frac{1}{j_L} = \frac{1}{j_K} + \frac{1}{0.62nFAC_0^* D_0^{*2/3} \nu^{-1/6} \omega^{1/2}} \quad (7)$$

with j_L the diffusion limited current density, n the number of transferred electrons, A the electrode area, C_0^* the bulk concentration of the electroactive specie, D_0^* its diffusion coefficient, ν the kinematic viscosity of the solution and ω the rotation speed of the electrode. The kinetic current density j_K can be easily quantified by measuring the electrode current at several rotation rates.

The rotating ring disk electrode (RRDE) consists in adding a ring electrode around the RDE set-up. This ring serves for the detection of the intermediates generated by the reaction at the disk electrode. For ORR investigation, the H_2O_2 produced by the 2 e^- pathway (see Eq. (5)) is quantified with RRDE measurements. This enables to study the selectivity of the ORR, on condition that all the H_2O_2 produced by the material is effectively released in the solution. The percentage of H_2O_2 produced by the reaction $\% H_2O_2$ and the global number of electrons transferred per O_2 molecule at the catalyst n_C are expressed in function of the currents measured at the disk i_d and at the ring i_r:

$$\% H_2O_2 = 2 \times \frac{i_r/N}{i_d + i_r/N} \times 100 \quad (8)$$

$$n_C = 4 \times \frac{i_d}{i_d + i_r/N} \quad (9)$$

with N the collection efficiency of the ring. The RDE and RRDE set-up are illustrated on Figure 8:

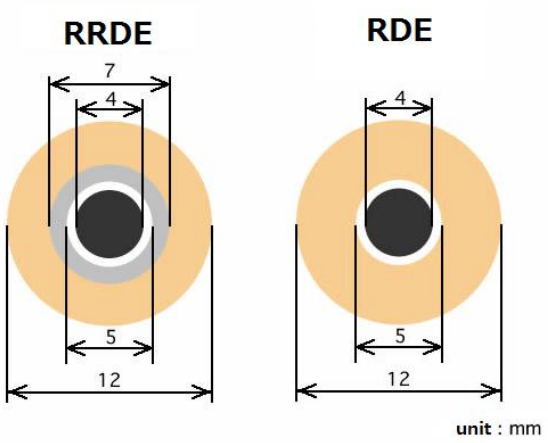

Figure 8: Illustration of the RDE and the RRDE.

The utilization of RDE and RRDE to extract the intrinsic activity and selectivity of a material requires that the flow at the electrode surface is perfectly laminar. Otherwise, the Koutecky-Levich approach is not valid. A laminar flow occurs when the deposit of catalyst is flat and homogeneous, which is not always the case

during experiments. This issue has been addressed by the scientific community in the field on Pt/C materials and the importance of employing standardized testing protocols has been highlighted [52]. With PGM-free materials, higher loadings are used in order to be able to reach the diffusion limited current. Typically, the loadings used for Pt/C materials characterizations are between 5 and 100 $\mu g_{Pt}.cm^{-2}$ [53] while loadings of 600 to 800 $\mu g.cm^{-2}$ are used to characterize PGM-free materials [54], [55]. These higher loadings lead to a higher roughness of the deposits and the risk to disrupt the laminar flow is enhanced. Moreover, the transportation of species within a thick layer is not considered by the Koutecky-Levich approach, which becomes inaccurate at too high loading. Although some groups are considering the pitfalls engendered by the thick layers [56], [57], most of the new developed PGM-free materials are nowadays characterized with only RDE [54], [55], [58].

Finally, if the layer of catalyst deposited on the electrode is thick, the H_2O_2 produced at the active sites can be further reduced in H_2O through a new 2 e^- reaction in the layer:

$$H_2O_2 + 2\ H^+ + 2\ e^- \rightarrow 2\ H_2O \qquad (10)$$

Hence, the amount of H_2O_2 released in the solution and measured at the ring will lead to an underestimation of the real quantity of H_2O_2 that was produced within the layer. This underestimation can have severe consequences since H_2O_2 is a specie that degrades the fuel cell. Its precise quantification is thus challenging but very important for the development of efficient and durable fuel cells.

I.3.3. Proton and electron conductivity

The ohmic phenomena occurring in a PEMFC are usually studied with electrochemical impedance spectroscopy (EIS). This technique consists in applying a low intensity sinusoidal variation to the cell potential and record the current response at several frequencies. By scanning the system over a wide range of frequencies (typically between 1 Hz and 200 kHz), phenomena with different time constants can be separated. The electrons transport is observed at high frequencies (100 kHz – 10 MHz), while the protons transport is visible between 1 kHz and 10 kHz. Electrochemical reactions and mass transfer are detected at the lowest frequencies. Equivalent circuit modeling of EIS data are used to extract quantitative information from the measurements. The main advantages of EIS technique is its ability to probe *operando* many different phenomena without being destructive.

I.3.4. CL structure analysis

Imaging techniques aim at investigating the internal structure of the CL. Radiations are diffused over the structure and their interactions with the materials enable to reconstruct the architecture and/or the composition of the layer. Several techniques are coexisting, based on different radiations (X-rays, electrons, neutrons) and their different interactions captured by the detectors (reflected, transmitted). The techniques are characterized by their different resolutions and fields of view (FOV).

The most used technique is scanning electron microscopy (SEM). It consists in scanning a surface with a focused beam of electrons which excite the atoms on the surface. The secondary electrons emitted after the desexcitation are detected and provide information about the topography of the sample. The images obtained are two-dimensional and provide information only about the external exposed surface of the material. SEM can acquire images with various resolutions and FOV, enabling images from millimeter scale to nanometer scale. SEM is widely used to image the materials before their integration in an MEA [59], [60]. Images are also performed on slices of used MEA in order to determine after the electrochemical characterizations the morphological characteristics of the CL (porosity, agglomerates size) [61]. Coupled with energy dispersive X-ray spectroscopy (EDX), this technique can also provide information about the chemical structure of the material. Transmission electron microscopy (TEM) provides similar information than SEM with a higher resolution [59]. It applies however on ultra-thin slices (~100 nm) which can be more difficult to obtain. Focused ion beam scanning electron microscopy (FIB-SEM) consists in acquiring several SEM images on the sample, which is cut layer by layer by an ion beam between each image. It is a destructive technique that can provide a reconstruction of the 3D structure of the material [62].

X-ray computed tomography (CT) consists in performing a radiography of the sample and provides 3D images of its structure. The resolution and the FOV of this technique can be adapted depending on the scale investigated. Komini Babu et al. resolved the morphology of PGM-free cathodes by performing nano CT images at two resolution levels (150 nm resolution / 65 µm FOV and 50 nm resolution / 16 µm FOV). In a first study, they extracted the distribution of agglomerate sizes and the local O_2 diffusion coefficient from these images and integrated them in a numerical model. This model highlighted the impact of liquid water formation within the CL, leading to significant transport losses [63]. The method was reused in a second work where more structural characteristics (porosity, agglomerate size distribution, pore size distribution) and effective transport properties (oxygen diffusivity, ionomer conductivity, tortuosity) were extracted from MEAs with three different Nafion contents [61]. These characterizations served to elucidate the microstructural origins of the performance changes due to the variations of ionomer loading. This study was the basement of a modeling work

highlighting the need for an increase of the cathode hydrophobicity and ionomer conductivity [64]. Serov et al. combined micro CT (3.3 mm FOV) and nano CT (80 µm FOV) to capture the full through-thickness morphology of a PGM-free cathode and extract structural and transport properties [59]. They observed an important inhomogeneity of the layer through its thickness thanks to the large FOV of the micro CT technique. X-ray CT can be used during the cell operation. Liu et al. used *operando* micro CT and modeling to study the formation of liquid water in three electrodes fabricated with different methods [65]. They concluded that the trough-thickness inhomogeneities play the most important role in the water withdrawal.

Imaging techniques are a very interesting tool for the investigation of the link between the structural properties and the electrocatalytic activity of a material. They are mainly used to characterize a CL after the electrochemical measurements in single cell. However, the resolution and the FOV of these techniques do not enable to image an entire electrode at nanometer scale. Thus, the information linking the electrocatalytic activity to the structure is only partial. Modeling is often used to deepen the investigation with these techniques, the different approaches will be presented in the Chapter IV.

I.4. Conclusion and objectives of the thesis work

The decarbonization of the transportation sector implies a wide development of electric vehicles. Fuel cell electric vehicles based on the PEMFC technology are of great interest because of their long travel range and their rapidity of refueling. However, PEMFC still face several challenges to reduce their cost and accelerate their expansion. The replacement of the Pt catalyst by PGM-free materials can reduce a lot the costs of a PEMFC stack. The integration of these materials in the thicker catalyst layer without creating supplementary transport losses is a challenge to which the scientific community devotes many efforts. The formulation processes are numerous and complex and the optimization of the CL structure makes the use of various characterization techniques necessary. These techniques are mostly applied to thick catalyst layers, in which a lot of different phenomena can affect the cell performance. With these techniques, it is difficult to deconvoluate the contribution of specific features of the CL such as the agglomerates. The agglomerate is indeed a key feature in the CL, its size and composition will affect the accessibility of the active sites and thus, the overall performance of the cell.

In this thesis work, we propose an approach based on the use of local probe techniques in order to study the catalyst material at agglomerate scale. Being able to perform direct experimental characterizations

on the agglomerates will provide new insights on the behavior of these features. Scanning electrochemical microscopy (SECM) and atomic force microscopy (AFM) will be used to link the electrocatalytic activity of a material to its agglomeration state, these techniques will be presented in the next chapter. The establishment of a characterization protocol will be detailed and applied to PGM-free catalysts from the PEGASUS project.

Chapter II

Development of a characterization method based on SECM and AFM for the study of catalysts at agglomerate scale

The aim of this chapter is to present the development of a method based on scanning electrochemical microscopy (SECM) and atomic force microscopy (AFM) for the characterization of PGM-free ORR catalysts at agglomerate scale. SECM and AFM are two local probe techniques which enable to study a very few amount of material deposited on a substrate (4-90 µg.cm^{-2} as we will see in the chapter). They will serve here to link the electrochemical activity of a catalyst to its agglomeration state. After presenting the two techniques and their present utilization in the field of electrocatalysis and energy storage, the implementation of the characterization method will be detailed. This method will be first applied for the study of several PGM-free materials developed within the PEGASUS project. Then, different ink formulations will be compared on one of the materials studied before.

II.1. Local probe techniques for electrocatalysis and energy storage

Local probe techniques are a family of instruments that consist in studying the interactions between a probe and a substrate. They enable to probe interfaces, thin-films or very few amounts of material deposited on the substrate. They provide information at a scale corresponding to the size of the probe (atomic to micrometric scale). The variety of the techniques (STM, AFM, SECM…) developed over the last decades enables to probe numerous physico-chemical phenomena such as the topography, the conductivity, the chemical or mechanical properties of a surface [66], [67].

II.1.1. Scanning electrochemical microscopy

Scanning electrochemical microscopy (SECM) consists in recording the current response of an ultramicroelectrode (UME) moved in the vicinity of a substrate. When the UME (called the probe) is positioned far from the substrate surface, its steady-state current depends on the geometry of the electrode and on the concentration of the redox mediator in solution. For a microdisk electrode [68]:

$$i_{T\infty} = 4n_{probe}FDC^{*}r_{T}\beta(RG) \quad (11)$$

with n_{probe} the number of electrons exchanged at the probe, F the Faraday constant, D and C^{*} the diffusion coefficient and the bulk concentration of the redox mediator, r_T the radius of the microdisk and $\beta(RG)$ a correction factor considering the finite dimensions of the electrode. Indeed, the active microdisk of the probe is embedded in a glass capillary whose dimensions have an influence on the current measured. $RG = \frac{r_{glass}}{r_T}$ is the dimensionless parameter representing the ratio between the glass part and the active part (see Figure 9).

$$\beta(RG) = 1 + \frac{0{,}1380}{(RG - 0{,}6723)^{0{,}8686}} \quad (12)$$

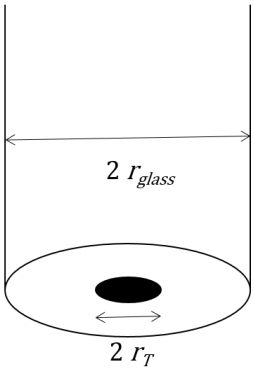

Figure 9: Schematic representation of an ultramicroelectrode.

When the UME is approached to a substrate, its current reflects the local topography and electrochemical activity on this substrate. Several modes of SECM are possible, enabling the characterization of different phenomena. They are described on Figure 10:

A. In bulk solution, the probe current depends on the concentration in redox mediator (noted R here).

B. In negative feedback mode, the probe is approached to an inert substrate whose presence hinders the diffusion of the specie R. The decrease of the probe current is directly linked to its dimensions. Cornut and Lefrou [69] established an analytical expression linking the probe current to the dimensions r_T and RG:

$$NIT(L, RG) = \frac{\frac{2{,}08}{RG^{0{,}358}}\left(L - \frac{0{,}145}{RG}\right) + 1{,}585}{\frac{2{,}08}{RG^{0{,}358}}(L + 0{,}0023RG) + 1{,}57 + \frac{\ln(RG)}{L} + \frac{2}{\pi RG}\ln\left(1 + \frac{\pi RG}{2L}\right)} \quad (13)$$

with $NIT = \frac{i_T}{i_{T\infty}}$ the dimensionless probe current and $L = \frac{d}{r_T}$ the dimensionless tip to substrate distance (d being the distance between the probe and the substrate). Hence, approach curves in negative feedback mode are used to determine with precision the dimensions of the SECM probe.

C. In positive feedback mode, the probe is approached to a conductive substrate. In this case, the O specie generated at the probe is reduced back to R by the substrate, leading to a local increase of the concentration in R, and thus to an increase of the probe current. This mode is principally used to determine kinetic rates of heterogeneous electron transfer at the substrate material [70], [71]. It can also be used to map the electronic conductivity of a 2D material, such as MoS_2 monolayered flakes [5].

D. In substrate generation/tip collection (SG-TC) mode, a redox specie (O here) is generated at the substrate and detected at the probe. This mode can provide a mapping of the chemical fluxes occurring at the substrate. It is principally used in the corrosion field, where it serves to characterize the localized corrosion processes on a metal surface [72], [73].

E. In tip generation/substrate collection (TG-SC) mode, the redox specie O is generated at the probe and detected at the substrate. The collection efficiency is thus higher than in SG-TC mode. This mode is principally used for the measurement of reaction kinetics [74] or to perform localized modifications on a substrate [75].

F. In redox competition (RC) mode, the probe and the substrate are polarized so that they both consume the specie R. The probe will measure the local depletion in R caused by the consumption at the substrate. In this way, the activity of the substrate can be probed by the RC-mode. The RC-mode was introduced by Schuhmann's group in 2006 for the investigation of ORR [76]. It is more and more used in the field of electrocatalysis for the study of various reactions [77], [78].

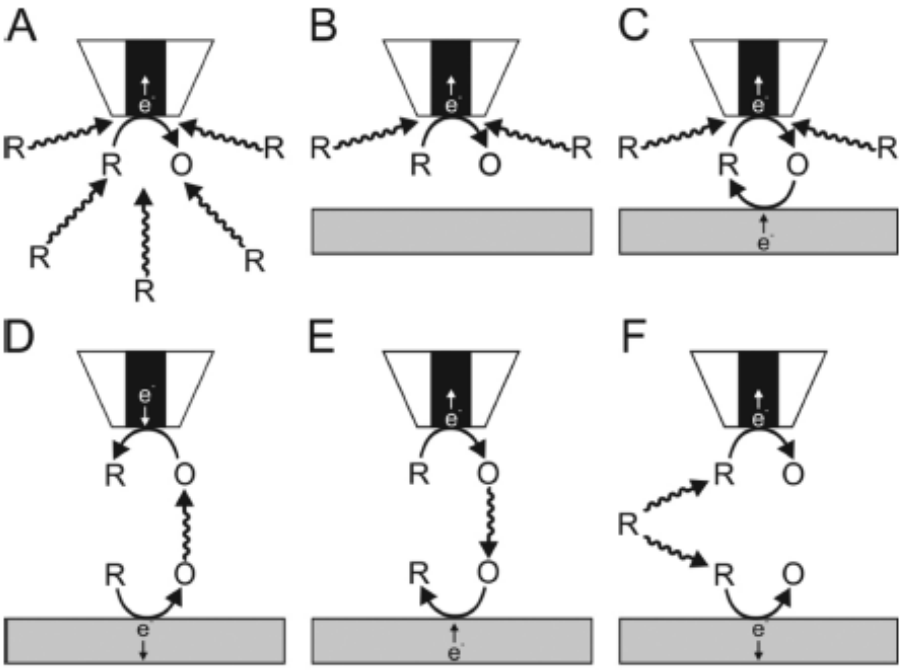

Figure 10: Illustration of the different modes of SECM. (A) UME in bulk solution. (B) Negative feedback. (C) Positive feedback. (D) Substrate generation/tip collection. (E) Tip generation/substrate collection. (F) Redox competition. Figure taken from [79].

SECM is a very versatile tool that is used in various research fields. The ability of the technique to map heterogeneous electron transfer over a surface makes it very interesting for corrosion studies [72], [73]. Its high spatial resolution leads to applications in localized surface modification like etching [80] or deposition [75]. In biology, SECM is used to investigate proteins [81], DNA [82], enzymes [83] or even living cells [84], [85]. In material science for energy, SECM is used to investigate materials or interfacial processes in the field of batteries [86], [87], [67], solar cells [88], supercapacitors [89], [90] or fuel cells [91], [92]. In the specific field of fuel cells and electrolysers, SECM is extensively used to probe the electrocatalytic activity of materials for the ORR, the HOR, the HER or the OER. A review of the recent works that investigated these reactions with SECM has been published by our group in 2020 [93].

The development of the SECM instrumentation is still very active. Many variants of the classical SECM set-up are being developed in order to investigate specific issues. Scanning ion conductance microscopy (SICM) consists in measuring the changes of ion conductance between an electrode placed in a nanopipette and an electrode in solution [94]. When the nanopipette is approached to the substrate, its current is strongly affected by the changes of substrate to nanopipette distance. Thus, this technique enables to measure the topography of the substrate with a resolution of approximately 200 nm. SICM is mainly used for investigating living cells [95], [96], or performing conductance measurements on porous materials [97]. Scanning electrochemical cell microscopy (SECCM) consists in approaching a nanopipette filled with electrolyte and containing an electrode to a substrate placed in ambient air. A droplet is formed at the end of the pipette and enters in contact to the substrate, enabling the measure a conductance current [98]. The main advantage of this technique is the fact that only a small part of the sample is in contact with the solution. This enables to investigate substrates sensitive to corrosion, passivation or surface fouling [99], [100]. Shear-force SECM consists in using a flexible probe oscillating laterally in order to position it via the dampening of the oscillation when the probe is approached to the substrate [101]. Similarly, the intermittent contact mode of SECM (IC-SECM) is based on the dampening of oscillations in the vertical direction [102]. In the last five years, shear-force SECM was used to probe the local reaction environment during CO_2RR [103], the morphology of MEA [91] or dye-sensitized solar cells [104]. IC-SECM was used to investigate defects in single crystal boron doped diamond electrodes [105] and map conductivity in solid Li-ion conducting electrolyte [106].

II.1.2. Atomic force microscopy

Atomic force microscopy (AFM) measures the interaction force between a tip fixed on a cantilever and a surface. The deflection of the tip caused by the variations of the surface's topography is detected by a quadrant photodetector monitoring a laser beam reflected on the cantilever (see Figure 11). Several operation modes are existing [107]. The contact mode consists in dragging the tip across the surface, this mode is destructive for both the tip and the substrate. Hence, tapping modes are more frequently used. In these modes, the cantilever oscillates near to its resonance frequency and the information about the topography is given by variations of amplitude of the oscillation. AFM is principally used for measuring the topography of surfaces [108], [109] and nanoparticles [110], [111], monitoring the growth of thin-films [112], investigating interfaces [113], [114] or defects [115].

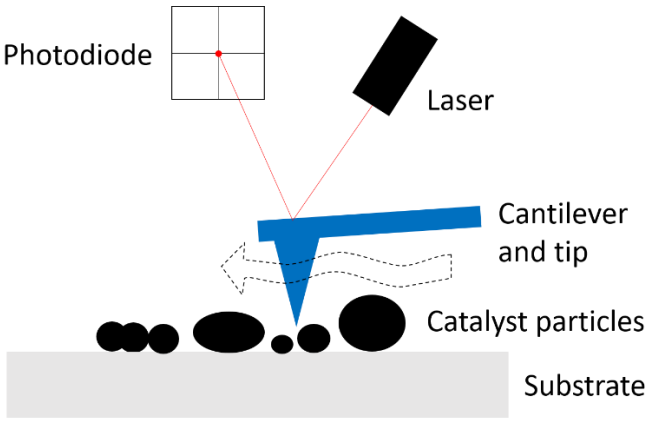

Figure 11: Principle of atomic force microscopy (AFM).

Beyond topography measurements, the tip can also be used to probe other phenomena. Conductive AFM (C-AFM) consists in applying a bias to the tip and recording the current flowing between the tip and the substrate during contact mode measurements. This technique was applied for example for measuring the conductivity of a MOF-graphene nanocomposite [116]. The conductivity measured with C-AFM was four order of magnitude higher than the one measured with the 4-point method. The dramatic enhancement of the conductivity was ascribed to the delocalization of interfacial states between MOF and graphene. AFM can also be used to investigate the mechanical properties of a material, notably under the form of discrete particles. Sun et al. [117] studied the elastic modulus of single MOF nanoparticles and showed that the mechanical properties of these materials can be tuned by adjusting the chemical functionalities of the ligands. In the field of PEMFC, the distribution and size of the ionomer phase at the surface of the CL was retrieved from AFM adhesion images [118]. Kelvin probe force microscopy (KPFM) consists in measuring the contact potential

difference of materials and is used to characterize the surface potential and work functions of electrical devices, semi-conductors or metallic materials [119]. In the field of solid state Li-ion batteries, KPFM has been used to map the internal potential of a composite cathode before and after charging [120]. Electrochemical strain microscopy (ESM) enables to detect local strains in mixed ionic-electronic conductors due to electrochemically induced compositional changes. It has been used to link the changes of ionic mobility with the number of charge/discharge cycles in Li-ion batteries [121].

AFM is often performed in ambient air environment. However, it is possible to use this technique in a liquid media, enabling to combine it with electrochemical measurements. Electrochemical AFM (EC-AFM) can be used for simultaneous topography measurement and electrochemical analysis of the substrate, which is used as working electrode in a three electrodes set-up. EC-AFM is used for the visualization of structure changes during an electrochemical process. For example, it has been used for observing the formation of the SEI during charging and discharging cycles in Li-ion batteries [122]. It is also possible to use the AFM tip as a fourth electrode and perform AFM-SECM. This technique enables to measure simultaneously the topography and the electrochemical activity of single nanoparticles [123], [124] or electrodes interfaces [125]. AFM-SECM is also used in the field of biology [126], [127], [128]. However, this technique remains limited to a few number of studies because of the high cost of the probes and their low durability and reliability, which limits the sensitivity of the electrochemical signal [129].

II.1.3. Approach of this work

The aim of this work is to develop a methodology using SECM and AFM to investigate an ensemble of catalyst particles at agglomerate scale. To the best of our knowledge, AFM and SECM are currently used (separately or as an AFM-SECM set-up) for the characterization of interfaces [130], [125], [131], thin films [132], [133] or individual nanoparticles [134], [124]. Performing a statistical analysis on a large ensemble of diverse particles will enable to link the electrocatalytic activity of the material to its agglomeration state. Practically, the catalyst particles are deposited on a substrate using a spray-coater. SECM is then performed in redox competition (RC) mode in order to measure the global ORR activity of the particles ensemble. Finally, the deposit is imaged with AFM in order to measure the size of the particles and a computational image treatment is used to determine the exact volume of material deposited, as well as its agglomeration state. This method is illustrated in Figure 12. It enables to study deposits with a very low loading (4-90 $\mu g.cm^{-2}$) compared to the loadings used with RDE (600-800 $\mu g.cm^{-2}$ for PGM-free materials [54], [55]).

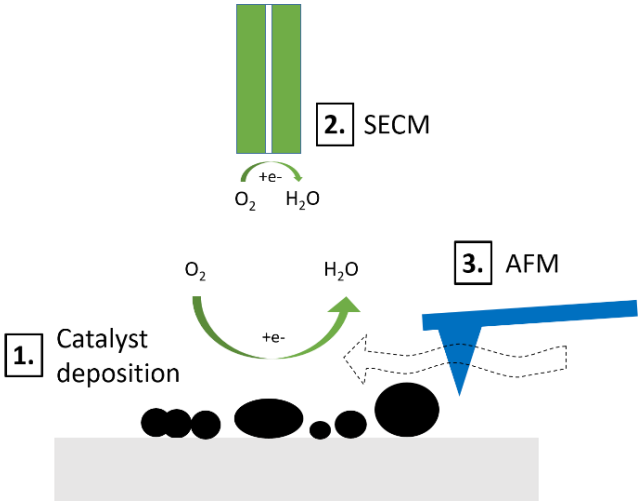

Figure 12: Illustration of the method consisting in combining SECM and AFM characterizations for the study of a catalyst electrochemical activity linked with its agglomeration state.

The development of the protocol is based on the work of Olivier Henrotte, who pursued his PhD in the LICSEN from 2015 to 2018 [135]. Olivier developed a protocol of RC-SECM characterizations aiming at performing steady-state, reproducible and comfortable measurements. He investigated the probe material and showed that using a gold probe instead of the widely used platinum probe increases the reliability and the reproducibility of the RC-SECM technique in acidic conditions. He also investigated different types of substrate: the commonly used glassy carbon substrate, or silicon wafers covered with gold or boron doped diamond (BDD). The activity towards ORR, the planarity and the roughness of these substrates have been investigated. The BDD substrate showed the lowest ORR activity, a high stability and a very good reusability. These two aspects were the subject of an article published in 2020 [6].

My contribution consists in developing further the characterization protocol developed by Olivier Henrotte, notably by including AFM measurements. After presenting the improvements brought to the characterization protocol, several PGM-free catalysts developed within the European project PEGASUS will be investigated with this method. The aim is to benchmark their intrinsic activity in order to compare their performances. The materials behavior towards the ink formulation and deposition will be investigated by comparing the agglomeration state of the deposits. Finally, the effect of the ink formulation on the agglomeration state will be investigated on one of the PEGASUS materials.

II.2. Method development

II.2.1. Catalyst deposition

Both SECM and AFM characterizations require that the catalyst material is deposited on a substrate. SECM requires a micrometric planarity, a sufficient conductivity and a low electrochemical activity while AFM requires a roughness smaller than the size of the particles to image. The silicon wafers covered by BDD or gold studied by Olivier Henrotte [6] have an excellent planarity. Although the BDD substrate was found to have the lowest activity towards ORR (inactive until -0.3 V/SCE), it had a roughness average of 39.9 nm which is the order of magnitude of the smallest catalyst particles we want to image with AFM. Thus, the Si-wafer covered with gold substrate was chosen for its lower roughness average (< 1 nm), despite a smaller inactive window (until 0 V/SCE).

A spray-coater (ExactaCoat apparatus from Sonotek) is used for the deposition of the catalyst on the substrate. It is combined with a mask with micropatterns (from Micron Laser Technology) in order to control the size and the shape of the deposits (squares of side 200 µm). On top of that, a home-made device that enables to spray onto one micropattern at a time has been developed. It makes easy the creation of different samples, for a benchmarking purpose for example. It is composed of two sliding plates with a slit that are moved over the micropattern on which we want to deposit (see Figure 13 (a)). The spray-coater parameters are adjusted in order to create deposits as homogeneous as possible. The flow rate has to be high enough for the catalyst to reach the substrate through the two sliding plates and the mask, but not too high to avoid flooding the substrate. A value of 0.3 $mL.s^{-1}$ has been fixed. The atomization of the solution is controlled by the Shaping Air parameter which is fixed to 0.3 kPa. The distance between the nozzle and the deposition device is reduced at its minimum (5 mm) in order to get the littlest spray area, while keeping the flow consistent. A path of spraying is created in the Sonotek software. It consists in covering the area with four successive serpentine passages, each passage starting in a different direction and overlapping the others (see Figure 13 (b)). This way of spraying creates homogeneous deposits, with no edge effect, as illustrated on Figure 13 (d). Each path (the four steps) sprays 0.15 mL of ink on the substrate, and deposits of different loadings can be created by repeating the path as many times as necessary.

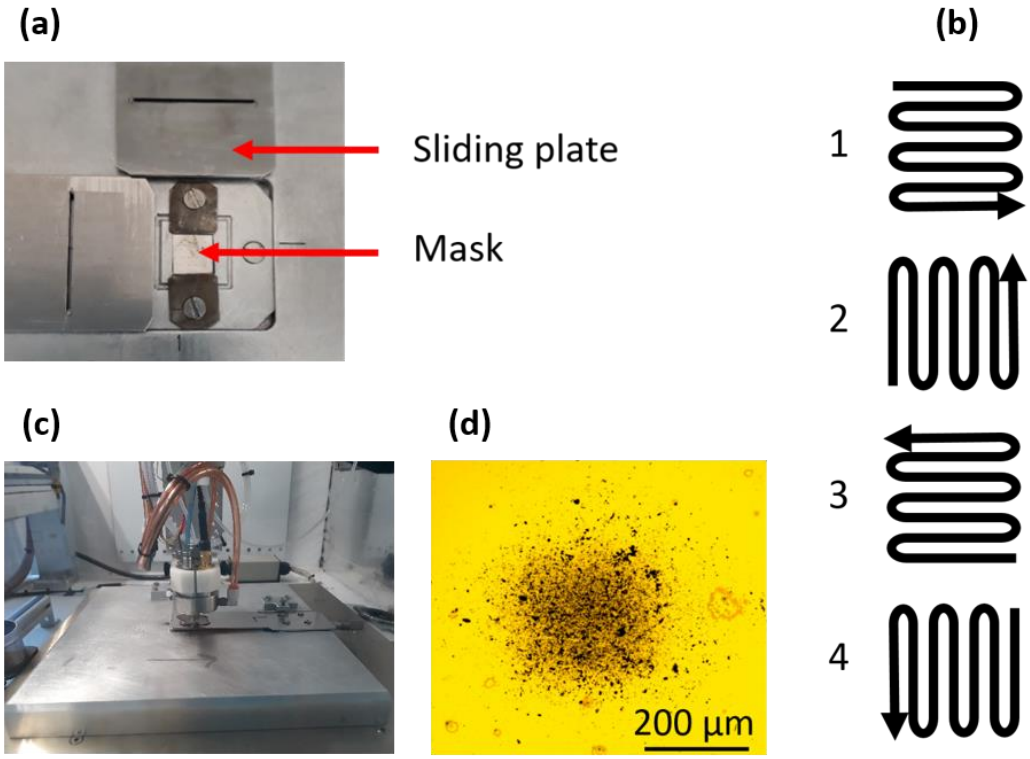

Figure 13: (a) Mask and sliding plates enabling to spray one deposit at a time. (b) Illustration of the path of spraying which consists in the four represented passages sprayed on the same area successively. (c) Sonotek nozzle spraying on the deposition device. (d) Optical image of a deposit obtained with the method developed.

A very diluted ink (0.2 $g.L^{-1}$) is used in order to facilitate the flow in the Sonotek hose and to be able to spray very low loadings. Thus, the solvent evaporation needs to be managed carefully, otherwise the ink will spread under the mask and flood the other deposits. The deposition device is placed on the heating plate of the Sonotek, which is heated at 80°C. A heating lamp is also placed above the set-up. This enables to keep the substrate at 80°C and the sliding plates at 60°C during the deposition. Moreover, pauses of few seconds are programmed between the spraying cycles in order to let the solvent fully evaporate. The ink is prepared by dispersing 6 mg of catalyst powder in a mix of ethanol and water (3:1) under sonication. Only 5 % wt of Nafion (D-520) is added for the purpose of studying the intrinsic activity of the catalyst. The catalyst powder and the Nafion are first dispersed in 1 mL of solvent and sonicated for 5 minutes in a Vibra-Cell VCX 130 PB from Sonics Material. Afterwards, the total volume of solvent is increased to 2 mL and the sonication process is repeated. The same process is continued by increasing the total volume to 5 mL, 10 mL and 30 mL to obtain a catalyst ink of 0.2 $g.L^{-1}$. After the deposition, the deposits are rinsed with pure ethanol and dried under a flux of compressed air in order to remove the particles with a poor adhesion on the substrate. Then, they are imaged with an Olympus BX61 optical microscope in order to check their homogeneity and to measure their precise dimensions.

II.2.2. SECM characterizations

SECM is used in redox competition (RC) mode in order to evaluate the activity of the catalysts towards ORR in an acidic solution. It is performed prior to AFM to prevent any fading of the electrochemical activity with time. The substrate is placed in a 0.1 M H_2SO_4 solution saturated with oxygen by bubbling gaseous O_2 in the solution. It is connected to the electrical circuit with a gold piece touching the golden surface of the wafer. A platinum wire is used as counter electrode and a saturated calomel electrode (SCE) serves as reference electrode. Both counter electrode and reference electrode are placed in sintered guards to avoid direct contact with the solution. The gold ultramicroelectrodes are either home-made or come from Sensolytics. The M470 Workstation from Bio-Logic Science Instruments is used for the SECM measurements. A camera overlooks the set-up in order to locate easily the deposits. A photography of the set-up is shown on Figure 14.

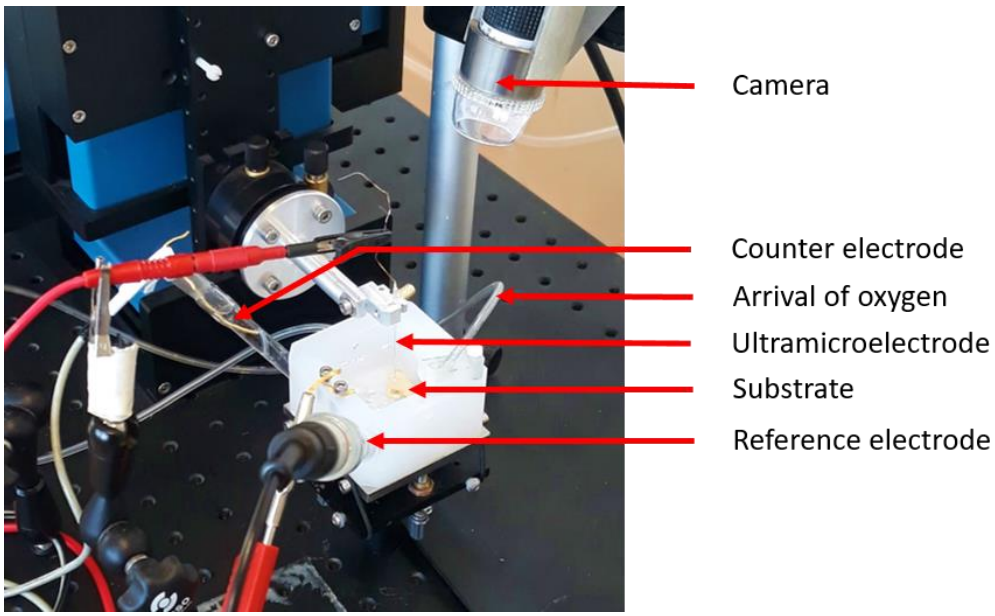

Figure 14: Photography of the SECM set-up.

The aim of the protocol is to perform quantitative measurements. Notably, a diffusion limited current is required at the probe in order to apply the analytical expression of the current at a microdisk electrode:

$$i_{T\infty} = 4n_{probe}FDC^{*}r_T\beta(RG) \qquad (14)$$

Thus, the potential applied at the probe has been carefully chosen. With the gold probe, there is no well-defined diffusion plateau for the ORR measurement, as showed on the cyclic voltammetry (CV) on Figure 15

(a). The ORR happens approximately between -0.2 V/SCE and -0.7 V/SCE and the proton reduction starts around -0.7 V/SCE, in the continuity of the ORR wave.

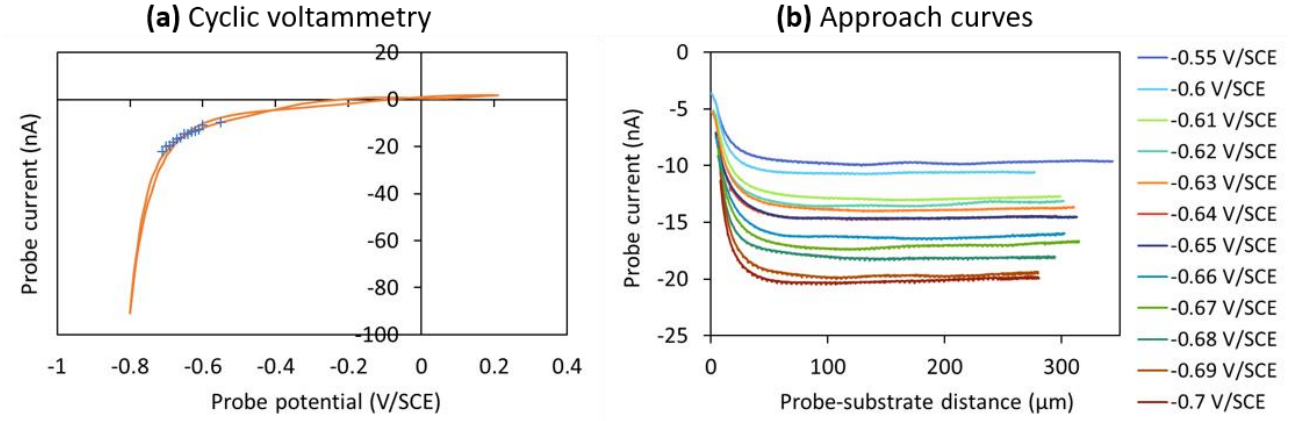

Figure 15: (a) CV from 0.2 V/SCE to -0.8 V/SCE with a scan rate of 10 mV/s, crosses represent the stabilized currents of the approach curves. (b) Approach curves at different probe potentials with a probe-substrate distance from 0 µm to 300 µm and a moving speed of 2 µm/s. (5 µm gold probe in a 0.1 M H_2SO_4 solution saturated in O_2)

In order to be able to use properly the previously presented analytical expression (see Eq. (14)), we try to approach to a maximum the diffusion plateau without reaching the proton reduction potential range. The aim is to find the best compromise between the sensitivity and the selectivity of the measurement. Negative feedback approach curves have been recorded with the probe polarized at different potentials between -0.55 V/SCE and -0.7 V/SCE. The electrode is first brought carefully into contact with the substrate, then it is retracted at 2 µm/s until the current reaches a stable value. This stable value occurs at approximately 100 µm from the substrate (L≈20) and is used to normalize the data. These data (noted NIT_{exp}) are compared to the analytical expression of $NIT(L, RG)$ established by Cornut et al. [69]. The values of r_T and RG are fitted, using the least squares method and the Solver module of Excel to minimize the sum of the squared residuals.

$$NIT(L,RG) = \frac{\frac{2{,}08}{RG^{0{,}358}}\left(L - \frac{0{,}145}{RG}\right) + 1{,}585}{\frac{2{,}08}{RG^{0{,}358}}(L + 0{,}0023RG) + 1{,}57 + \frac{\ln(RG)}{L} + \frac{2}{\pi RG}\ln\left(1 + \frac{\pi RG}{2L}\right)} \qquad (15)$$

The number of electrons exchanged at the probe is then calculated using the expression of the diffusion-limited current at a microdisk electrode (Eq. (14)). Figure 16 shows the calculated values of n_{probe}, r_T and RG for the different potentials applied to the probe.

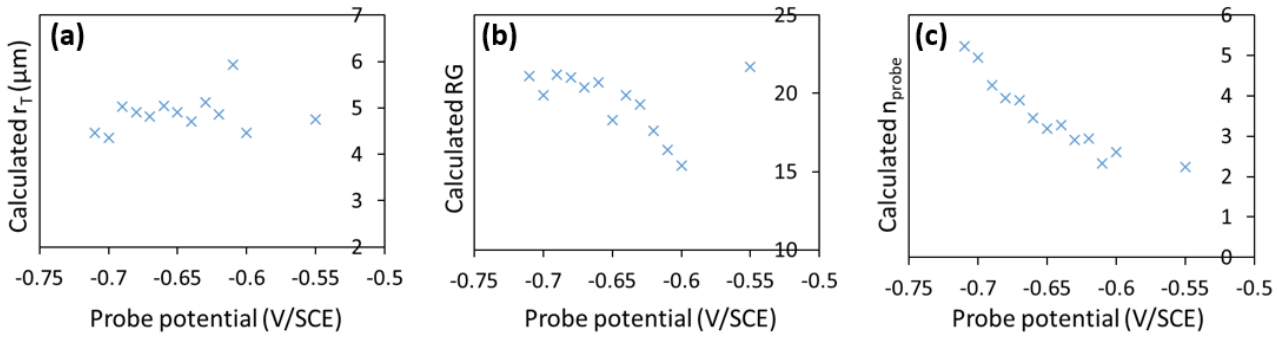

Figure 16: Calculated values of r_T, RG and n_{probe} from approach curves recorded at different probe potentials

The value of r_T remains constant regardless the probe potential. The value of RG is increasing from -0.55 V/SCE to -0.65 V/SCE and remains constant at the potentials below -0.65 V/SCE. This indicates that the estimation of RG is not valid above -0.65 V/SCE, probably because the hypothesis of a diffusion-limited current at the microelectrode is not verified at these potentials. The number of electrons exchanged at the probe increases with the potential, this is consistent with the fact that the diffusion plateau is not reached at the lowest potentials. Below -0.67 V/SCE, n_{probe} becomes even bigger than 4, which indicates that ORR is no more the only reaction happening at the tip and that proton reduction has started too. Combining these results, -0.65 V/SCE seems to be the best potential to choose for a utilization of the SECM analytical expressions as accurate as possible.

The SECM measurement protocol has been developed with the aim of being able to perform rapid measurements on several deposits. To this end, we are not intending to individualize the contribution of each catalyst particle, but we want to evaluate the global activity of the deposit. This is done by measuring the probe current above the center of the spot, while a linear sweep voltammetry (LSV) is performed at the substrate. Finally, the SECM measurements protocol can be described as follows: an approach curve is first performed in order to find the surface of the substrate, then the probe is placed at 30 µm from this surface. Few linescans are performed with the substrate polarized at 0 V/SCE in order to find the center of the deposit. Finally, the probe is placed above the center of the deposit and a linear sweep voltammetry (LSV) is performed at the substrate between 0.5 V/SCE and 0 V/SCE, while the probe is kept at its measurement potential (-0.65 V/SCE).

II.2.3. AFM characterizations

The AFM characterizations aim at measuring the size of the particles on the deposits in order to evaluate the exact volume of catalyst, as well as its agglomeration state. This information will be linked afterwards to the catalytic activity measured with SECM. After the SECM measurements, the substrate is rinsed with water and ethanol and microscope images are taken to compare the aspect of the deposits before and after SECM. Usually, the images are similar, indicating that no material detached during the SECM measurements, and that the deposit's morphology did not change by the contact with the electrolyte. AFM images are performed on a PicoLE microscope from Molecular Imaging. The key parameters are the resolution and the maximum size of the images. One image has to be small enough to capture all the particles of catalyst, and large enough to get a representative estimation of the agglomerates distribution. The scan speed and the number of images captured are also essential, with a compromise between the quality of imaging and the duration of the measurement. All these parameters depend on the microscope available to the experimenter and will strongly influence the time necessary to characterize a whole deposit. The PicoLE microscope on which this work was done is around 15 years old and its performances are rather limited compared to what a more recent AFM can achieve. Thus, the following paragraphs will present how the parameters of our AFM were adjusted to reliably image our deposits.

The resolution of the PicoLE microscope can be set to 512 pixels per line or 1024 pixels per line. Considering that doubling the resolution doubles the acquisition time for one given scan rate, the 512 x 512 resolution has been chosen. This means for example that if images of 50 µm side are performed, particles smaller than 98 nm (size of one pixel) will not be captured correctly. In our deposits, the particles have heights comprised between few hundreds of nanometers and few micrometers. SEM on CEA-BRF02 catalyst has been performed in order to determine the size of the smallest particles that can be encountered (see Figure 17 (a)). The size of these particles does not fall below 100 nm, thus it has been decided to perform mostly images of 50 µm side, and occasionally images of 100 µm side when very big particles have to be investigated. Some AFM images were compared with SEM images in order to check if the AFM captures correctly the particles. Figure 17 (b) and (c) show a SEM image and an AFM image captured in the same deposit. Even if it was not possible to find the exact same location for the two images, the distribution and the size of the particles look similar, indicating that the AFM imaging does not create any prejudicial artefact.

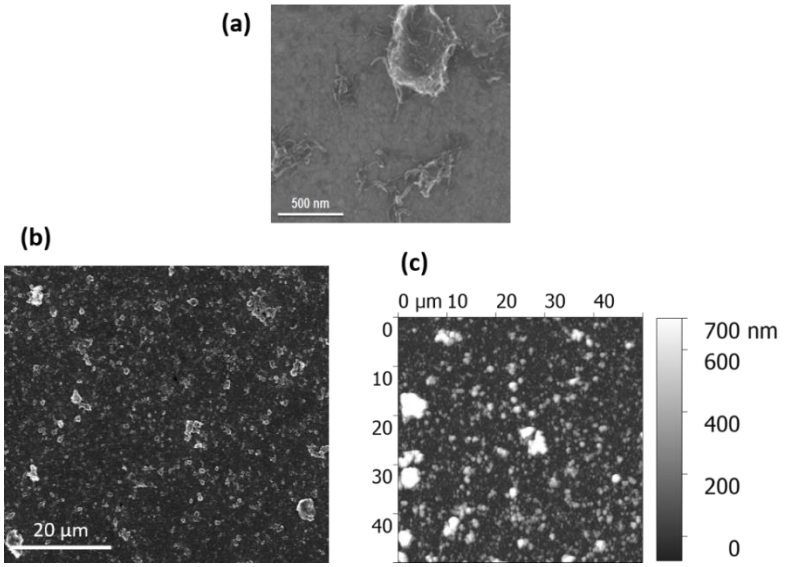

Figure 17: (a) SEM image of some of the smallest particles that can be found in the sample. (b) SEM image taken within a deposit of CEA-BRF02 catalyst. (c) AFM image taken within the same deposit. (b) and (c) show a similar distribution of particles, which confirms that AFM captures correctly the different sizes of particles.

Only few images are acquired on each deposit for the evaluation of the volume deposited and the agglomeration state. Indeed, with a size of AFM-images limited to 50 x 50 µm, it would demand too much time to capture the totality of a deposit, whose dimensions are comprised between 200 x 200 µm and 250 x 250 µm. Moreover, in order to capture properly all the particles with their very different sizes, a low scan speed is necessary. This scan speed has been chosen at 0.5 line per second for the 50 µm images (17 min for one image) and at 0.2 line per second for the 100 µm images (43 min for one image). On each AFM-image, the volumes of the particles are summed to give the volume of catalyst in the image. When several images are performed, the volumes are averaged and multiplied by the ratio between the surface of the deposit and the surface imaged by AFM to give the estimated total volume of material in the whole deposit. This estimated volume of the deposit is then plotted towards the number of AFM images captured and its variations are observed (see Figure 18). When adding an image changes the estimation of the extrapolated volume by less than 10 %, it is considered that the number of images is sufficient to get a good estimation of the volume of material in the whole deposit. With this method 4 to 6 images are necessary to characterize each deposit.

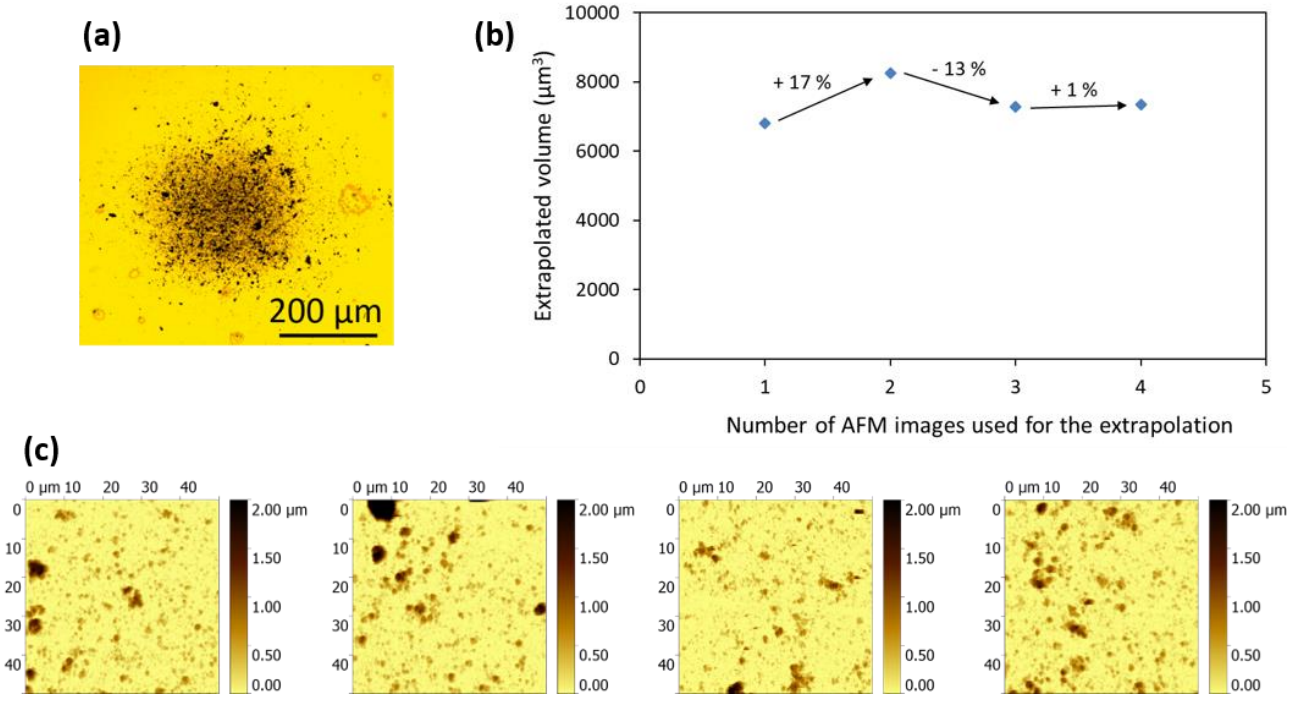

Figure 18: Illustration of how the sufficient number of AFM images is estimated. (a) Optical image of a deposit of catalyst. (b) Evolution of the extrapolated volume towards the number of AFM images acquired. (c) AFM images used for the estimation of the volume of catalyst in the deposit.

After the acquisition, the images are processed with the software Gwyddion. The catalyst particles are detected thanks to a watershed algorithm [136] implemented in the software, that consists in determining the local extremes and separate the grains. Then the height, the volume, the projected area and the external surface of each particle are exported. The distribution of particles sizes is built by defining 50 ranges of particle volume, logarithmically distributed between the smallest and the biggest volume of particle that were encountered during the experiments. A home-made Python routine is used to count the particles in each range and sum their volumes. The results for all the images are summed and multiplied by the ratio between the surface of the deposit and the surface imaged by AFM. This gives an estimation of the distribution of particles sizes for the whole deposit. Finally, the volume of catalyst in each range is compared to the total volume of catalyst, which enables to highlight the contribution of the different particles sizes towards the total volume of material. An illustration of this procedure is shown on Figure 19 and the Python routine is detailed in the Annex 1. The smallest particles are distributed with a gaussian shape and constitute slightly more than half of the total volume. The other half of the volume is formed with bigger particles discretely distributed in size. In this work, only the total volume of catalyst and the distribution of particles sizes of each deposit is discussed. But a lot of other features could be investigated using AFM data, which comprise the height, the volume, the projected

area and the external surface of each particle. For example, we could link the volume of the particles to their external surface and investigate the relationship between the morphology of the agglomerates and their size. Anyhow, the versatility of the AFM technique gives opportunities to various studies, especially for the purpose of linking the characterizations at agglomerate scale with SECM measurements.

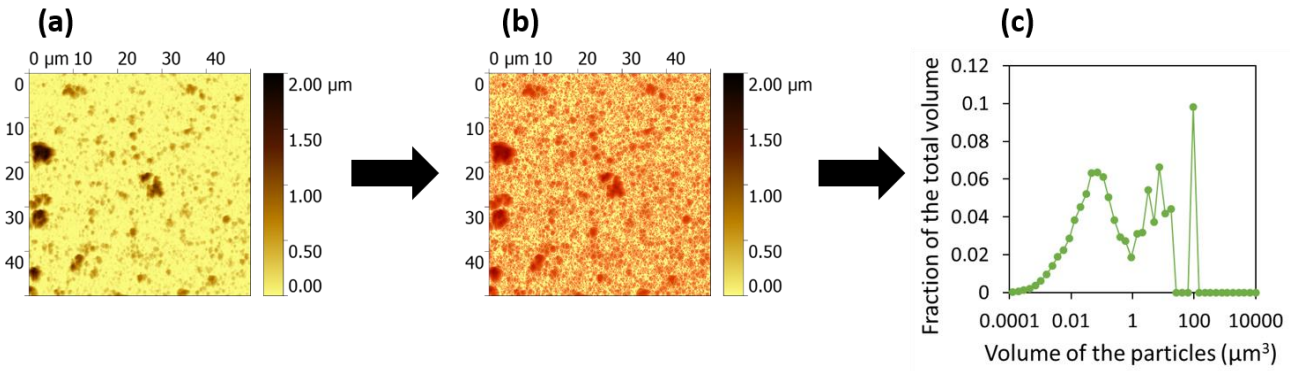

Figure 19: Illustration of how the distributions of particles sizes are obtained. (a) Pristine AFM image. (b) Detection of the particles with a watershed algorithm of the software Gwyddion. (c) Distribution of particles highlighting the contribution of the different particles sizes towards the total volume of material.

II.4. Application to ORR PGM-free catalysts benchmarking

The protocol presented above is used in the context of benchmarking catalysts from the European project PEGASUS. Three catalysts from partners of the project (Armines-CA52b, CEA-BFR02 and CSIC-Imine Fe G40), two catalysts from the member of the advisory board Pr. Zelenay (Zelenay-MOF and Zelenay-PANI), and one commercially available catalyst from Pajarito Powder are investigated (see part I.2.2). The ink formulation and the deposition protocol presented previously were optimized on the CEA-BRF02 catalyst. This protocol is applied to all the materials and the agglomeration state evaluation of the deposits enables to study how the different catalysts behave towards a same formulation and deposition protocol.

II.4.1. Morphological comparison of the catalysts

For each catalyst, deposits with different loadings are created. These deposits are identified on Figure 20 by the number of paths applied during the spraying.

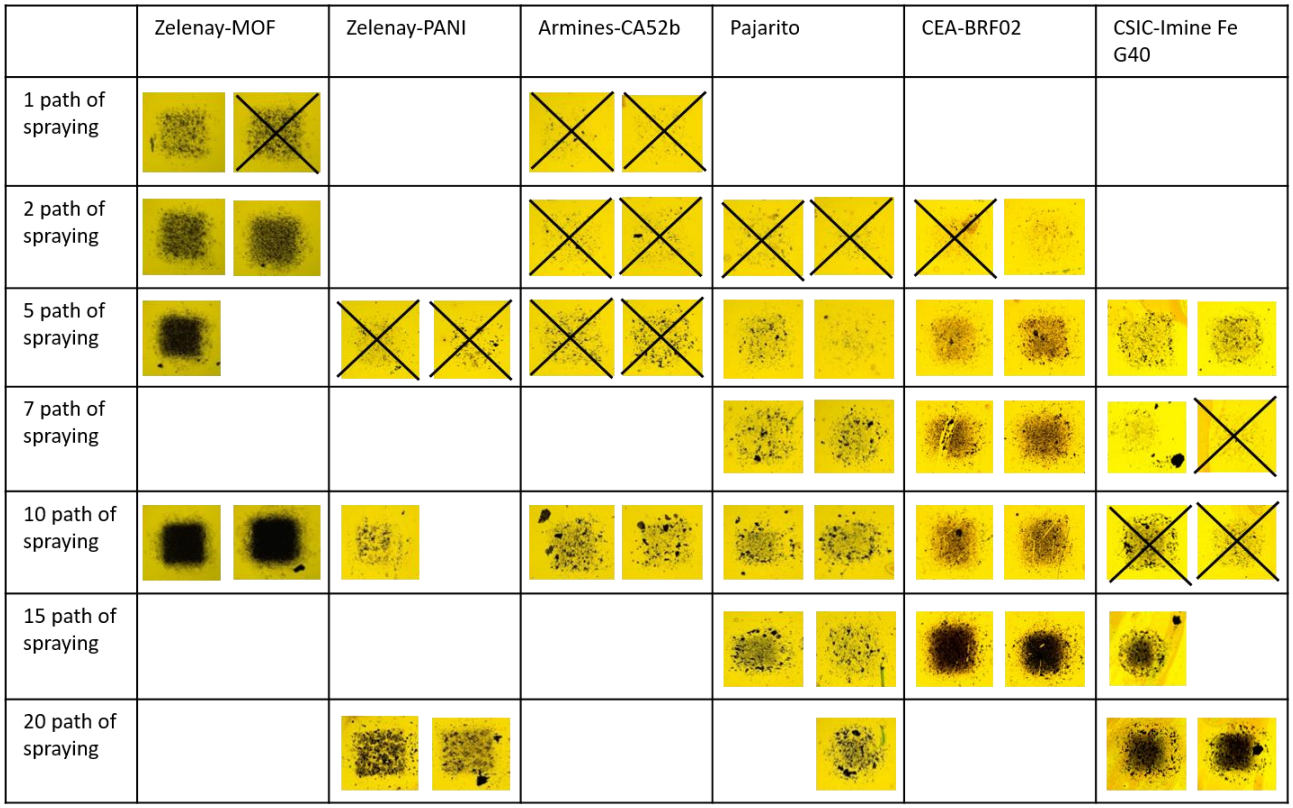

Figure 20: Microscope images of deposits of different catalysts. The loadings are identified by the number of spraying paths applied during the deposition. The crossed out deposits did not show any SECM activity and were not studied with AFM.

The deposits look very different from one catalyst to another, both in term of loading and agglomeration state. This indicates that even if the same ink formulation and the same deposition protocol were used for all the catalysts, their physico-chemical properties lead to different behaviors in term of dispersion, stability of the inks and adherence on the substrate. Notably, some sedimentation was observed in the syringe and in the tube of the ExactaCoat apparatus for the majority of the catalysts. For Zelenay-MOF however, no sedimentation was observed and this catalyst may have been better dispersed than the others, which may explain the higher apparent loadings of the deposits. The inks that mostly subject to sedimentation are the ones that lead to deposits with the biggest particles (Zelenay-PANI, Armines-CA52b and Pajarito). Indeed, big aggregates are consistent with a poor dispersion of the ink. Finally, the dimensions of the deposits are slightly bigger than the mask dimensions (200 µm side) and vary depending on the material sprayed (see Figure 21 (a)), although the same mask was used for all the catalysts. This indicates that the inks tend to spread under the mask, but differently for each catalyst because of their unique adherence properties on the substrate. All these observations lead to the conclusion that measuring the exact amount and agglomeration state of the material

actually deposited is essential for the development of quantitative measurement and standardized benchmarking of catalysts.

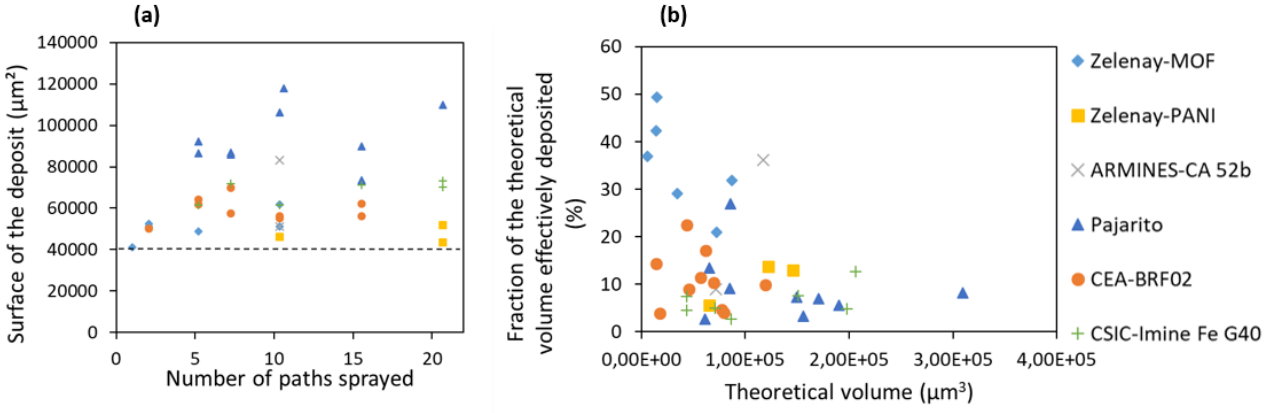

Figure 21: (a) Surface of the deposits, the dashed line represents the surface of the mask. (b) Fraction of the theoretical sprayed volume that was effectively deposited on the substrate.

After the SECM measurements, AFM is performed on the deposits that show sufficient catalytic activity. The volume of material deposited on the substrate is extracted from the AFM images. In order to compare this value with the theoretical volume given by the amount of ink sprayed, an assumption needs to be done regarding the density of the deposited material. Indeed, the concentration in the ink is measured in $g.L^{-1}$. As the different PGM-free materials studied here have very different morphologies (see Figure 4 in part I.2.2.), the porosity of the particles deposited on the substrate may differ depending on the catalyst. For simplicity, this theoretical volume is calculated from the theoretical loading in $\mu g.cm^{-2}$ with the hypothesis of a particles density of 2 $g.cm^{-3}$, which is the density of carbon with no porosity [137]. In reality, the density can be lower and the assumption leads to a small underestimation of the theoretical volume of material deposited. The volume of material measured by AFM on each deposit is compared to the theoretical volume on Figure 21 (b). The fraction of catalyst effectively deposited is rather low and depends on the material and on the loading. Expressed in $\mu g.cm^{-2}$, the loadings of the deposits are comprised between 4 $\mu g.cm^{-2}$ and 90 $\mu g.cm^{-2}$. This confirms that there is some decantation in the Sonotek syringe and hose and that this decantation is different for each catalyst. The effect of the ink decantation is more important for the high loadings, probably because they take a longer time to be produced. The low fraction of ink effectively deposited can also be caused by the spread of the ink in the home-made device enabling the deposition on one micropattern at a time, or by the rinse of the substrate after the deposition which aims to remove the particles with a poor adherence. The very low amount of Nafion in the ink (5 % wt) is certainly responsible for the decantation phenomenon. In a context of a comparison of the intrinsic activities of the catalysts, this is not problematic as long as AFM is performed

to measure the exact volumes deposited. However, if the aim of the study was to optimize an ink formulation, it would be interesting to compare the AFM-measured distribution of particles sizes with the distribution in the ink, measured with dynamic light scattering (DLS) for example. Indeed, it must be kept in mind that the distribution of particles sizes in the sprayed fraction of the ink may differ from the distribution of the original ink.

Using the method detailed above, the AFM images of all the deposits are processed in order to obtain their distributions of particles sizes (see Figure 22). For one given catalyst, the distributions are averaged in order to get a mean distribution, which will serve as reference for the comparisons.

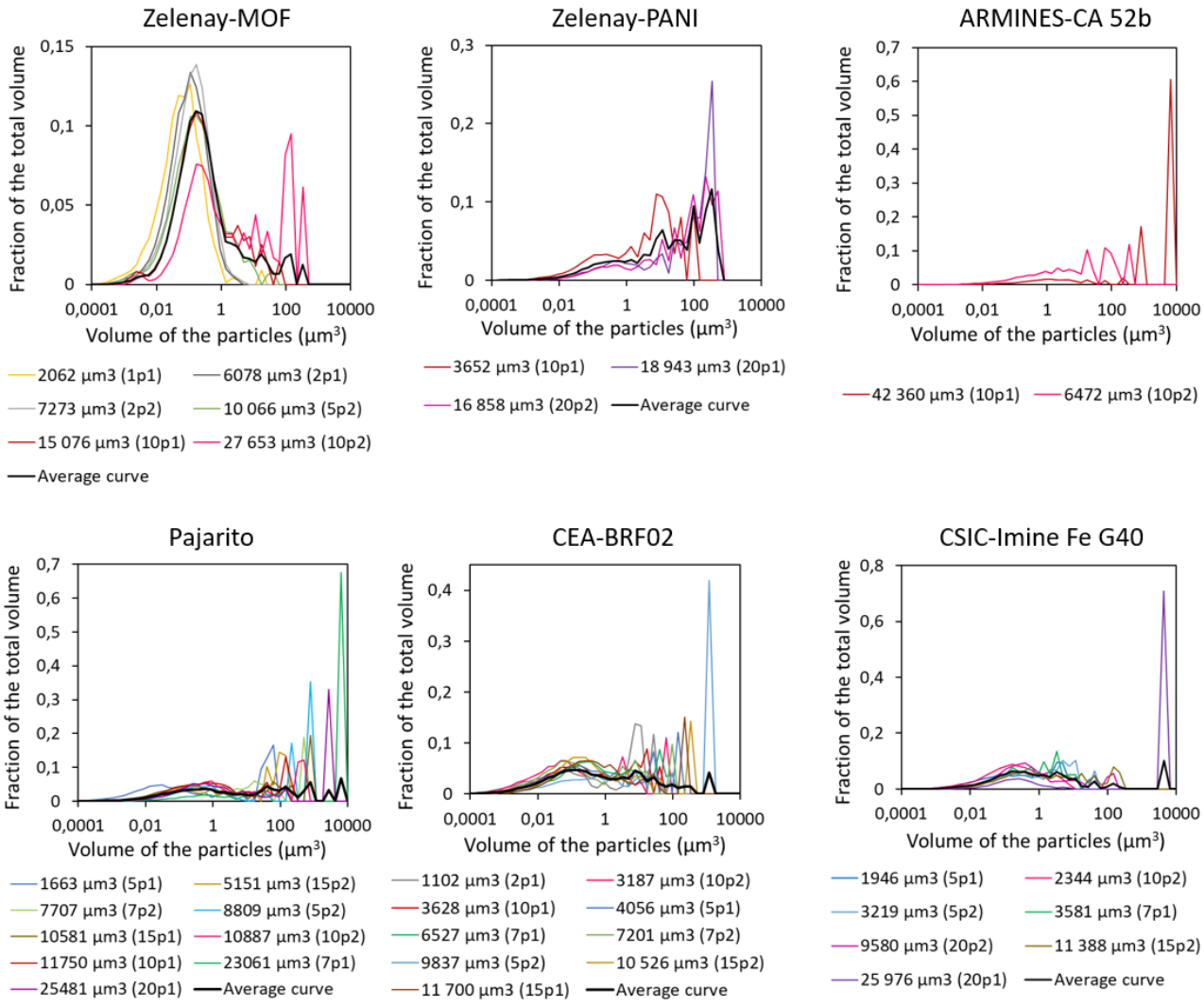

Figure 22: Distributions of particles sizes of the deposits from the different catalysts.
An average distribution is shown for each catalyst.

II.4.2. Link between electrochemical performance and agglomeration state

The results of the SECM measurements for the different catalysts are presented on Figure 23 where the normalized probe current is plotted towards the substrate potential. In redox competition mode, the probe measures the depletion of oxygen caused by the ORR at the catalyst. Hence, by normalizing the recorded current by its value when no polarization is applied to the substrate, the curves give a representation of the catalytic activity towards the applied potential. This activity increases when the substrate potential decreases, and it increases also with the loading.

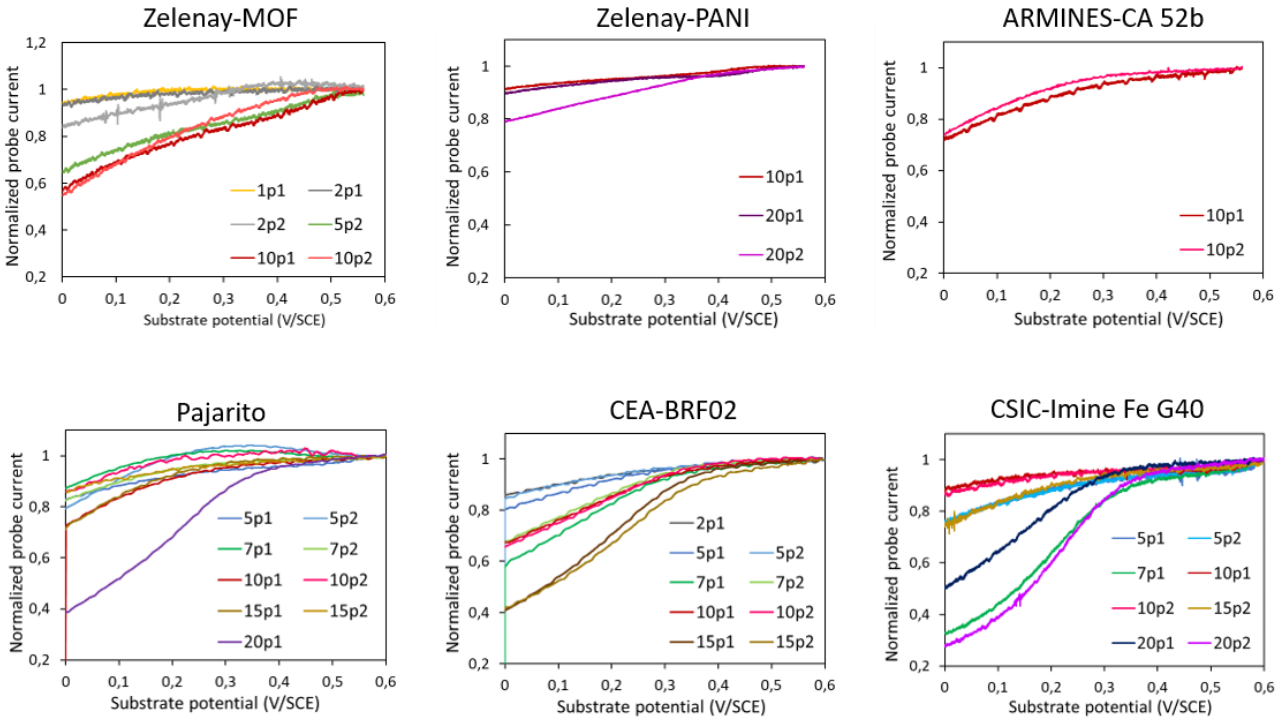

Figure 23: SECM characterization of the deposits from the different catalysts. SECM experiments were performed with a gold probe (rT≈12,5 µm, RG≈10, E_{probe}=-0.45 V/SCE) in a H_2SO_4 50 mM solution saturated with oxygen and a distance probe-substrate of 30 µm. A LSV was applied at the substrate from 0.6 V/SCE to 0 V/SCE with v_{scan}=2 mV/s. The probe current is normalized by its value at $E_{subsrate}$=0.6 V/SCE.

In order to link the catalyst electrochemical performances to the AFM characterizations, the onset potential of ORR is extracted from each curve. This onset potential is defined as the potential at which the probe normalized current falls below 90 % of its initial value. It is considered as an indicator of the electrochemical performance of each deposit, the higher it is, the more active is the catalyst. A more quantitative analysis of the results (with the support of numerical simulation) will be presented in the next

chapter. Some deposits with a very low activity did not reach 90 % of the initial probe current in the potential range investigated. No onset potential could be defined for these deposits, which are not further studied (Zelenay-MOF 1p1 and 2p1, Zelenay-PANI 10p1). Thus, at this stage, the Zelenay-PANI and ARMINES-CA 52b catalysts do not contain enough exploitable deposits to link their agglomeration state to their catalytic activity. For the Zelenay-MOF, Pajarito, CEA-BRF02 and CSIC-Imine Fe G40 catalysts, the onset potential is plotted towards the AFM-measured volume of catalyst (see Figures 24(a), 25(a), 26(a) and 27(a)). An increase of this potential with the volume is observed. Indeed, the AFM-measured volumes are directly related to the loadings of the deposits. For each catalyst, most of the points follows a linear trend, with few points deviating from this global tendency. To explain these deviations, the distributions of particles sizes of the deposits leading to departure from linearity are compared to the averaged distribution of sizes of all the catalyst deposits. After a careful analysis, we conclude that most of the cases belong to one of the two following situation: if a very big particle is present on the deposit, its inner volume is certainly not active towards ORR, thus the AFM-measured volume overestimates the catalytically active volume in the deposit, leading to a lower activity than the global tendency (see Figures 24(e), 25(c) and (d), 26(d) and 27(b), (c) and (d)). On the contrary, if the deposit shows a bigger proportion of small particles in its distribution, one can suppose a better accessibility of the active sites, which explains the higher activity of the deposit compared to the ones in the global tendency (see Figures 25(b), 26(b) and (c)).

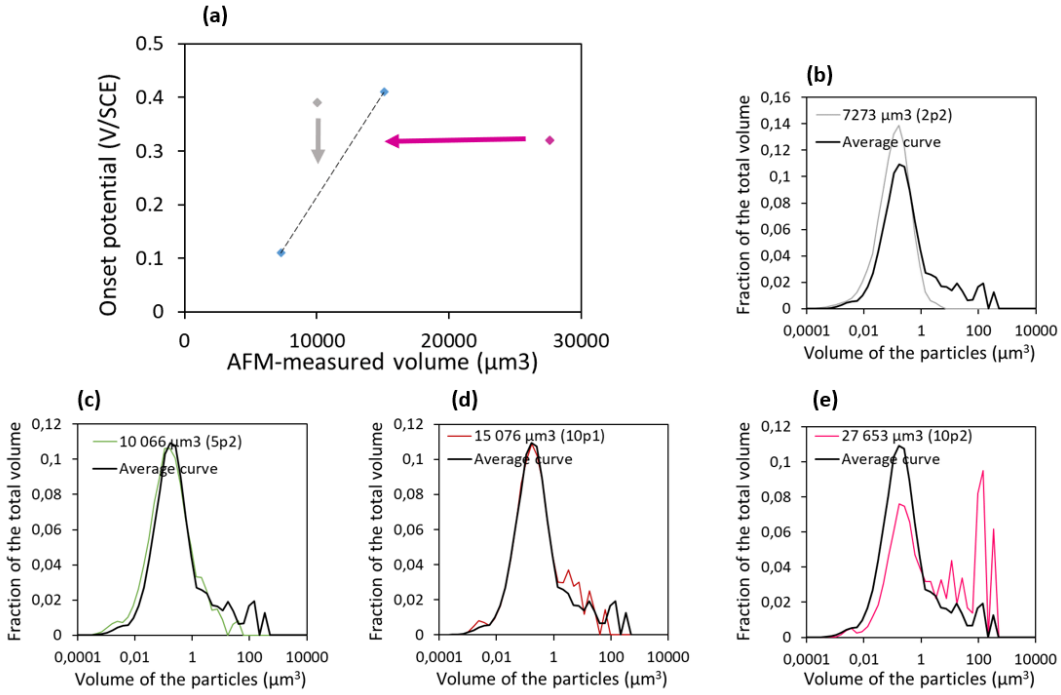

Figure 24: Electrochemical performance of Zelenay-MOF catalyst linked with the agglomeration state of the deposits. (a) Onset potential towards the volume of catalyst. (b), (c) and (d) Distributions of particles sizes of the three points deviating from the trend in (a) and comparison to the average distribution of all the deposits.

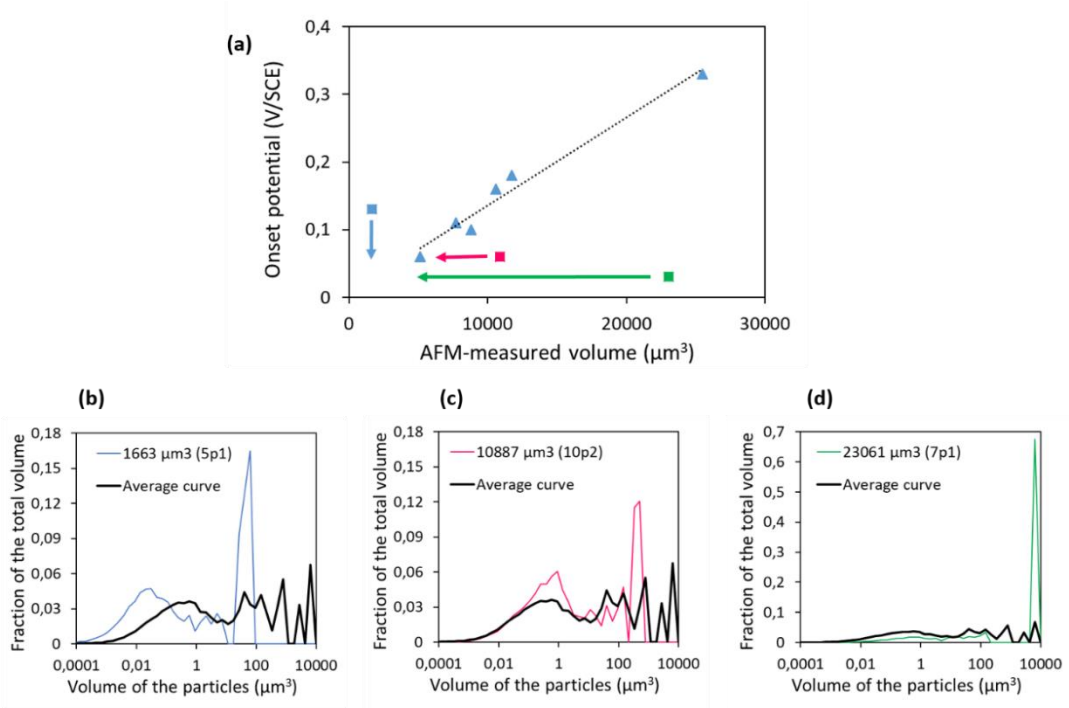

Figure 25: Electrochemical performance of Pajarito catalyst linked with the agglomeration state of the deposits. (a) Onset potential towards the volume of catalyst. (b), (c) and (d) Distributions of particles sizes of the three points deviating from the trend in (a) and comparison to the average distribution of all the deposits.

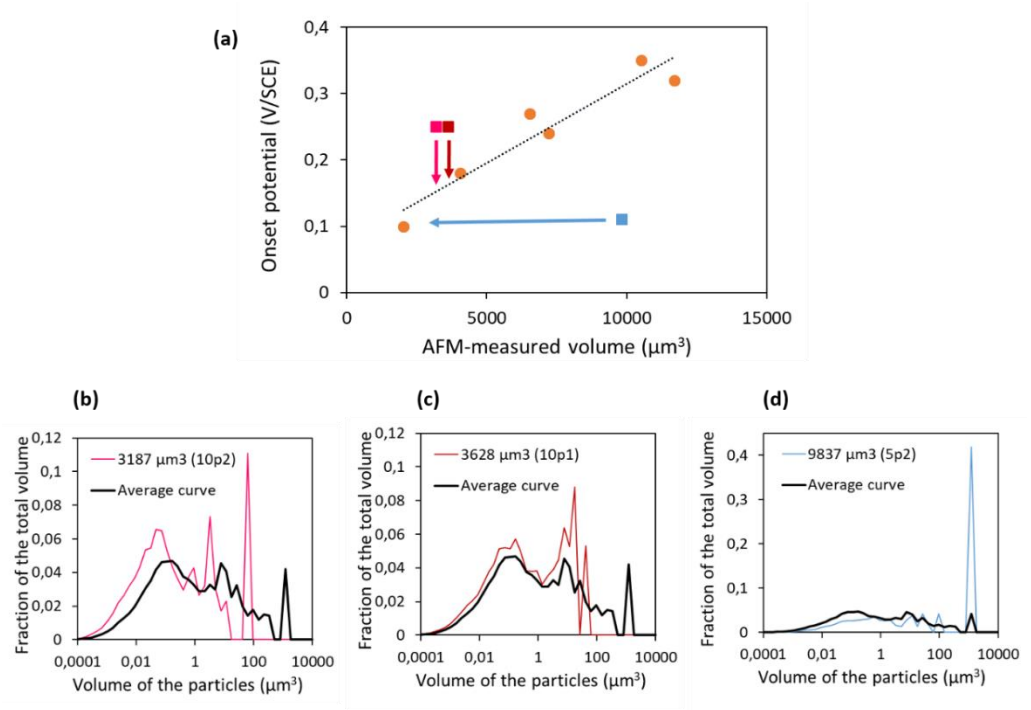

Figure 26: Electrochemical performance of CEA-BRF02 catalyst linked with the agglomeration state of the deposits. (a) Onset potential towards the volume of catalyst. (b), (c) and (d) Distributions of particles sizes of the three points deviating from the trend in (a) and comparison to the average distribution of all the deposits.

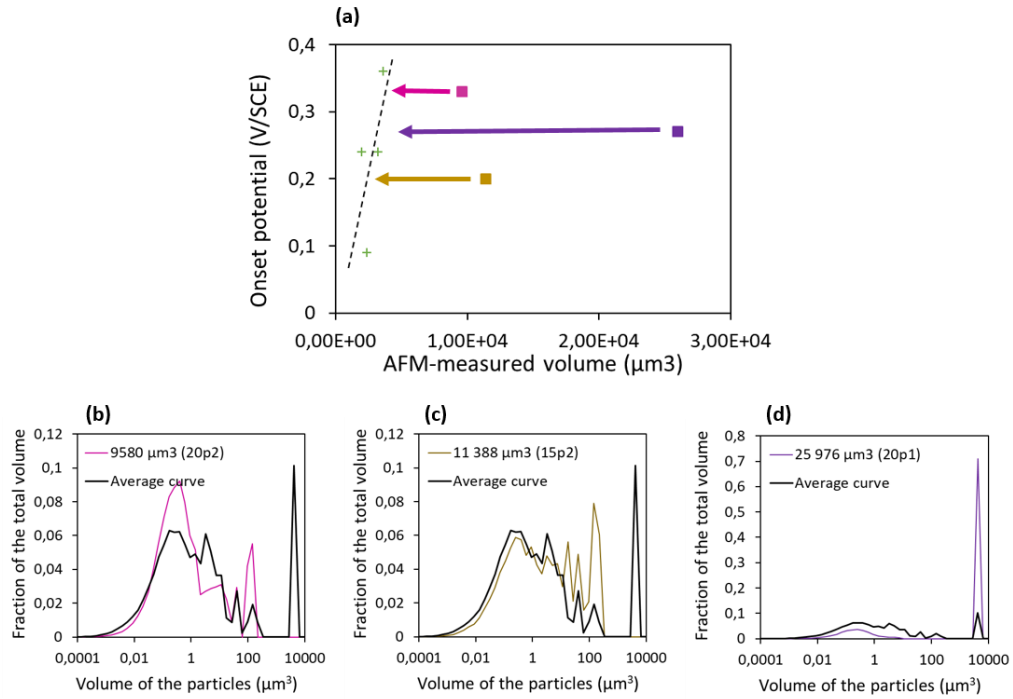

Figure 27: Electrochemical performance of CSIC-Imine Fe G40 catalyst linked with the agglomeration state of the deposits. (a) Onset potential towards the volume of catalyst. (b), (c) and (d) Distributions of particles sizes of the three points deviating from the trend in (a) and comparison to the average distribution of all the deposits.

II.4.3. Comparison of the catalysts performances

At this stage, four catalysts have enough exploitable deposits to highlight the tendency linking the catalytic activity to the volume of material deposited (Zelenay-MOF, Pajarito, CEA-BRF02 and CSIC-Imine Fe G40). These tendencies are now plotted on the same graph in order to compare the performances of the catalysts (see Figure 28 (a)). The deviating points that were analyzed in the last paragraph have been removed here. The major difference between the catalysts is the slope of the curves, and this amplifies the performance differences observed at low loading. The different slopes of the curves can be explained by the different agglomeration states of the catalysts. When the catalyst is more dispersed, a larger fraction of the catalytic sites present in the volume deposited is accessible to the ORR reactants, leading to a rapid growth of the activity with the volume. On the contrary, if the particles are bigger, a significant part of their core will be inactive towards ORR, and increasing the volume of material on the deposit will have a lower impact on the activity, and consequently on the slope of the curve. This is confirmed by the distributions of particles sizes showed on Figure 28 (b). CSIC-Imine Fe G40 has the second biggest proportion of small particles and the steeper slope on Figure 28 (a). Then, CEA-BRF02 has slightly less little particles and a less steep slope, and Pajarito has the biggest particles and the flattest slope. With only two data points, the Zelenay-MOF catalyst is difficult to analyze properly, but its distribution of particles sizes and the steep slope formed by the two exploitable deposits indicate that this catalyst is very well dispersed.

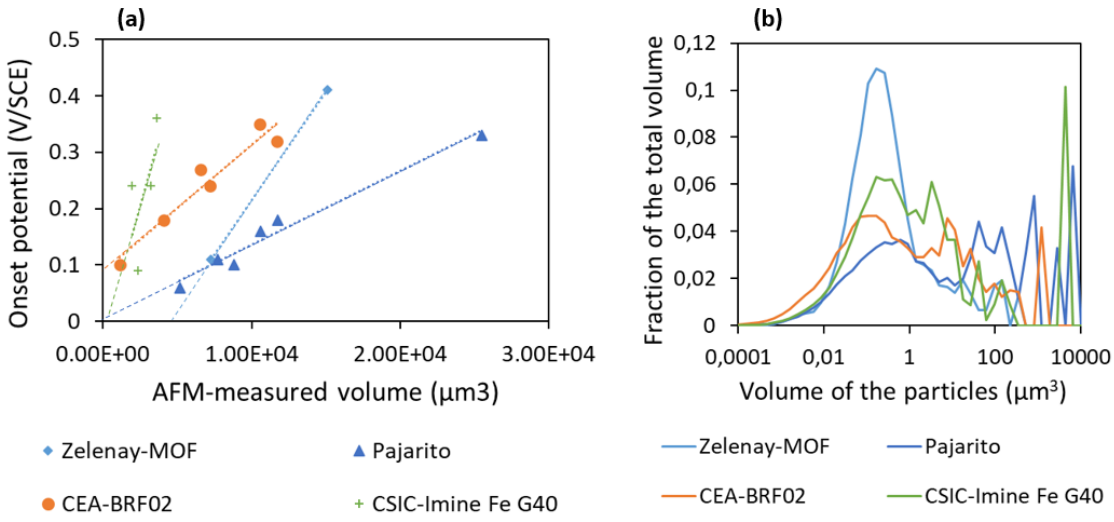

Figure 28: Comparison of (a) the electrochemical performances and (b) the distributions of particles sizes of the four exploitable catalysts.

The other parameter that can be extracted from the Figure 28 is the intrinsic activity of the catalysts. This value can be defined by the activity at very low loading, when the material is so dispersed that all the catalytic sites can be considered as accessible to ORR. Here, the material with the highest intrinsic activity is the CEA-BRF02, followed by CSIC- Imine Fe G40 and Pajarito, then by Zelenay-MOF.

This study shows that the formulation and deposition process of a material has a strong influence on its performance, even at agglomerate scale. Here, the important differences of agglomeration of the materials make the comparison of their performances very delicate. Even if the intrinsic activity can be observed at very low loadings (around 1500 μm^3 or 5 $\mu g/cm^2$), the different agglomeration states of the materials start to have a non negligible effect on the performances above 1 x 10^4 μm^3 or 35 $\mu g/cm^2$. It would be interesting to work on the formulation of the inks in order to obtain a similar agglomeration state for each material before comparing their performances. The first steps in this direction are presented in the following section.

II.5. Influence of Nafion content and dispersion method

The study of the different catalysts presented in the last part highlighted the ability of the method to investigate experimentally the link between the catalytic activity and the dispersion of a material at agglomerate scale. However, a strong effect of the agglomeration state on the performance was observed even at the low loadings investigated with the method. Hence, it is interesting to identify the parameters that influence the agglomeration state of the deposits. In this regard, some supplementary experiments have been performed on the CEA-BRF02 catalyst, investigating the proportion of Nafion in the ink and the dispersion method. Inks with 5 % wt, 25 % wt and 45 % wt of Nafion were prepared by dispersing the catalyst powder and the Nafion in an isopropanol/water (1:1) solvent. Two methods of dispersion were compared: a dispersion under sonication and a ball milling dispersion. The dispersion under sonication consists in dispersing the catalyst powder and the Nafion in 1 mL of solvent and let it under sonication during 5 min. Afterwards, the total volume of solvent is increased to 2 mL and the sonication process is repeated. The process is repeated by increasing progressively the total volume of solvent to obtain a catalyst ink concentration of 0.2 $g.L^{-1}$. The second method of dispersion consists in adding Zirconium balls with a diameter of 1 mm to the ink. The ink is then placed for 1 h in a IKA ULTRA-TURRAX® Tube Drive for a first grinding, before being let for one week on a IKA ROLLER 6 shaker. During this time, the balls disperse the suspension.

Finally, six different inks have been prepared, and four deposits of each ink were sprayed and characterized with SECM and AFM. Figure 29 shows the microscope images of these deposits. The deposits obtained with the ink dispersed by ball milling and with 5 % wt of Nafion are very inhomogeneous and look different from all the other deposits. This indicates that something misfired during the preparation or the deposition of the ink. For this reason, these deposits were not further studied.

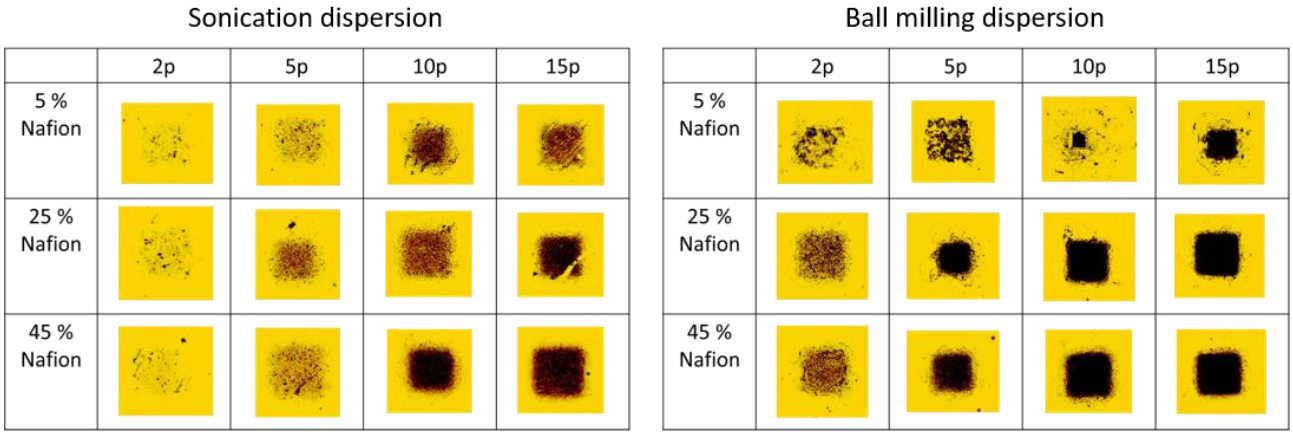

Figure 29: Microscope images of deposits obtained with inks prepared by two different dispersion methods and with three different Nafion contents.

Thanks to the AFM measurements and similarly as before, the volume of material effectively deposited is compared to the theoretical volume and the distributions of particles sizes are plotted (see Figure 30). The proportion of Nafion in the inks seems to not have a lot of influence on the distributions of particles sizes. This little influence of the Nafion content on the agglomeration could seem unexpected since Nafion aims at improving the dispersion of the powder in the ink and reducing the number of big particles. However, Figure 30 (d) shows also that the fraction of catalyst effectively deposited increases with the proportion of Nafion. Thus, we can imagine the following scenario: when the ink contains a few amount of Nafion, big particles are present initially but decant in the Sonotek hose. These particles are not sprayed on the substrate and they are not taken into account in the distribution of particles sizes determined with the AFM measurements. When a higher proportion of Nafion is incorporated in the ink, the catalyst is better dispersed and less big particles are present. Thus, a larger fraction of the material initially present in the ink is sprayed on the substrate. Moreover, increasing the fraction of Nafion may improve the adherence of the material on the substrate. The AFM measurements will show a higher volume of material on the deposit but the distribution of particles sizes may not differ from the first case, since the particles above a certain size are not sprayed on the substrate in both cases. This scenario corresponds to the observation done on Figure 30, where the fraction of catalyst effectively

deposited increases with the amount of Nafion, but with no clear modification of the distributions of particles sizes.

As concerns the dispersion method, an influence on the volume effectively sprayed and on the agglomeration state of the deposits is noticed on Figure 30 (c) and (d). As more material is deposited on the substrate with the inks prepared by ball milling than with the inks prepared by sonication, we can conclude that the grinding by ball milling is the more efficient method. This method leads also to deposits with a slightly different distribution of particles sizes compared to the deposits prepared by sonication: the proportion of smaller and medium-sized particles is predominant and the amount of bigger particles is lower.

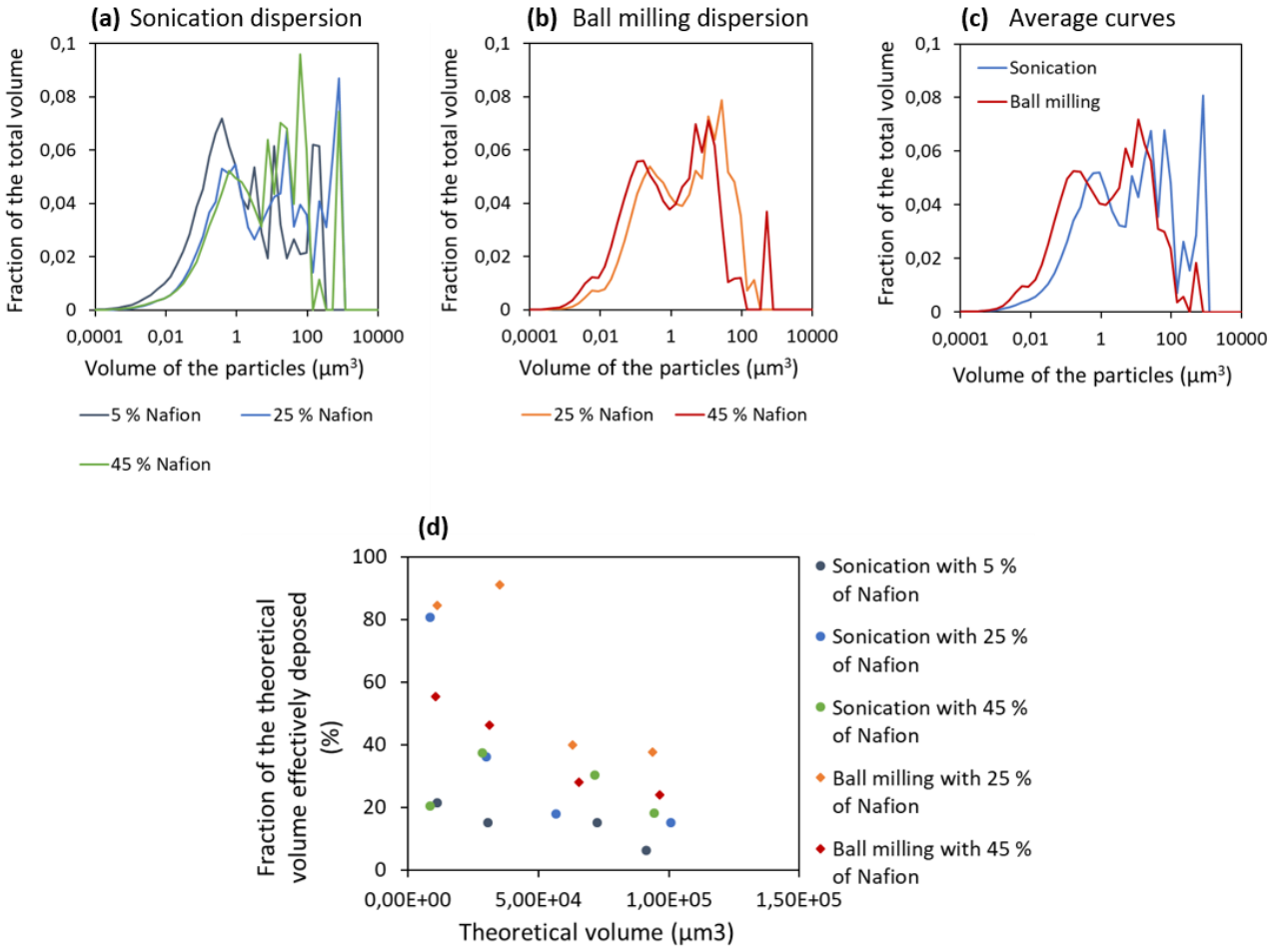

Figure 30: (a) and (b) Distributions of particles sizes for deposits obtained with inks prepared with different dispersion methods and different proportions of Nafion. (c) Distributions obtained by averaging the curves at different Nafion content for each dispersion method. (d) Fraction of the theoretical sprayed volume that was effectively deposited on the substrate.

The electrochemical performances of the different deposits are then compared. The onset potentials of the SECM measurements are plotted towards the AFM-measured volumes of material in Figure 31. The inks studied in this part are compared to the deposits of the CEA-BRF02 catalyst presented in the last part. All the inks are following the same trend than the CEA-BRF02 catalyst (whose ink was prepared under sonication and with 5 % wt of Nafion). Only one point deviates from the trend because of its slightly different agglomeration state (see Figure 31 (b)). The effects of the Nafion content and the dispersion method are visible on the volume deposited but do not seem to influence the activity trend of the deposits. For the more loaded deposits, this trend stabilizes at a plateau. Indeed, the onset potential of the catalyst cannot become higher than the open circuit potential, which is measured around 0.52 V/SCE.

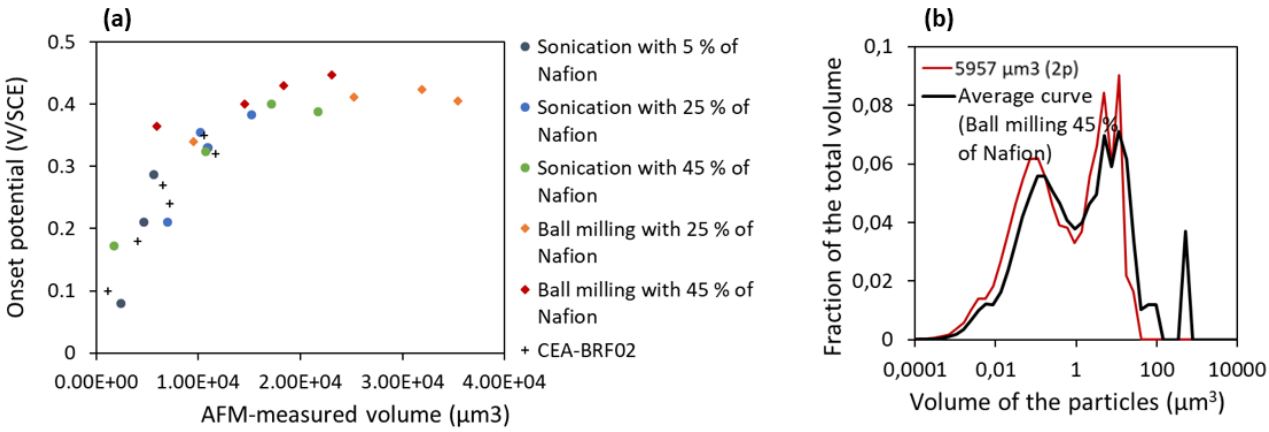

Figure 31: (a) Onset potential of the deposits towards the volume of catalyst. The previously studied series of CEA-BRF02 catalyst is added to the data. Distribution of particles sizes of the point deviating from the tendency, compared to the averaged distributions of the deposits made with the same ink.

Finally, the amount of Nafion in the ink and its dispersion method affect mostly the fraction of catalytic material that is effectively sprayed on the substrate. The effect of the ink fabrication on the agglomeration state of the deposits is less relevant since a non negligible fraction of the particles remains in the Sonotek apparatus during the spraying process. Because of this specificity of our protocol, no difference due to the ink fabrication could be observed on the electrochemical activity, once this activity is related to the volume of material present on the deposit. In this study, only one over the twelve deposits showed a different activity caused by a different agglomeration state. This indicates that the deposition method was better controlled during these experiments.

II.6. Conclusion

In this chapter, we have developed and employed a new methodology for the characterization of catalysts at agglomerate scale. SECM was used to characterize the global electrocatalytic activity and AFM to determine the exact volume of material on the deposits, as well as their agglomeration state. Several PGM-free catalysts from the European project PEGASUS were compared through the same protocol of ink formulation and deposition. However, the different physico-chemical properties of the catalysts led to different agglomeration states of the deposits, and to a different collection efficiency of the sprayed material. It was highlighted that, when the loading is increased, the agglomeration state is predominant on the differences of activities. The influence of the intrinsic activity is visible only at very low loading. The effect of the dispersion method and of the Nafion content were investigated on the material developed in the LICSEN. The decantation in the Sonotek affects the amount of material deposited on the substrate. As long as the catalytic activity was expressed towards the exact volume of material measured with AFM, this phenomenon did not affect the investigation of the activity of the catalysts.

This methodology offers a new playground for the characterization of catalysts at agglomerate scale with various possible applications. Some efforts remain to be done to fully control the formulation and deposition protocol. For the purpose of investigating the intrinsic activity of a pristine material, only 5 % wt of Nafion can be added in the ink and the AFM measurement of the volume deposited will compensate the fact that a large part of the material remains in the Sonotek apparatus. If the aim is to study a given ink formulation and its effect on the agglomeration state of the material, the deposition process needs to be carefully considered in order to limit the fraction of the material that is not sprayed on the substrate.

Chapter III

Determination of kinetic parameters from SECM measurements

The chapter II showed the development and the utilization of a methodology based on SECM and AFM for characterizing PGM-free ORR catalysts at agglomerate scale. This methodology enables to study the material at very low loading and is thus adapted for investigating the intrinsic activity of a catalyst. The intrinsic activity is measured when all the catalytic sites are accessible to the reaction, it depends only on the ORR kinetic limitations and on the selectivity of the material. With our set-up where the agglomerates are dispersed on a substrate, the only losses that can result from other phenomena than kinetic limitations on the catalyst, are transport losses within the agglomerates or connection resistances between the particles and the substrate. Hence, with agglomerates having a limited volume, the activity measured with SECM should be close to the intrinsic activity of the catalyst. Two parameters characterizing the intrinsic activity will be investigated in this chapter. First, the exchange current density i_0 which reflects the intrinsic rate of electron transfer by the reaction will be determined. Then, the selectivity of the ORR (whose importance was mentioned in part I.2.2.) will be investigated by considering the global number of electrons transferred per O_2 molecule at the catalyst n_C. To this end, the protocol of SECM characterization will be completed by measurements in SG-TC mode in order to probe the amount of H_2O_2 produced by the deposits. Then, a numerical model of the SECM set-up will be developed in order to extract the above-mentioned parameters. Finally, the parameters obtained with this procedure will be analyzed in a last part.

III.1. SECM protocol in SG-TC mode

In order to be able to characterize the selectivity of the ORR, it is important to measure with SECM the amount of H_2O_2 generated by the ORR. A protocol of SECM characterization in substrate generation-tip collection (SG-TC) mode probing the concentration of H_2O_2 above the deposit has been developed in collaboration with another PhD student in the LICSEN, Ndrina Limani. Briefly, a platinum probe is polarized at 0.9 V/SCE while a LSV from 0.5 V/SCE to 0 V/SCE is applied to the substrate. In this way, the deposit undertakes the ORR while the probe measures the production of H_2O_2. In order to be able to use the SG-TC measurements in the models, it has been verified that the chosen probe potential for H_2O_2 oxidation corresponds to a diffusion limited plateau. Practically, the measurements in RC mode are first performed on all the deposits, then the gold probe is replaced by the platinum probe and the measurements in SG-TC mode are recorded. This protocol has been used during the experiments presented in part II.5. In the last chapter, only the measurements in RC mode were investigated. Here, the measurements in both RC and SG-TC mode will be considered in order to extract values for i_0 and n_C. Figure 32 shows the curves obtained for one of the ink formulations investigated during the experiments.

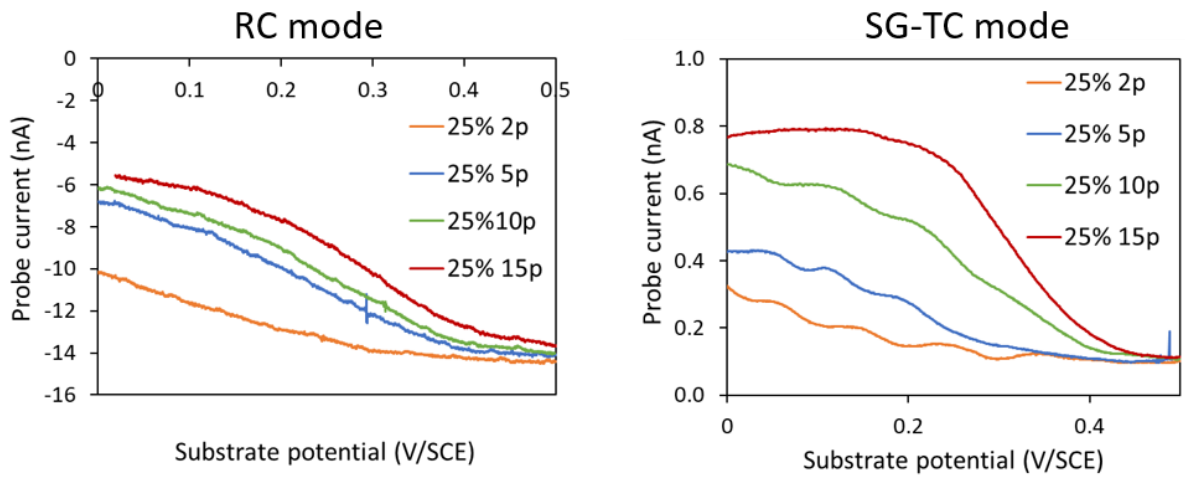

Figure 32: Example of SECM measurements in RC and SG-TC modes (ink dispersed by ultrasonication with 25 % wt of Nafion).

III.2. Numerical modeling of the SECM experiment

In order to extract kinetic parameters with the greater accuracy, a 2D numerical model of the SECM set-up has been developed on Comsol Multiphysics®. Before presenting the model developed in this work, a brief review of the literature about SECM modeling will be conducted. Then, the validity of the 2D approach will be discussed by comparing it with a 3D model.

III.2.1. SECM modeling in the literature

In order to extract quantitative information from SECM measurements, modeling approaches of the transport and kinetic phenomena occurring during the experiment have been developed by the scientific community. After the pioneer works by Bard, Mirkin and Unwin [138], [139], [140], several theoretical works established analytical expressions describing the general operation of SECM. For example, the correction factor $\beta(RG)$ applied to the diffusion limited current at a microdisk microelectrode with finite dimensions (see Eq. (12)) has been expressed in different ways [68], [141], [142]. Analytical expressions for approach curves in negative and positive feedback mode have been developed by Renaud Cornut and Christine Lefrou [69], [141] and are henceforth widely used by the community. Other expressions have been established to express the probe feedback current with an homogeneous reaction is solution [143] or heterogeneous kinetics at the substrate. They served notably to study semiconductors [144], catalytic materials [145] or the enzymatic behavior of glucose oxidase [146], [147]. Considering the study of ORR kinetics, the rate constants of the two pathways of ORR (see Eq. (4) and (5)) were fitted thanks to an analytical expression of the transient probe current when potential pulses were applied to the substrate in SG-TC mode [148]. The group of Schuhmann developed a methodology derived from the Koutecky-Levich approach used for RRDE measurements to calculate the heterogeneous electron transfer rate and the amount of H_2O_2 generated during the ORR at PGM-free catalysts from RC-SECM measurements [149], [150].

Nowadays, the majority of the quantitative studies on SECM are using numerical models based on finite element analysis. These numerical models enable to consider complex geometries for the probe [151], [152] and the substrate [153], or different operation modes and instrumentation [154], [155], [156]. The positive feedback mode is the most investigated and the simulations serve principally to determine electron or mass transfer kinetics. For example, Li and Unwin calculated the rate constant of photoinduced electron transfer at

liquid/liquid interfaces [157]. Yao et al. unraveled the mass and electron transfer at silica nanomembrane modified electrodes [158], while Hossain et al. resolved the mass transport properties in lithium battery electrodes [159]. The mechanisms of HER [160] and HOR [161] were also investigated with positive feedback SECM coupled with numerical models. Fewer models are existing on the generation/collection modes but they serve also to study kinetic mechanisms, for instance of HER [162], [163]. Although very few simulations are reported in RC mode in the field of material science [164], this mode is more widely investigated through modeling in the biological field. Indeed, the RC mode is adequate for resolving the oxygen consumption by living organisms such as living cells [165], worms [166] or even tumors [167]. The kinetics of the ORR catalyzed by the glucose oxidase enzyme have been investigated by several groups thanks to simulation assisted RC-SECM measurements [168], [169].

III.2.2. Numerical model developed in this work

In this chapter, we propose a numerical model of our SECM set-up in order to simulate experiments in negative feedback, RC and SG-TC modes. It will be used to fit experimental data such as approach curves or substrate LSV measurements. During SECM measurements, three steps can be considered: the consumption/production of reactive species at the substrate, the diffusion of these species in solution, and their detection at the probe. The space between the probe and the substrate is modeled in order to be able to link the current measured at the probe to the consumption/production at the substrate. The square shaped deposits of catalyst are approximated by disks of radius $r_C = \sqrt{\frac{S_{deposit}}{\pi}}$, which allows to build a 2D axisymmetric model. The validity of this hypothesis will be discussed in the part III.2.3. The transport of an active specie X in solution is due to diffusion (X can be O_2 or H_2O_2):

$$D_X \nabla C_X = \frac{dC_X}{dt} = 0 \qquad (16)$$

as the simulation is performed at a steady state. Since the probe is polarized in the diffusion limited plateau, the boundary condition at the active part of the probe is:

$$C_X = 0 \qquad (17)$$

There is a zero flux boundary on the probe glass walls and on the parts of the substrate not covered with catalyst. A concentration boundary equal to the initial bulk concentration C_0 is set in the limits of the simulation

area. At the active part of the substrate (which represents the deposit of catalyst), the boundary condition depends on the mode of SECM that is simulated. In negative feedback, a zero flux boundary is set on the totality of the substrate. In redox competition, a flux of O_2 consumption is defined at the part of the substrate covered with catalyst and the probe consumes O_2 too. In SG-TC, a flux of H_2O_2 production is defined at the part of the substrate covered with catalyst and the probe consumes H_2O_2. The simulation parameters and the boundary conditions corresponding to the different modes of SECM are summarized in Annex 2. In all cases, the consumption and transport of protons are not modeled since the concentration in H_2SO_4 is much higher than the concentrations in O_2 or H_2O_2. The currents at the probe (i_T) and at the catalyst deposit (i_C) are evaluated by integrating the flux of X at the considered boundaries:

$$i_T = 2\pi n_T F \int_0^{r_T} D_X \frac{\partial C_X}{\partial z}|_{z=d} r dr \quad (18)$$

$$i_C = 2\pi n_C F \int_0^{r_C} D_X \frac{\partial C_X}{\partial z}|_{z=0} r dr \quad (19)$$

with r_T the radius of the probe's active part, n_T the number of electrons exchanged at the probe, r_C the radius of the catalyst deposit, n_C the number of electrons exchanged at the catalyst, and with d the distance between the probe and the substrate. Figure 33 shows an illustration of the model.

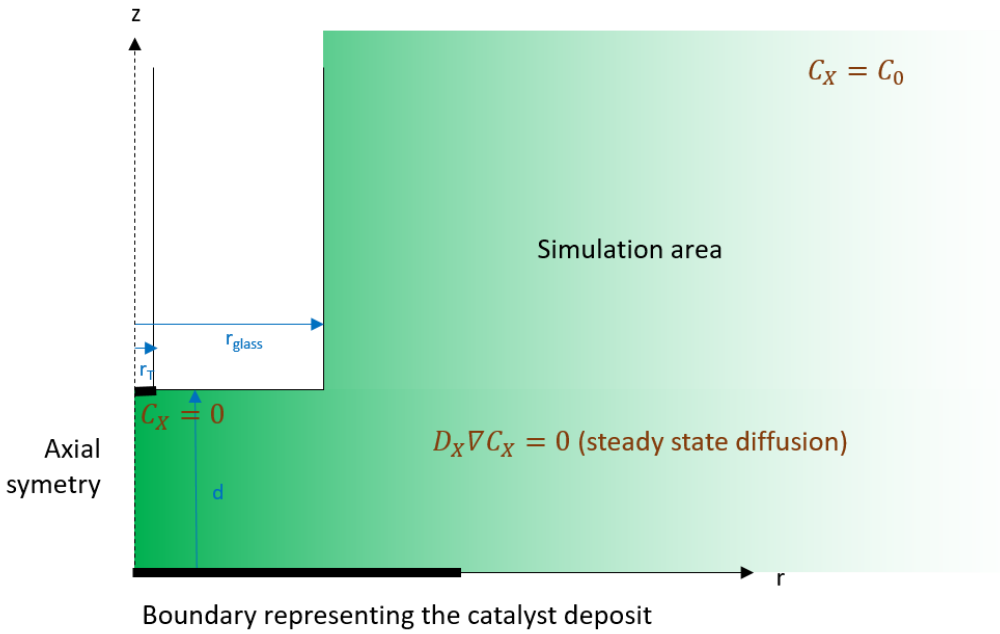

Figure 33: Illustration of the model developed to simulate SECM measurements.

The model is implemented in Comsol Multiphysics® v.5.4 for solving the different equations with the finite elements method. In the cylindrical coordinates, the substrate surface is set at $z = 0$ and the center of the microelectrode is set at $r = 0$. The size of the simulation area is set to $1000 * r_T$ in order to let the diffusion profiles fully establish. In order to mesh the simulation area correctly, it is divided in subdomains with different sizes of meshing (see Figure 34). The bulk domain is meshed with the coarser triangles while the zone around the probe and the catalyst deposit is refined with thinner triangles. A further refinement is built on the boundaries representing the catalyst deposit and the bottom wall of the probe. Finally, a last refinement is performed around the boundary between the active part and the inactive part of the probe. This area is indeed crucial for an accurate evaluation of the O_2 flux consumed by the probe. The mesh is considered as sufficient when increasing the number of triangles does not significantly change the results of the simulation.

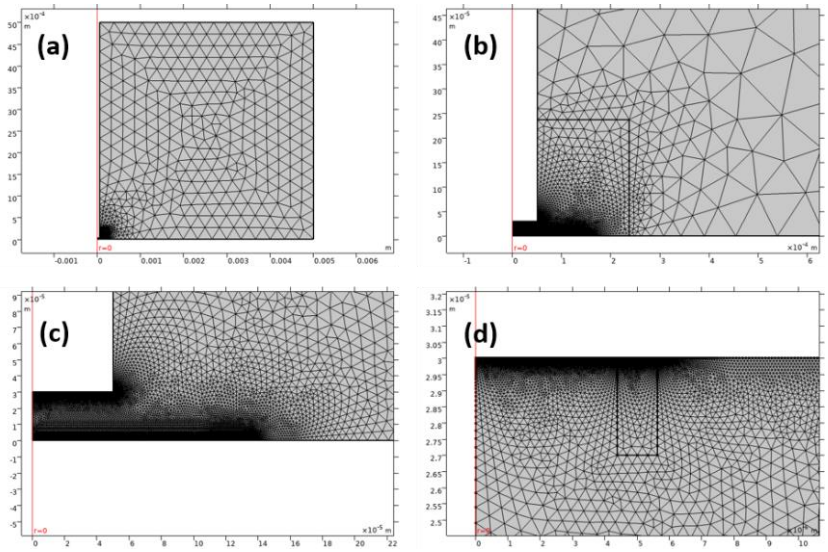

Figure 34: Meshing of the simulation area for r_T =5 µm, RG=10, L=3, r_C =113 µm. a) Coarse triangles in the bulk domain. b) Refinement around the probe and the catalyst deposit. c) Refinement on the boundaries representing the catalyst deposit and the bottom wall of the probe. d) Refinement on the boundary between the active part and the inactive part of the probe.

The model validation has been performed in negative feedback mode, by comparing simulated approach curves with the analytical expression established by Cornut et al. [69]:

$$NIT(L,RG) = \frac{\frac{2{,}08}{RG^{0{,}358}}\left(L - \frac{0{,}145}{RG}\right) + 1{,}585}{\frac{2{,}08}{RG^{0{,}358}}(L + 0{,}0023RG) + 1{,}57 + \frac{\ln(RG)}{L} + \frac{2}{\pi RG}\ln\left(1 + \frac{\pi RG}{2L}\right)} \quad (20)$$

with $L = \frac{d}{r_T}$ and $RG = \frac{r_{glass}}{r_T}$ the usual dimensionless parameters. This expression has an accuracy of 1 % for L>0.1 and RG<200. Figure 35 represents the approach curves calculated with the analytical expression and the Comsol model, as well as the difference between these two models for a case with r_T=5 µm, RG=10 and n_T=4. A value of r_C=113 µm is set, corresponding to a square deposit of 200 µm side, but a zero flux is defined at this boundary. The difference between the two models does not exceed 0.01, which validates the accuracy of the numerical model in negative feedback mode. No changes are added to the geometry in RC or SG-TC mode, so the model can be validated in these two modes too.

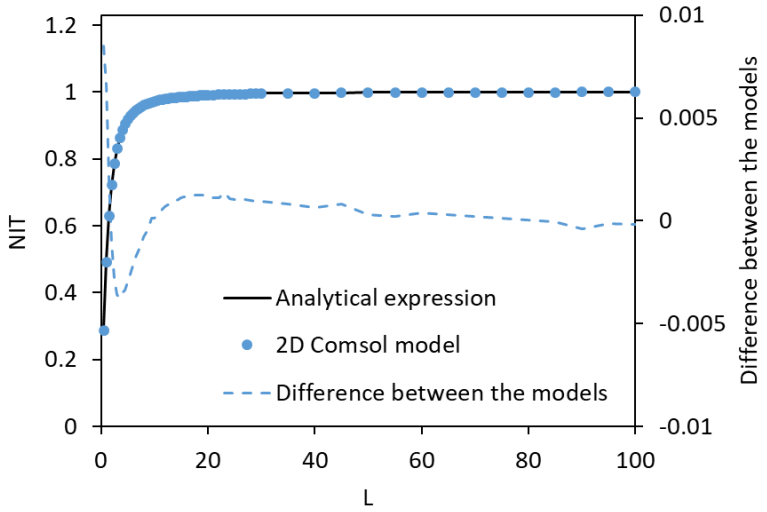

Figure 35: Left axis (points and solid line): negative feedback approach curves calculated with the Comsol model and with the analytical expression from [69]. Right axis (dashed line): difference between the two curves. r_T=5 µm, RG=10, r_C=113 µm and n_T=4.

III.2.3. Influence of the deposit geometry

In the 2D axisymmetric model the catalyst deposit is represented by a disk, while the experimental deposits are square shaped. Hence, working with a 2D axisymmetric model requires an approximation on the geometry of the deposit. The validity of this approximation has been investigated by building a 3D model, which allows to have square shaped deposits. This model and its meshing have been set up identically to the 2D model. Figure 36 shows the meshing of the 3D model with a square shaped deposit.

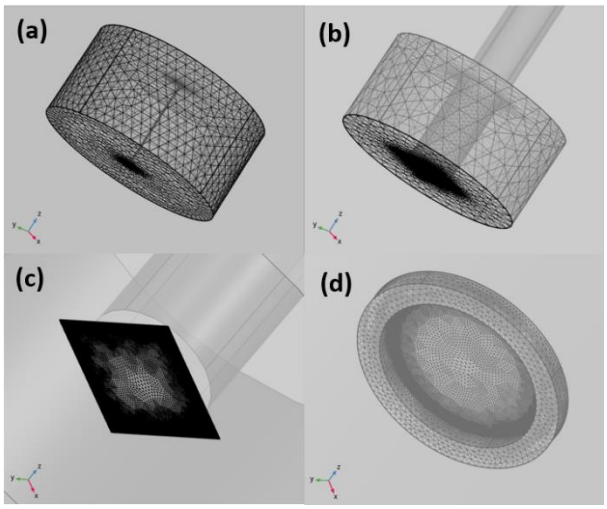

Figure 36 : Meshing of the simulation area for r_T =5 µm, RG=10, L=3, n_T=4, $S_{deposit}$ = 200 x 200 µm. a) Coarse triangles in the bulk domain. b) Refinement around the probe and the catalyst deposit. c) Refinement on the boundaries representing the catalyst deposit and the bottom wall of the probe. d) Refinement on the boundary between the active part and the inactive part of the probe.

Similarly to the previous part, the model accuracy is verified by comparing an approach curve in negative feedback mode simulated by the 3D model (with a disk shaped deposit) to the analytical expression (20). Figure 37 shows that the 3D model is less accurate than the 2D model. The difference between the two models reaches 0.065 for L=0.5, while it stabilizes around 0.02 at higher L values. This bigger error is probably due to a less refined mesh in the 3D simulation. Indeed, simulating the SECM set-up in 3D requires more nodes and refining the mesh demands more computing capacity. For instance, the 3D model requires about 40 min to simulate the presented approach curve, while it takes 15 min with the 2D model.

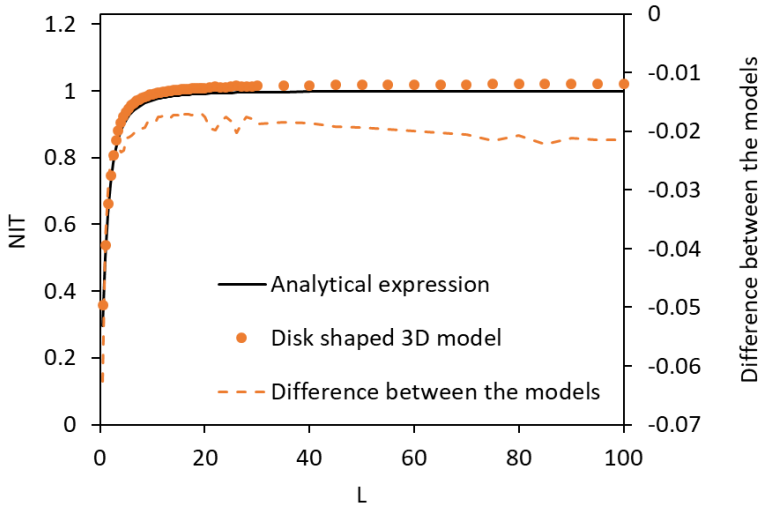

Figure 37: Left axis (points and solid line): negative feedback approach curves calculated with the 3D Comsol model with a disk shaped deposit. Right axis (dashed lines): error to the analytical expression of the two models. r_T=5 µm, RG=10, r_C=113 µm and n_T=4.

Then the 3D model is used to calculate approach curves in RC mode and in SG-TC mode with deposits with a same surface (40 000 µm²) but of different shapes (square shape or disk shape). At this stage of the study, simplified boundary conditions are set at the catalyst deposit. In RC mode, the active specie is O_2. It is consumed by both the probe and the catalyst, so $C_{O2} = 0$ is set at these two boundaries. The number of electrons exchanged at the probe and at the catalyst are fixed to 4 for the two boundaries. In SG-TC mode, the active specie is H_2O_2. It is not present initially in the solution so $C_0 = 0$. At the probe active part $C_{H2O2} = 0$, and at the catalyst deposit $C_{H2O2} = C_{O2}^{ref}$ with C_{O2}^{ref} the concentration of oxygen in the bulk solution. The number of electrons exchanged at the probe and at the catalyst are set to 2 for the two boundaries. Figure 38 shows the evolution of the probe and deposit currents during the approach curves in RC and SG-TC modes with two different deposit shapes. The current at the deposit of catalyst is slightly different (by 2.5 %) whether the deposit is disk shaped or square shaped. This may come from a different meshing of the two shapes, leading to a different evaluation of the current. The calculation of the current density at the corner of a square may be more delicate than the calculation at a disk border. On the other hand, the difference of the probe current for the two shapes is very low (around 0.5 % in RC mode and 2.5 % in SG-TC mode). We can thus conclude that approximating the shape of the deposit by a disk of radius $r_C = \sqrt{\frac{S_{deposit}}{\pi}}$ has a negligible influence on the calculated currents. We will thus use the 2D axisymmetric model for the rest of the study.

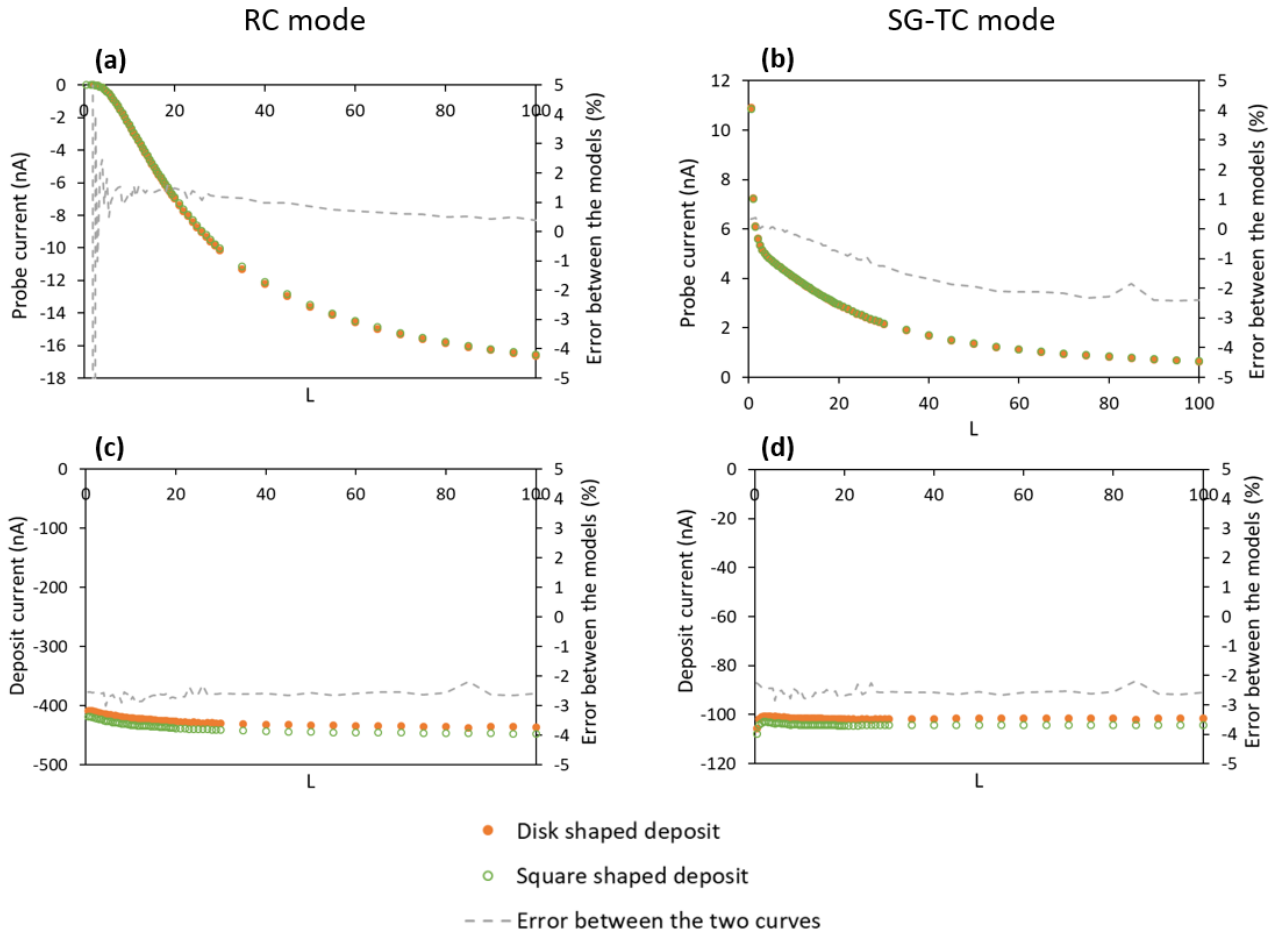

Figure 38: Comparison of the currents calculated at the probe (a and b) and at the catalyst deposit (c and d) in RC mode (a and c) and in SG-TC mode (b and d) for a disk shaped deposit and a square shaped deposit.

III.3. Estimation of kinetic parameters

In order to estimate the kinetic parameters of ORR on our catalyst, the flux of oxygen consumed by the deposit W_{O2} (mol/m²/s) is detailed as follows, using the Butler-Volmer equation:

$$W_{O2} = \frac{i_0}{n_C F}\frac{C_{O2}}{C_{O2}^{ref}}\left[\exp\left(\frac{\alpha n_C F}{RT}\eta\right) - \exp\left(\frac{-(1-\alpha)n_C F}{RT}\eta\right)\right]\frac{V_{catalyst}}{S_{deposit}} \quad (21)$$

with i_0 (A/m³) the exchange current density, n_C the number of electrons exchanged at the catalyst, C_{O2} (mol/m³) the concentration of O_2 at the catalyst boundary, C_{O2}^{ref} (mol/m³) the concentration of O_2 in the bulk of the

solution, $V_{catalyst}$ (m^3) the volume of material determined with AFM, and $S_{deposit}$ (m^2) the surface of the deposit measured with an optical microscope. The overpotential η (V) is defined as $E_{sub} - OCV_{sub}$, with E_{sub} the potential applied at the substrate and OCV_{sub} the substrate open circuit potential. The symmetry factor of the reaction α is fixed at 0.5. The two parameters that we want to determine from SECM experiments are i_0 and n_C. They will be extracted from RC and SG-TC measurements that were performed above the deposits while a LSV between 0.5 V/SCE and 0 V/SCE was applied to the substrate. First, the results of a SECM experiment are strongly dependent on the geometry of the set-up and particularly the probe dimensions. These dimensions will be determined precisely by fitting approach curves in negative feedback mode. Then, an approach combining the measurements in RC and SG-TC modes will be used to determine the value of n_C. Finally, the measurements in RC mode will be fitted by the model using Eq. (21) in order to extract the value of i_0.

III.3.1 Determination of the probes parameters

In order to use the SECM numerical model for the extraction of kinetic parameters of ORR catalysts, the probes parameters (r_T, RG and n_T) need to be determined with precision. Indeed, the values of r_T and RG can vary slightly because of the successive polishings of the microelectrode. Besides, the mechanism of the reaction at the probe can also vary a little because of fluctuations of the electrode surface state or the presence of impurities in the solution. Fitting approach curves with the analytical expression in negative feedback mode (Eq. (20)) is a precise method to determine r_T, RG and n_T. The method was presented in the part II.2.2 for the gold probe, and several approach curves were analyzed. For the platinum probe, 5 mM of H_2O_2 is added to the solution before performing the approach curves with the probe polarized at 0.9 V/SCE. Several approach curves have been recorded with the two electrodes used for the SECM experiments, enabling to get an average value of the probe parameters. Figure 39 shows an example of one approach curve for each electrode, with the associated analytical curve and the numerical values of the probe fitted parameters.

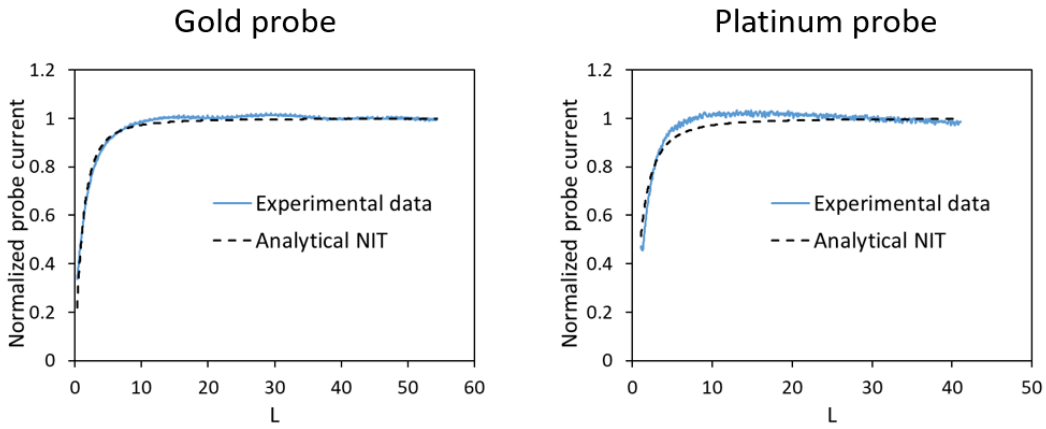

Electrode	r_T	RG	n_T
Gold	6.2 µm ± 0.6 µm	11 ± 2	2.7 ± 0.3
Platinum	3.5 µm ± 0.8 µm	10.4 ± 1.2	2.47 ± 0.4

Figure 39: Determination of the parameters of the gold and platinum probe used for the SECM measurements. The values of r_T, RG and n_T are fitted on approach curves in negative feedback mode. The table gives the values averaged on several measurements for each electrode.

III.3.2. Determination of n_C

The number of electrons exchanged at the catalyst n_C is calculated by combining the experiments done in RC mode (measurement of O_2 consumption) and in SG-TC mode (measurement of H_2O_2 production). Similarly to the works initiated by Sánchez-Sánchez [170], [171] and Schuhmann [172], [149], n_C is expressed through a derivation inspired by the RRDE methodology:

$$\frac{i_{sub\ O2}}{n_C} = \frac{i_{sub\ H2O}}{4} + \frac{i_{sub\ H2O2}}{2} \quad (22)$$

$$\frac{i_{sub\ O2}}{n_C} = \frac{i_{sub\ O2} - i_{sub\ H2O2}}{4} + \frac{i_{sub\ H2O2}}{2} \quad (23)$$

$$\frac{\Delta i_{tip\ O2}}{n_C\ \eta_{RC}} = \frac{\Delta i_{tip\ O2}}{4\ \eta_{RC}} + \frac{\Delta i_{tip\ H2O2}}{4\ \eta_{SG/TC}} \quad (24)$$

$$n_C = \frac{4\,\Delta i_{tip\ O2}}{\Delta i_{tip\ O2} + \frac{\eta_{RC}}{\eta_{SG/TC}}\Delta i_{tip\ H2O2}} \quad (25)$$

$i_{sub\ O2}$ is the substrate current linked to the total consumption of O_2 by the deposit of catalyst, $i_{sub\ H2O}$ and $i_{sub\ H2O2}$ are the substrate currents linked to the production of H_2O and H_2O_2 with respectively the 4 e^- pathway and the 2 e^- pathway. $\Delta i_{tip\ O2}$ is the variation of current at the SECM probe during a measurement in RC mode, and $\Delta i_{tip\ H2O2}$ is the variation of current at the SECM probe during a measurement in SG-TC mode. η_{RC} and $\eta_{SG/TC}$ are the collection efficiency factors of the considered SECM modes, defined by:

$$\eta_{RC} = \frac{\Delta i_{tip\ O2}}{i_{sub\ O2}} \quad \text{and} \quad \eta_{SG/TC} = \frac{\Delta i_{tip\ H2O2}}{i_{sub\ H2O2}} \qquad (26)$$

In the approach developed by Schuhmann, a collection efficiency ratio $N = \frac{\eta_{RC}}{\eta_{SG/TC}}$ is defined. This value is assumed to be 100 % as the the probe current does not change when the distance between the probe and the substrate is varied [172]. Here, since two distinct electrodes with slightly different dimensions are used for the measurements in RC and SG-TC mode, the collection efficiencies η_{RC} and $\eta_{SG/TC}$ will be calculated with the numerical model.

In order to calculate these collection efficiencies, the currents at the probe and at the substrate are simulated for a probe-substrate distance of 30 µm (which is the value used experimentally), with the probe dimensions determined previously (see on Figure 39) and with a substrate radius corresponding to a 200 µm side deposit. The simplified kinetics presented in part III.2.3. are reused here (substrate concentration equal to $C_{O2} = 0$ in RC mode and to $C_{H2O2} = C_{O2}^{ref}$ in SG-TC mode). In SG-TC mode, only the current of the 2 e^- reaction is needed to calculate $\eta_{SG/TC}$. The number of electrons exchanged at the catalyst n_C is thus set at 2 in this particular case. Then the currents at the probe and at the substrate are simulated and $\eta_{SG/TC} = 3.74\ \%$ is calculated. It is verified that changing the concentration condition at the catalyst deposit does not change the estimation of $\eta_{SG/TC}$. In RC mode, the total current at the catalyst including the 4 e^- pathway and the 2 e^- pathway is needed. So the value of n_C is needed to calculate η_{RC}. An iterative process is completed thanks to an experimental measurement (see Figure 40 (a)). Firstly, the values of η_{RC} with $n_C = 2$ and $n_C = 4$ are simulated. It is found that 3.73 % ≤ η_{RC} ≤ 7.47 %. Then Eq. (25) is used with these two threshold values and the experimental probe currents to calculate n_C: 3.36 ≤ n_C ≤ 3.65. These values are again implemented in the Comsol model to calculate a more precise range for η_{RC}. After two iterations, a value of $\eta_{RC} = 4.3\ \%$ is determined, leading to $n_C = 3.61$ for the experiment used. The collection efficiency ratio $N = \frac{\eta_{RC}}{\eta_{SG/TC}} = 1.15$ is close to the value of 100 % assumed in the other studies.

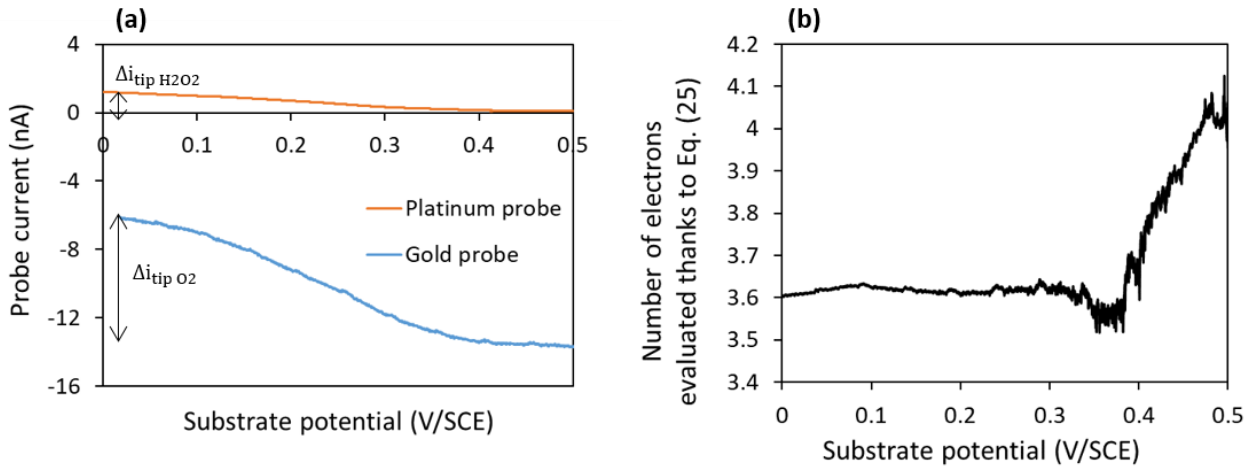

Figure 40: (a) Example of SECM measurements for the determination of the number of electrons exchanged at the probes (gold and platinum). Gold probe: rT≈6.2 µm, RG≈11, E_{probe}=-0.65 V/SCE. Platinum probe: rT≈3.5 µm, RG≈10.4, E_{probe}=0.9 V/SCE. Experiments done in a H_2SO_4 0.1 M solution saturated with oxygen and a distance probe-substrate of 30 µm. A LSV was applied at the substrate from 0.5 V/SCE to 0 V/SCE with v_{scan}=2 mV/s. (b) Evaluation of n_C for the experiment presented in (a) according to Eq. (25).

The calculation of n_C is performed for all the experiments considered in this chapter (deposits from inks prepared with different formulations). Figure 40 (b) shows on one example that the value of n_C remains independent from the potential applied to the substrate (above 0.4 V/SCE, the ORR activity is not significant). This is the case for all the deposits studied. Hence, the values of n_C calculated from the experiments in RC mode and in SG-TC mode are plotted on Figure 41 (a). All the series except one (sonication with 5 % of Nafion) are overlapping with no visible effect of the loading, the method of dispersion, or the amount of Nafion on the number of electrons exchanged at the catalyst. The curve corresponding to the ink prepared by sonication with 5 % of Nafion shows however a slightly smaller value for n_C. The distribution of particles sizes of this series of experiments is plotted on Figure 41 (b), and a slightly bigger proportion of smaller particles is noticed for the deposits made with the ink dispersed by sonication with 5 % of Nafion. Considering that the H_2O_2 produced by the ORR within an agglomerate can be further reduced to H_2O before it reaches the bulk solution (see Eq. (10)), having smaller particles on the deposits can lead to a bigger amount of H_2O_2 released in the solution. This hypothesis should be examined through more experiments but these results indicate that H_2O_2 decomposition occurs even within the agglomerates, and not only when the material is processed into a thick layer. Anyhow, the average value of n_C for the overlapping series is 3.88 ± 0.04, indicating that the CEA-BRF02 catalyst synthesized in the LICSEN has a very good selectivity towards the 4 e^- pathway of ORR.

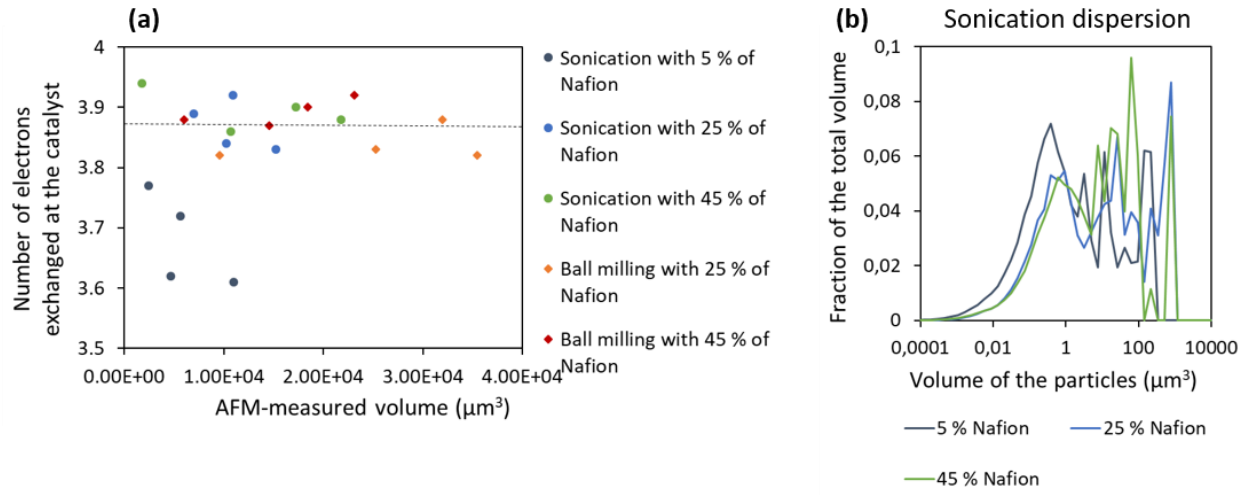

Figure 41: (a) Calculated values of n_C towards the volume of material for several proportions of Nafion and dispersion methods. (b) Distributions of particles sizes of the deposits prepared by sonication.

III.3.3. Determination of i_0 and introduction of a local ohmic drop

The exchange current density i_0 is determined by fitting experimental curves in RC mode with the numerical model. As it was mentioned in the introduction of this part (see Eq. (21)), a flux of O_2 consumption based on the Butler-Volmer equation is defined at the deposit boundary:

$$W_{O2} = \frac{i_0}{n_C F}\frac{C_{O2}}{C_{O2}^{ref}}\left[\exp\left(\frac{\alpha n_C F}{RT}\eta\right) - \exp\left(\frac{-(1-\alpha)n_C F}{RT}\eta\right)\right]\frac{V_{catalyst}}{S_{deposit}} \qquad (27)$$

At this stage of the study, the only unknown parameter is i_0. The other parameters of the simulation are either taken from the literature, measured during the experiments (SECM, AFM and optical microscope) or determined by the method presented in the previous paragraphs. These parameters, their values and their sources are exhaustively detailed in the Annex 2. The only parameter that remains unknown at this stage of the study is the exchange current density i_0. The model is thus used to fit this parameter by varying its value until the modeled curve becomes identical to the experimental curve.

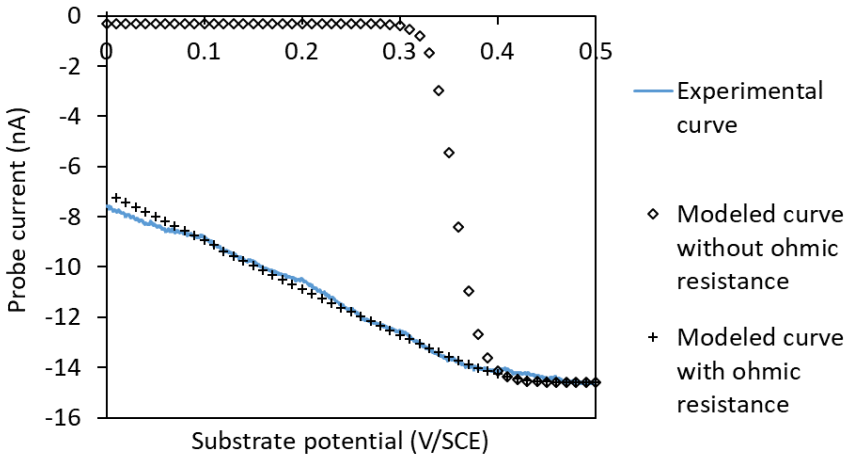

Figure 42: Comparison the model ability to fit an experimental curve with and without the addition of an ohmic resistance.

Nevertheless, it was not possible to fit the experimental curve with the flux defined by Eq. (27). Indeed, the slope of the polarization curve is much softer in the experimental data than for the modeled curve (see Figure 42). The shape of the curve indicates that an ohmic phenomenon can be considered in order to improve the fit between the experiment and the model. This phenomenon may represent the screening of the applied potential due to local ohmic drop. Local ohmic drop can occur from resistive paths inside the agglomerates or contact resistances between the agglomerates and the substrate. It is injected into in the model by modifying the Butler-Volmer expression:

$$W_{O2} = \frac{i_0}{n_C F}\frac{C_{O2}}{C_{O2}^{ref}}\left[\exp\left(\frac{\alpha n_C F}{RT}(\eta - R_\Omega i_C)\right) - \exp\left(\frac{-(1-\alpha) n_C F}{RT}(\eta - R_\Omega i_C)\right)\right]\frac{V_{catalyst}}{S_{deposit}} \quad (28)$$

with R_Ω ($\Omega.m^3$) the ohmic resistance and i_C (A/m^3) the current density at the catalyst deposit, expressed per volume of catalytic material. With this correction, the model is able to fit the experimental curves (see Figure 42). The ohmic term correcting the potential perceived by the catalyst particles is thus kept in the model and values of i_0 and R_Ω are fitted from experiments. R_Ω governs the slope of the curve while i_0 controls the onset potential of the ORR. Hence, no risk of overfitting is introduced by the addition of this supplementary parameter.

The values of R_Ω and i_0 have been evaluated thanks to a fitting procedure using the model described previously. The experiments comparing different methods of dispersion and different proportions of Nafion were considered (see part II.5. and III.1.). The values are plotted towards the volume of material measured with AFM on Figure 43. R_Ω is independent from the volume of material, the dispersion method or the amount of Nafion. A mean value considering all the deposits is calculated: R_Ω = 1.94 x 10^{-8} ± 0.82 x 10^{-8} $\Omega.m^3$.

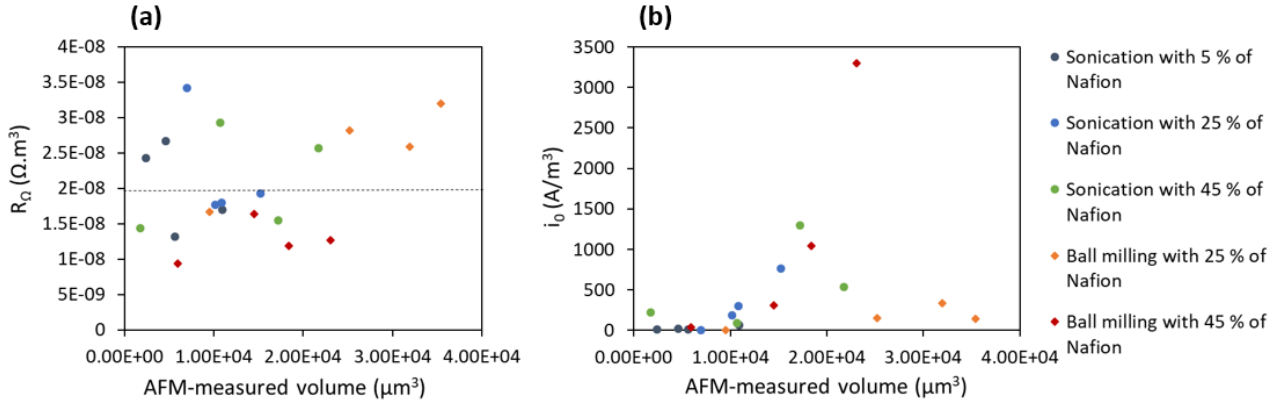

Figure 43: Fitted values of (a) R_Ω and (b) i_0 towards the volume of material for several proportions of Nafion and dispersion methods. The mean value for R_Ω is represented by the dashed line.

As concerns the determination of the exchange current density, the fitted values of i_0 look very dispersed and seem to vary with the loading. However, i_0 is supposed to reflect the intrinsic activity of the catalyst and should be independent of the loading, as soon as the material is sufficiently dispersed. The accuracy of our fits has thus been investigated by studying the sensitivity of the model to the parameter. The variations of i_0 affect essentially the onset potential, which is defined as the potential at which the probe current falls below 90 % of its initial value. Thus, the variations of i_0 required to modify the onset potential by ± 0.01 V are calculated for each data point (see an example on Figure 44 (a)) and these variations serve to define error bars to the values fitted by the model.

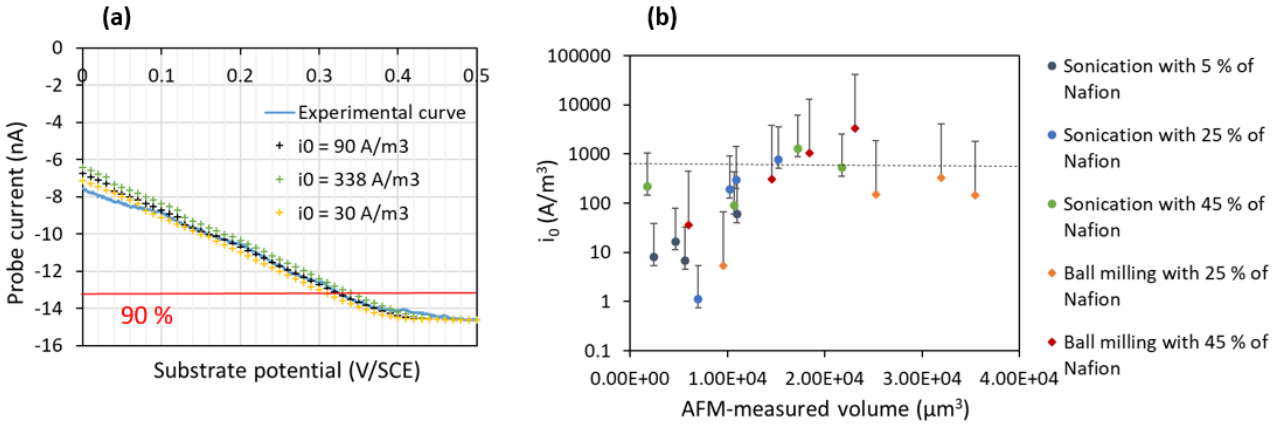

Figure 44: Sensitivity analysis on the parameter i_0. (a) Determination of the sensitivity for one experiment. (b) Fitted values of i_0 towards the volume of material with error bar corresponding to the parameter sensitivity (logarithmic scale).

The effect of i_0 on the onset potential is logarithmic. The higher is the value of i_0, the larger is the range in which the variation of i_0 does not affect the onset potential. This range has been determined for each data point. On average, the onset potential is modified by more than ± 0.01 V when i_0 is varied beyond 33 % or 376 % of the fitted value. These limit values have been plotted as error bars in Figure 44 (b), which is represented with a logarithmic scale. On this figure, taking into account the logarithmic scale and the error bars, the values of i_0 look less erratic. An average value independent of the loading seems to emerge: $i_0 = 670\ A/m^3$.

In the literature, similar exchange current densities have been estimated for PGM-free catalysts by fitting polarization curves in a single cell with a numerical model. Leonard et al. determined a value of 1300 A/m^3 for the Pajarito catalyst, while Baricci et al. [173] evaluated i_0 to 2000 A/m^3 for a similar Fe-N-C catalyst synthesized with the sacrificial support method. Komini Babu et al. [64] found a mean value of 160 A/m^3 for a CM-PANI-Fe catalyst investigated with several Nafion loadings. Thus, the value estimated in this work with the SECM-based method is in the order of magnitude of the exchange current densities estimated in the literature.

III.4. Conclusion

In this chapter, a new methodology for the determination of kinetic parameters of ORR catalysts has been presented. This methodology is based on a numerical model of the SECM set-up in order to investigate the exchange current density and the selectivity of ORR for the PGM-free catalyst synthesized in the LICSEN (CEA-BRF02). The model enables to simulate SECM experiments in negative feedback, redox competition and substrate generation-tip collection modes. Thereby, experiments measuring the consumption of O_2 (RC mode) and the production of H_2O_2 (SG-TC mode) by the catalyst have been investigated with the model. An ohmic resistance leading to important performance losses was brought to light. The two kinetic parameters determined with this methodology were an exchange current density of 670 A/m^3 and a number of electrons exchanged per O_2 molecule of 3.88. The estimation of the ohmic resistance added to the model gave an average value of 1.94 x 10^{-8} Ω.m^3. Investigating further this ohmic resistance could be very interesting for the development of efficient PGM-free catalysts. Indeed, the loss of performance caused by this resistance can be very important (see the difference between the two modeled curves on Figure 42) and should be perceptible in single cell measurements. This aspect will be notably investigated in the Chapter IV that concerns single cell

modeling. At agglomerate scale, the use of a conductive AFM during our measurement protocol could enable to access the conductivity of each particle and identify the type of particle responsible for the ohmic loss.

Chapter IV Investigation of PGM-free fuel cell performance through a single cell numerical model

Computational modeling plays a key role in the comprehension of PEMFC operation. The performance measured experimentally involves numerous and coupled phenomena, that modeling allows to investigate altogether. Several approaches are coexisting, with different levels of complexity in the modeling of the physics, and different required computational capacities. These approaches will be detailed in a first part, with a focus put on the models including PGM-free materials. Then, the relationship between the structure and the activity of PGM-free materials will be investigated at the single cell scale by performing numerical simulations of a membrane electrode assembly (MEA). The model developed in this chapter is based on a 1D macro-homogeneous model developed in the CEA-Grenoble for the study of Pt/C-based PEMFC. This model will be modified in order to integrate the kinetic parameters determined in the Chapter III on SECM and AFM measurements. An agglomerate model will also be included in the cathodic CL in order to describe more finely the crucial phenomena occurring in this layer. The model will be then compared with experimental results performed by a partner of the PEGASUS project. Finally, several CL and agglomerate parameters will be numerically investigated in order to identify the main contributions to the performance losses and propose some improvements of the CL formulation.

IV.1. Numerical modeling of membrane electrode assemblies

IV.1.1. Presentation of the different types of numerical models

PEMFC modeling at the MEA scale aims at understanding the phenomena occurring during the operation of a fuel cell and providing formulation recommendations in order to increase the performance. The transport and reaction of the species involved in the electrochemical reactions are modeled through the different layers composing the MEA. The catalyst layer (CL) is the more difficult element to simulate. Indeed, the transport of species in different phases and their reaction at the catalytic sites need to be resolved in this complex structure. Notably, the morphology of the CL and the repartition of its components (carbon material, ionomer, gas phase) will have a significant impact on the performance of the cell. Because of the complexity of the CL architecture, several modeling approaches are coexisting. They are classified on Figure 45:

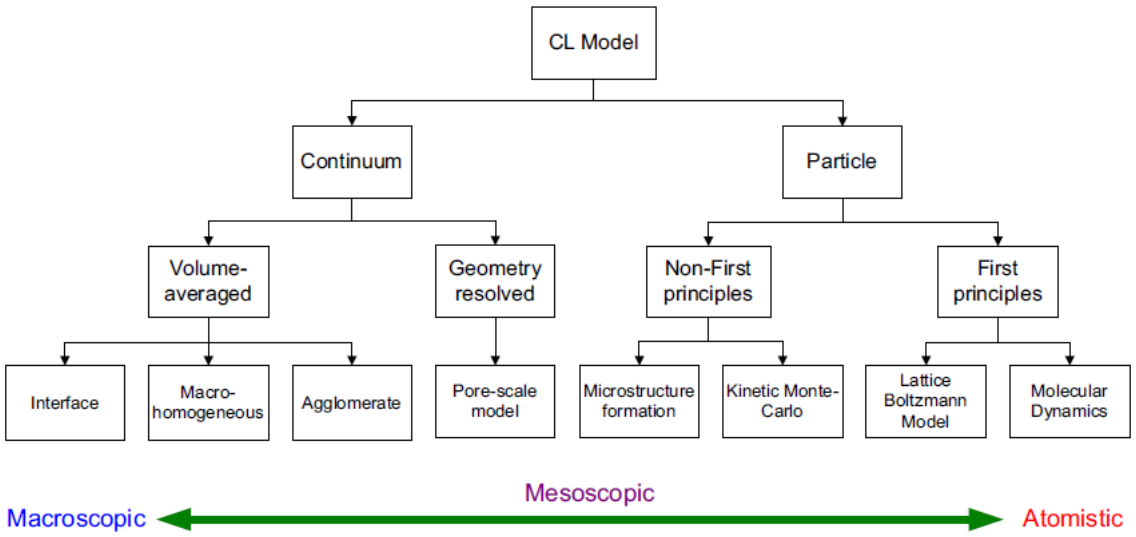

Figure 45: Classification of the different models for describing the CL structure. Figure taken from [174].

The continuum models consider the layers as a continuous media where conservation equations are resolved over an averaged representative element of volume. The particle-based models describe the phenomena happening to a single particle or a cluster of particles and use advanced numerical methods like Kinetic Monte-Carlo [175], [176] or Lattice Boltzmann [177], [178]. These particles-based models will not be

further reviewed here. Over the continuum models, several approaches are existing to describe the structure of the CL:

- The interface models [179], [180] treat the CL as an interface between the GDL and the membrane, considering that this layer is thin enough to neglect the transport in its structure. These models can only give an approximate performance of the MEA and are not adapted to study the architecture of the CL.

- The macro-homogeneous models [181], [182], [183], [184] consider the CL as a continuous medium where the different phases are uniformly distributed. These models enable to solve the transport of the species within the CL structure and give accurate predictions of the cell performance under specific conditions. However, these model cannot predict the significant mass transport limitations occurring at high current densities.

- The agglomerate models consider more explicitly the structure of the CL by describing the transport within clusters of carbon particles embedded in ionomer, the agglomerates. The characteristics of the agglomerates (shape, composition, size) can be varied in order to investigate with more precision the effect of the CL structure on the cell performance. The majority of the studies consider spherical agglomerates with an identical size, but some articles deal with cylindrical or slab agglomerates [185]. The carbon cluster is often considered as completely filled with ionomer, but some models assume that the porosity within the agglomerate is filled with liquid water [186]. A thin film of ionomer surrounding the agglomerate is often included in the models, as well as, in some cases, a film of liquid water. The size of the agglomerates is often assumed or determined on SEM images of CL and differs a lot according to the studies (from 20 nm to 5 µm). Some models are also taking into account different sizes of agglomerates within the CL [64]. Two ways for describing the agglomerate behavior are coexisting. A numerical model of the agglomerate can be integrated in a MEA model [187], [185], or an analytical expression of the agglomerate current can be used directly in the source term of the macro-homogeneous model [188], [189]. This analytical expression will be presented in the part IV.3.2. Agglomerate models have a great accuracy in the prediction of the MEA performance. They are principally used to study the CL structure, especially the agglomerates characteristics [190], [191], and the thickness [192] or composition [193] of the electrode. The operating conditions are also often investigated with such models [194], [191].

- The more complex models attempt to resolve the heterogeneous geometry of the CL with the help of imaging techniques (see part I.3.4.). First, the CL microstructure is computationally reconstructed from images with respect to the determined physical properties (porosity, pore size distribution, volume fractions). Then, the transport and reaction of the species are resolved in the structure with the appropriate

governing equations. Because of the limited resolution and FOV of the imaging techniques, these models are generally coupled with an agglomerate model and a macroscale model. These models are useful to study the water management in the CL [195] or the GDL [196], as well as the effect of the CL composition and morphology on the performance [197], [198], [199].

MEA modeling can be performed in 1D, 2D or 3D, depending on the issue investigated. 1D models are simple to set-up and rapid to compute. They describe the physical phenomena occurring across the MEA without considering the inhomogeneities in the plan of the layers [200], [201]. 2D models consider a cross section of the MEA, often containing under-rib and under-channel areas. They aim notably at modeling the impact of the bipolar plate (BP) geometry on the performance [202], [203]. Other 2D models can be built along a channel in order to study the effect of reactants depletion and water accumulation in the channel [204]. Thanks to the progresses made on computing efficiency, 3D models are now accessible with reasonable power and time. They can question specific issues such as the shape of the BP [205], channel blockages [206], the effect of gas purging [207] or temperature and humidity issues [208].

IV.1.2. PGM-free PEMFC modeling in the literature

For years, PGM-free catalysts showed a too weak activity towards ORR to be considered as a reasonable alternative to Pt-based materials. It is only in 2011 that Proietti et al. conceived the first catalyst that reached competitive performance compared to Pt/C catalysts [25]. Since then, the materials developed are more and more active and their integration in PEMFC is now thoroughly considered. Modeling works are thus emerging in order to provide insights into the main phenomena affecting the performance of PGM-free PEMFC. These works are still few in numbers and are reviewed exhaustively in this part.

In 2014, Komini Babu et al. [63] combined an analytical agglomerate model with nano-scale resolution X-ray computed tomography (nano CT) extraction of the morphology and transport parameters. They investigated the limiting transport processes and especially the losses caused by the water flooding. Similar works were released by the same team in 2016 [61] and 2017 [64], both investigating different Nafion loadings leading to different ionomer distributions in the CL and thus different performances. The need to increase the hydrophobicity and the ionomer conductivity of the cathodic CL was highlighted in the second article. In 2015, Leonard et al. [209] used a 1D macro-homogeneous model to compare the performances in oxygen and air conditions of MEA prepared with the catalyst from Pajarito Powders. They studied notably the effect of water flooding and the optimization of the catalyst utilization. Pavlicek et al. [210] resolved in 2018 the gas-phase

and non-gas-phase resistances of two different PGM-free catalysts: the Pajarito catalyst and a MOF-based catalyst. They combined experiments involving different carrier gases with a pseudo 2D model. The same year, Xing [211] built a water-filled agglomerate model to study the effects of the CL and agglomerate composition in an MEA prepared with a nitrogen-doped carbon xerogel. He investigated the thickness, the porosity and the ionomer to carbon ratio of the CL. The internal structure of the agglomerate was also investigated, notably the ratio between the liquid water and the ionomer filling the primary pores of the agglomerate. It was found that liquid water offers a lower transport resistance compared to ionomer and leads to better performance. Overall, an ideal formulation of 6 $mg.cm^{-2}$ of catalyst with a 40 % porosity was highlighted. In 2019, Baricci et al. [173] developed a 1D macro-homogeneous model to interpret polarization curves and electrochemical impedance spectroscopy (EIS) measurements. They studied the effect of catalyst loading and ionomer content on the performance and the durability of PGM-free fuel cells. Liu et al. [65] compared in 2019 the impact of different electrode fabrication methods on the water management, by combining operando X-ray CT characterizations with an analytical agglomerate model. In 2020, they proposed an innovative algorithm coupling a microscale model and a nanoscale model for resolving multiscale transport processes incorporating the variations of effective properties [212]. According to them, the model accuracy was improved compared to the traditional macro-homogeneous models.

IV.2. Presentation of the EuROPIUM model

The model used in this work has been developed at CEA-Grenoble and is called EuROPIUM (ElectRochemistry OPtImization Understanding Modeling). It is a multi-scale modeling framework developed for solving numerous PEMFC processes at the cell level. The model includes:

- Gas transport in the porous media (GDL, CL)
- Dissolved water transport (diffusion and electro-osmosis) in the ionomer (CL, membrane)
- Electronic (BP, GDL, CL) and proton conductivity (CL, membrane)
- Heat transfer by conduction (GDL, CL, membrane)
- Electrochemical kinetics (CL)

The model is solved with Comsol Multiphysics® but Matlab® is also used as a piloting tool for helping the building of the model and running the simulations. Three versions have been developed by the CEA Grenoble: a 1D model, a 2D model and a 3D model. The 1D model will be the one used for this work. This is a degenerated version of the standard 2D rib-channel code where the equations are discretized along the through cell direction. The full description of the 2D model can be found in Randrianarizafy et al. work [181]. The model will be resolved in stationary conditions.

Figure 46 shows the geometry of the 1D model. It is composed of several domains representing the different layers in a MEA (see part I.2.1). Each domain can be composed of several phases (solid phase, gaseous phase or electrolyte phase) in which the transport of the different chemical species (O_2, H_2, N_2, H_2O, H^+, e^-) is resolved.

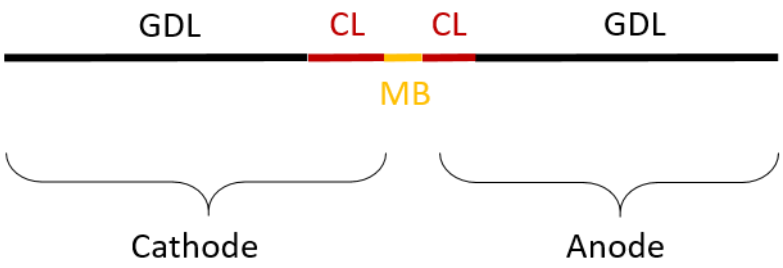

Figure 46: Geometry of the 1D EuROPIUM model. The GDL dimensions are not to scale.

IV.2.1. Transport in the gas phase

The gases are brought in the cell by the channels and penetrate first the porous media (GDL and CL). In the 1D model, no differentiation is done between the channel and the rib, thus the gas transport within the bipolar plates (BP) is not modeled. A concentration condition c_i (mol/m^3) is applied at the boundary between the BP and the GDL:

$$c_i = X_i \frac{P_{channel}}{RT} \qquad (29)$$

with $P_{channel}$ (Pa) the inlet pressure and X_i the molar fraction of specie i (O_2, H_2, N_2 or H_2O).

The mass balance in the gas phase is written as follows:

$$\nabla\left(\overrightarrow{N_i}\right) = S_i^a \quad (30)$$

with $\overrightarrow{N_i}$ (mol/m²/s) the molar flux of the specie and S_i^a (mol/m³/s) a source term. The source term depicts the dissolution of the active species (O_2, H_2 and H_2O) in the ionomer phase.

The molar fluxes are resolved with the Young and Todd approach [213] which includes convection and diffusion. The diffusion component is given by:

$$\frac{c_g \varepsilon}{\tau^2} \nabla\left(\overrightarrow{X_i}\right) = \sum_j \left[\frac{X_i \cdot \overrightarrow{N_j}}{(D_A)_{ji}} - \frac{X_j \cdot \overrightarrow{N_i}}{(D_A)_{ij}}\right] \quad (31)$$

with c_g (mol/m³) the total concentration of gases, ε the porosity of the layer and τ its tortuosity. A mean diffusion coefficient $(D_A)_{ij}$ (m²/s) taking into account the diffusion in gas phase and the Knudsen diffusion is defined:

$$\frac{1}{(D_A)_{ij}} = \frac{1}{D_{ij}} + \frac{1}{D_i^k} \quad (32)$$

The Knudsen diffusion coefficient being:

$$D_i^k = \left(\frac{2}{3} \cdot R_p \cdot \sqrt{\left(\frac{8RT}{\pi M_i}\right)}\right) \quad (33)$$

with R_p (m) the radius of the pores and M_i (kg/mol) the molar mass of the specie.

The convection component of the Young and Todd approach is given by:

$$\frac{\varepsilon}{\tau^2} \nabla\left(\overrightarrow{P_g}\right) = -A_A \sum_i \sqrt{M_i} \cdot \overrightarrow{N_i} \quad (34)$$

where P_g (Pa) is the total pressure of gases. The convection coefficient A_A takes into account the convection in gas phase and the convection due to Knudsen diffusion:

$$\frac{1}{A_A} = \frac{1}{A_C} + \frac{1}{A_K} \quad (35)$$

$$A_C = \frac{\mu}{c_g \tau^2 k \sum_i X_i \sqrt{M_i}} \quad (36)$$

with μ (Pa.s) the dynamic viscosity of the gases and k (m²) the permeability of the porous media.

$$A_K = \frac{3}{4R_p}\sqrt{\left(\frac{\pi RT}{2}\right)} \quad (37)$$

IV.2.2. Transport in the electrolyte phase

The EuROPIUM model takes into account the dissolution of O_2 and H_2 from the gas phase into a thin layer of ionomer surrounding the carbon surface of the catalyst layer (CL). Then the species reach the carbon surface and react on the catalytic sites (Pt in the original model). The mass balance in the electrolyte phase is expressed as follows:

$$\nabla\left(\overrightarrow{N_i^a}\right) = S_i^a + S_i \quad (38)$$

with $\overrightarrow{N_i^a}$ (mol/m^2/s) the diffusion flux in the ionomer along the cell direction, S_i^a (mol/m^3/s) the source term corresponding to the dissolution of the species in the ionomer, and S_i (mol/m^3/s) the source term corresponding to their consumption by the electrochemical reactions. This mass balance can be illustrated by the following scheme:

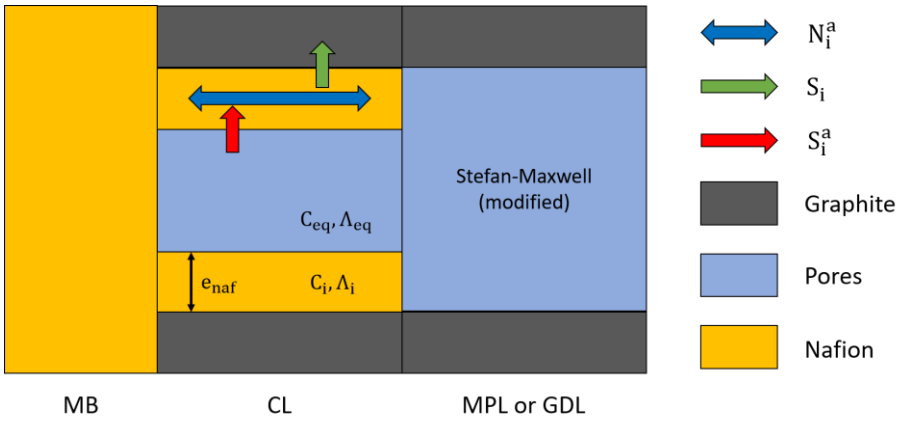

Figure 47: Illustration of the mass balance in the electrolyte phase of the CL. Figure taken from [181].

The diffusion flux along the through cell direction is written:

$$\overrightarrow{N_i^a} = -D_i^a \nabla\left(\overrightarrow{C_i}\right) \quad (39)$$

with D_i^a the diffusion coefficient of the gas in the ionomer phase. The dissolution of the species from the gas phase to the ionomer phase is expressed by the source term S_i^a :

$$S_i^a = \frac{D_i^a a_v}{e_{ionomer}}(C_i^{eq} - C_i) \quad (40)$$

with a_v (m^2/m^3) the specific surface and $e_{ionomer} = \frac{(1-\varepsilon)\varepsilon_{ionomer}}{a_v}$ the thickness of the ionomer layer surrounding the carbon surface ($\varepsilon_{ionomer}$ being the fraction of Nafion in the solid phase). C_i^{eq} (mol/m^3) is the concentration at the interface between the gas phase and the electrolyte phase: $C_i^{eq} = P_i \cdot H_i$, where H_i ($mol/Pa/m^3$) is the Henry constant for the specie and P_i (Pa) its partial pressure.

S_i in Eq. (38) represents the source term corresponding to the consumption of the species through the electrochemical reactions: $S_{H2} = -\frac{i_r}{2F}$ for the anode CL and $S_{O2} = \frac{i_r}{4F}$ for the cathode CL, i_r (A/m^3) being the current density of the reaction.

As concerns H_2O, it is considered at equilibrium in the CL electrolyte phase:

$$C_{H2O} = \Lambda \cdot C_{SO3-} \quad (41)$$

with C_{SO3-} (mol/m^3) the concentration of sulphonated sites in the Nafion and Λ the water content in this phase. Λ is calculated from the RH (relative humidity) in the gas phase with an interpolated table of values. Thus, in this case, the additional mass balance introduced for H_2 and O_2 does not apply and the source term in Eq. (30) depicts directly the production of H_2O by the electrochemical reactions: $S_{H2O} = 0$ for the anode CL and $S_{H2O} = -\frac{i_r}{2F}$ for the cathode CL.

In the membrane, the transportation of H_2O takes into account an electro-osmotic flux and a diffusion flux:

$$\nabla\left(\overrightarrow{N_{H2O}^a}\right) = 0 \quad (42)$$

$$\overrightarrow{N_{H2O}^a} = n_d \frac{\vec{i_l}}{F} - D_{H2O}\vec{\nabla}(C_{H2O}) \quad (43)$$

with n_d the electro-osmotic drag coefficient and i_i (A/m^2) the ionic current.

IV.2.3. Ionic and electronic transport

The transport of protons is computed in the membrane and in the CL. The ionic potential Φ (V) is calculated as follows:

$$\nabla\left(-\kappa_i \vec{\nabla}\Phi\right) = S \quad (44)$$

with κ_i (S/m) the ionic conductivity of the layer (membrane or CL) and S the source term corresponding to the production/consumption of protons by the electrochemical reaction: $S = 0$ in the membrane and $S = i_r$ in the CL. The ionic conductivity of the Nafion in the membrane is calculated with a formula taking into account the water content and the temperature [214]:

$$\kappa_{MB} = (0.5139 \cdot \Lambda - 0.326) \cdot exp\left(\frac{1}{303.15} - \frac{1}{T}\right) \quad (45)$$

The ionic conductivity in the CL is derived from this expression, taking into account the amount of ionomer in the layer:

$$\kappa_{CL} = \frac{(1-\varepsilon)\varepsilon_{ionomer}}{\tau^2} \cdot \kappa_{MB} \quad (46)$$

The ionic current is defined as:

$$\vec{\imath_i} = -\kappa_i \vec{\nabla}\Phi \quad (47)$$

The electronic transport is computed in the BP, the GDL and the CL with the following equation:

$$\nabla\left(-\sigma \vec{\nabla}\Psi\right) = S \quad (48)$$

with Ψ (V) the electronic potential and σ (S/m) the electronic conductivity. The source term corresponding to the electrochemical reaction is calculated: $S = 0$ in the BP and GDL and $S = -i_r$ in the CL. The electronic current is expressed:

$$\vec{\imath_e} = -\sigma \vec{\nabla}\Psi \quad (49)$$

A contact resistance between the BP and the GDL is included in the model by modifying the electronic conductivity in the part of the GDL in contact with the BP and over a length of $\frac{e_{GDL}}{100}$. This modified conductivity is noted $\sigma_{BP/GDL}$.

IV.2.4. Heat transfer

The heat transfer by thermal conduction is computed in the GDL, the CL and the membrane. At the boundary between the BP and the GDL, a temperature condition is fixed: $T = T_0$. The Fourier law is written:

$$\nabla\left(-\lambda\vec{\nabla}T\right) = \sum Q \quad (50)$$

with λ (W/m/K) the thermal conductivity and Q (W/m^3) the source terms. These source terms depends on the domain. In the domains where a current (electronic or ionic) is circulating, a Joule heat source term is defined:

$$Q_J = \frac{{i_i}^2}{\kappa_i} \quad \text{in the membrane and CL} \quad (51)$$

$$Q_J = \frac{{i_e}^2}{\sigma} \quad \text{in the GDL and CL} \quad (52)$$

In the CL, another source term depicts the heat produced by the electrochemical reaction:

$$Q_{reac} = \left((\Psi - \Phi) + \frac{\Delta H^0_{a/c}}{nF}\right) \cdot i_r \quad (53)$$

with $\Delta H^0_{a/c}$ (J/mol) the enthalpy of the reaction (hydrogen oxidation at the anode and oxygen reduction at the cathode).

IV.2.5. Electrochemistry

The current density of the reactions happening at the two electrodes i_r (A/m^3) is calculated with the Butler-Volmer expression:

$$i_r = j_0 a_v \left[\exp\left(\frac{\alpha n F}{RT}\eta\right) - \exp\left(\frac{-(1-\alpha)nF}{RT}\eta\right)\right] \quad (54)$$

with j_0 (A/m^2) the exchange current density, n the number of electrons exchanged, α the symmetry factor of the reaction and η (V) the overpotential, defined as $\eta = (\Psi - \Phi) - E$. The standard potential E (V) is calculated according to the Nernst law:

$$E = \frac{\Delta G°}{nF} + \frac{RT}{nF} \cdot log\left(\prod_{\nu_j} {a_i}^{\nu_i}\right) \quad (55)$$

with $\Delta G° = \Delta H° - T\Delta S°$. The values of $\Delta H°$ (J/mol) and $\Delta S°$ (J/mol/K) are taken from [215]. The activities of the species a_i are calculated as follows:

$$a_i = \frac{C_i}{P_{ref} H_i} \quad \text{for } H_2 \text{ and } O_2 \qquad (56)$$

$$a_{H2O} = \frac{P_{vap}}{P_{sat}(T)} \quad \text{for } H_2O \qquad (57)$$

$$a_{H+} = \frac{\Lambda^{eq}(1)}{\Lambda} \quad \text{for } H^+ \qquad (58)$$

In the EuROPIUM model, the exchange current density j_0 is expressed in function of the reaction rate and the species activities:

$$j_0 = n \cdot F \cdot (k_{ox}^0)^{1-\alpha} \cdot (k_{red}^0)^{\alpha} \cdot \left(\prod_{\nu_i > 0} ({a_i}^{\nu_i}) \right)^{1-\alpha} \cdot \left(\prod_{\nu_i < 0} ({a_i}^{-\nu_i}) \right)^{\alpha} \qquad (59)$$

The reaction rate coefficients k_{ox}^0 (mol/m²/s) and k_{red}^0 (mol/m²/s) are calculated with the activation enthalpies and the activation entropies:

$$k_{ox}^0 = k° exp\left(\frac{\Delta H_{ox}^{\ddagger} - T\Delta S_{ox}^{\ddagger}}{RT} \right) \qquad (60)$$

$$k_{red}^0 = k° exp\left(\frac{\Delta H_{ox}^{\ddagger} - T\Delta S_{ox}^{\ddagger} + \Delta G°}{RT} \right) \qquad (61)$$

with $k° = \frac{k_b T}{s_0 N_A h}$ (mol/m²/s). k_b(J/K) is the Boltzmann constant, N_A (mol^{-1}) the Avogadro number, h (J.s) the Planck constant and s_0(m²) the size of the catalytic site.

IV.3. Modifications brought to the EuROPIUM model

Herein we will present the modifications done on the cathodic catalyst layer (CL) modeling in order to introduce an agglomerate model and include the kinetic parameters determined with SECM. The model described in the previous part remains unchanged at the anodic side because this electrode is not limiting the overall performance. At the cathodic side, an analytical agglomerate model is introduced. The cathodic CL is modeled as a porous medium comprising gaseous pores and solid agglomerates. The agglomerates are spherical clusters of carbon particles embedded in the ionomer. They are characterized by their radius r_{agg} (m) and their composition $L_{i,agg}$ (the volume fraction of ionomer phase in the agglomerate core). They can be surrounded by a thin ionomer layer with a thickness δ_{agg} (m). The agglomerate current $i_{agg,CL}$ (A/m^3) will enable

to calculate the consumption/production of O_2 and H_2O by the CL. Thus the mass balance in the gaseous phase of the cathodic CL (see Eq.(30)) can be directly expressed as follows:

$$\nabla\left(\overrightarrow{N_i}\right) = S_i^{agg} \qquad (62)$$

with $S_{O2}^{agg} = \frac{i_{agg,CL}}{4F}$ and $S_{H2O}^{agg} = -\frac{i_{agg,CL}}{2F}$

The modeling of the cathodic CL can thus be illustrated by a new scheme:

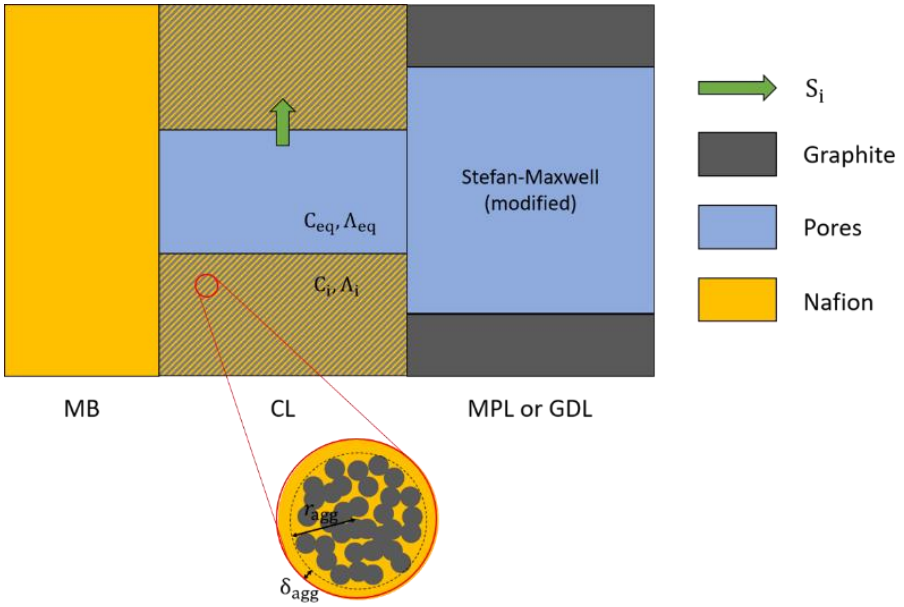

Figure 48: Modeling in the cathodic CL including the agglomerate model.

Moreover, the parameters i_0, n_C and R_Ω determined on the SECM measurements (see chapter III) will be included in the single cell model. Usually, kinetic parameters are fitted on MEA polarization curves, together with other quantities. For example, the EuROPIUM model fits four different parameters ($\Delta H_{ox}^{\ddagger}$, α_a, α_c, κ_{MB}), the first three of them being kinetic parameters. When too many parameters are fitted, this leads to a risk of overfitting and decreases the accuracy of the parameters estimation [216], [217], [218]. Thus, being able to determine experimentally the kinetic parameters on the simplified environment studied by SECM (with a direct access to the agglomerates) limits the risk of overfitting.

IV.3.1. Determination of CL composition and agglomerate parameters

The catalyst layers (CL) are prepared by mixing the solid phase and the ionomer phase before coating the mixture on the membrane. The loading in catalyst, the thickness of the electrode obtained and the mass ratios of the different materials enable to calculate the volume fractions of the different phases. At the cathode, the catalytic sites are comprised in the carbon material, leading to:

$$L_{S,c} = \frac{m_S}{\rho_S \cdot e_{CL,c}} \quad \text{and} \quad L_{i,c} = \frac{m_S \cdot I/C_c}{\rho_{Nafion} \cdot e_{CL,c}} \qquad (63)$$

with $L_{S,c}$ the volume fraction of solid phase, m_S (kg/m^2) the loading in carbon material, ρ_S (kg/m^3)the density of the solid phase and $e_{CL,c}$ (m) the thickness of the cathodic CL. $L_{i,c}$ is the volume fraction in ionomer phase, $I/C_c$the mass ratio of ionomer phase to carbon phase and ρ_{Nafion} (kg/m^3) the density of the Nafion. At the anode, the solid phase is composed of platinum and carbon with a mass ratio noted f. Thus, $L_{S,a}$ and $L_{i,a}$ are calculated as follows:

$$L_{S,a} = \frac{1}{e_{CL,a}}\left(\frac{m_{Pt}}{\rho_{Pt}} + \frac{m_{Pt}}{f \cdot \rho_C}\right) \quad \text{and} \quad L_{i,a} = \frac{m_{Pt} \cdot I/C_a}{f \cdot \rho_{Nafion} \cdot e_{CL,a}} \qquad (64)$$

with m_{Pt} (kg/m^2) the loading in platinum, ρ_{Pt} (kg/m^3) the density of platinum and ρ_C (kg/m^3) the density of carbon.

Knowing L_S and L_i, the porosity of the cathodic and anodic CL can be expressed as follows:

$$\varepsilon = 1 - L_S - L_i \qquad (65)$$

The composition of the agglomerates is deduced from the composition of the cathodic CL. First, the volume fraction of Nafion in the solid phase $\varepsilon_{ionomer}$ is calculated from the value of I/C_c:

$$I/C_c = \frac{\rho_{Nafion} \cdot \varepsilon_{ionomer}}{\rho_S \cdot (1 - \varepsilon_{ionomer})} \qquad (66)$$

Then, the volume fraction of Nafion in the agglomerate core is defined as follows:

$$\mathrm{L_{i,agg}} = \min\left(\varepsilon_{\mathrm{ionomer}}, \mathrm{L_{i,agg}^{max}}\right) \qquad (67)$$

$L_{i,agg}^{max} = 0.5$ being the maximal fraction of ionomer in the core of the agglomerate. If $\varepsilon_{ionomer} > L_{i,agg}^{max}$, a layer of ionomer with a thickness δ_{agg} is introduced around the agglomerate. By expressing L_S and L_i in function of the agglomerate parameters, δ_{agg} can be calculated :

$$L_s = n_{agg}\frac{4}{3}\pi {r_{agg}}^3(1 - L_{i,agg}) \quad (68)$$

$$L_i = n_{agg}\frac{4}{3}\pi\left[{r_{agg}}^3 L_{i,agg} + (r_{agg} + \delta_{agg})^3 - {r_{agg}}^3\right] \quad (69)$$

with n_{agg} (m^{-3}) the number of agglomerates per unit of CL volume. The radius of the agglomerate r_{agg} is estimated from SEM imaging of the CL.

The radius of the CL pores R_p (used to calculate the Knudsen diffusion coefficient) is now determined from the agglomerates parameters. The external surface area of the pores being equal to the external surface area of the agglomerates:

$$4\pi(r_{agg} + \delta_{agg})^2 \cdot \frac{(1 - \varepsilon)V_{CL}}{\frac{4}{3}\pi\left(r_{agg} + \delta_{agg}\right)^3} = 4\pi {R_p}^2 \cdot \frac{\varepsilon V_{CL}}{\frac{4}{3}\pi {R_p}^3} \quad (70)$$

$$R_p = \frac{\varepsilon}{(1 - \varepsilon)} \cdot (r_{agg} + \delta_{agg}) \quad (71)$$

IV.3.2. Derivation of the agglomerate current

Diffusion and chemical reaction within a porous material have been extensively studied in the field of heterogeneous catalysis [219], notably through the definition of adimensional factors. The effectiveness factor E_r represents the ratio between the real consumption rate by the agglomerate R_{O2} ($mol/m^3/s$) and the consumption rate if the entire catalytically active surface was exposed to the concentration measured at the agglomerate core surface $R_{O2,(core|film)}$ ($mol/m^3/s$).

$$E_r = \frac{R_{O2}}{R_{O2,(core|film)}} = \frac{1}{\Phi}\left(\frac{1}{\tanh(3\Phi)} - \frac{1}{3\Phi}\right) \quad (72)$$

Φ being the Thiele's modulus which characterizes the relative contributions of chemical reaction and diffusion for a given geometry. For spherical agglomerates with radius r_{agg}:

$$\Phi = \frac{r_{agg}}{3}\sqrt{\frac{k_c}{D_{O2}^{eff}}} \quad (73)$$

with k_c (s^{-1}) the reaction rate and $D_{O2}^{eff} = D_{O2,N} \times {L_{i,agg}}^{3/2}$ (m^2/s) the effective oxygen diffusion coefficient in the agglomerate. $D_{O2,N}$ (m^2/s) is the diffusion coefficient of oxygen in Nafion.

By assuming a first order reaction, the consumption rate by the agglomerate is defined as follows:

$$R_{O2} = E_r k_c C_{O2,(core|film)} \quad (74)$$

The flux of oxygen in the thin film of ionomer surrounding the agglomerate is:

$$N_{O2} = D_{O2,N}\frac{dC_{O2}}{dr} = \frac{F_{O2}}{4\pi r^2} \quad (75)$$

with F_{O2} (mol/s) the total oxygen consumption within the agglomerate. Integrating this expression and rearranging:

$$C_{O2,(core|film)} = C_{O2,(film|gas)} - \frac{\delta_{agg}}{r_{agg}\left(r_{agg}+\delta_{agg}\right)} \cdot \frac{F_{O2}}{4\pi D_{O2,N}} \quad (76)$$

F_{O2} can also be expressed as follows:

$$F_{O2} = \frac{4\pi {r_{agg}}^3}{3} R_{O2} = \frac{4\pi {r_{agg}}^3}{3} E_r k_c C_{O2,(core|film)} \quad (77)$$

Substituting Eq. (77) in Eq. (76):

$$C_{O2,(core|film)} = C_{O2,(film|gas)}\left[\frac{\delta_{agg}{r_{agg}}^2}{3\left(r_{agg}+\delta_{agg}\right)} \cdot \frac{E_r k_c}{D_{O2,N}} + 1\right]^{-1} \quad (78)$$

In order to express the volumetric current density i_{agg} (A/m^3) produced over the full agglomerate (core and ionomer shell), a scaling factor $\overline{V_{agg}}$ is applied to the consumption rate R_{O2}:

$$\overline{V_{agg}} = \frac{\frac{4\pi {r_{agg}}^3}{3}}{\frac{4\pi\left(r_{agg}+\delta_{agg}\right)^3}{3}} = \frac{{r_{agg}}^3}{\left(r_{agg}+\delta_{agg}\right)^3} \quad (79)$$

Thus, $i_{agg} = 4F\overline{V_{agg}}E_r k_c C_{O2,(core|film)}$ (80)

Substituting the oxygen concentration by Eq. (78) and rearranging:

$$i_{agg} = 4F\overline{V_{agg}}C_{O2,(film|gas)}\left[\frac{1}{E_r k_c} + \frac{\delta_{agg} r_{agg}^2}{3\left(r_{agg}+\delta_{agg}\right)D_{O2,N}}\right]^{-1} \quad (81)$$

$C_{O2,(film|gas)} = P_{O2}\cdot H_{O2}$ being the concentration of O_2 at equilibrium between the gas phase and the electrolyte phase. This expression describes the current density per volume of agglomerate. For the whole catalyst layer, the current density $i_{agg,CL}$(A/m^3) is expressed:

$$i_{agg,CL} = i_{agg}(1-\varepsilon) \quad (82)$$

In Eq. (81), the contribution of the electrochemical reaction to the agglomerate current is contained in the reaction rate k_c. In order to express this parameter, the current density given by the agglomerate model is expressed under the limiting condition of an homogeneous CL ($r_{agg}\to 0$, $\delta_{agg}\to 0$, $E_r\to 1$,):

$$i_{agg,CL} = (1-\varepsilon)4F\overline{V_{agg}}C_{O2,(film|gas)}k_c \;\to\; i_r \quad (83)$$

$$k_c = \frac{i_{\mathrm{r}}}{(1-\varepsilon)4F\overline{V_{agg}}P_{O2}\,H_{O2}} \quad (84)$$

with i_r the current density expressed with the Butler-Volmer expression:

$$i_r = i_0\cdot L_S\cdot\frac{P_{O2}\,H_{O2}}{P_{ref}\,H_{O2}}\left[\exp\left(\frac{\alpha n_C F}{RT}\left(\eta-\frac{R_\Omega}{L_s}i_r\right)\right)-\exp\left(\frac{-(1-\alpha)n_C F}{RT}\left(\eta-\frac{R_\Omega}{L_s}i_r\right)\right)\right] \quad (85)$$

This expression takes into account the assumption of a first order reaction towards O_2 (see Eq. (74)). The parameters i_0, n_C and R_Ω determined on SECM measurements (see Chapter III) are included in the equation. As i_0 and R_Ω were measured per unit of catalyst volume (the volume fraction of Nafion used during the SECM measurements is neglected), a scaling factor L_S is applied in order to express them per unit of catalyst layer volume (solid phase + ionomer phase + gaseous phase).

IV.4. Analysis of the cell performance with the agglomerate model

IV.4.1. Model validation

The model is implemented with the parameters values corresponding to an experiment performed by a partner of the PEGASUS project: Heraeus Precious Metals – Hydrogen Systems. A catalyst coated membrane (CCM) of 50 cm^2 was realized with the bar coating technique on a Gore 820.15 membrane. The loading in CEA-BRF02 catalyst at the cathode was 2.2 $mg_{BRF02}.cm^{-2}$, with an I/C ratio of 0.67. At the anode, a 20 %wt Pt/C catalyst was used with a loading of 0.22 $mg_{Pt}.cm^{-2}$ and an I/C ratio of 1. Two H23C7 GDL from Freudenberg and two multichannel serpentine bipolar plates were added to the MEA to form a single cell PEMFC. The physico-chemical properties of the different components are well known in CEA-Grenoble, thanks to their long experience of fuel cell characterization and modeling. They are detailed in the Table 7 of Annex 3. A polarization curve was performed following the protocol established within the PEGASUS project (see Table 8 in Annex 3). After the electrochemical characterization, the MEA was sent to the CEA-Grenoble and imaged with SEM. The images are presented on Figure 49 and enable to evaluate the thickness of the electrodes (30 µm at the cathode and 20 µm at the anode), the agglomerate size in the cathode (1 µm) and the pore radius in the anode (100 nm). Then the other CL and agglomerate parameters are determined with the method presented in part IV.3.1.

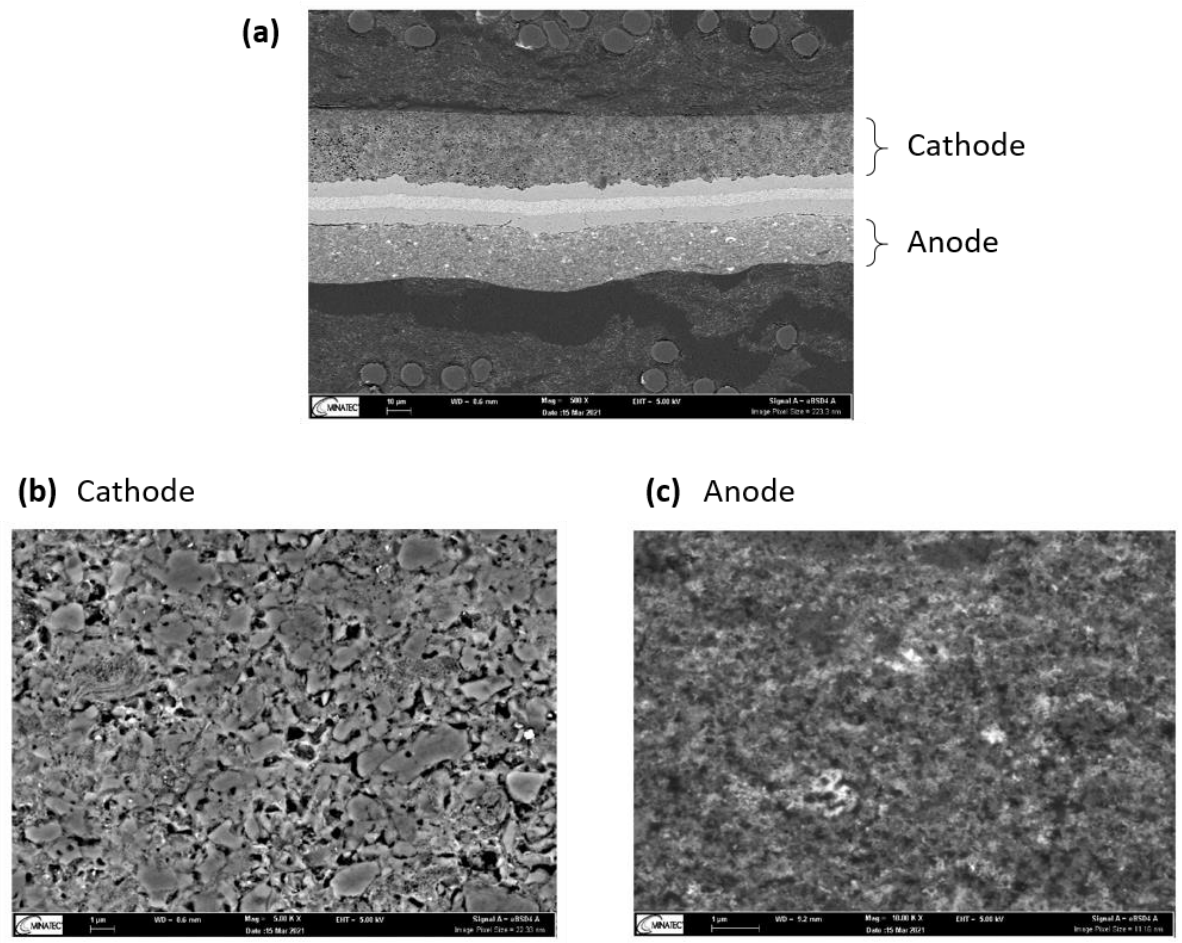

Figure 49: SEM imaging of the MEA used to validate the numerical model. (a) Zoom on the CL and the membrane. (b) Zoom on the cathode CL. (c) Zoom on the anode CL.

In order to be able to fit the experimental data with the numerical model, two parameters need to be adjusted. First, the symmetry factor of the ORR α_c is modified to 0.55 in order to fit the kinetic part of the curve. Then, the ohmic resistance R_Ω is set to 1.1 x 10^{-9} Ω.m^3 instead of the SECM-determined value of 1.94 x 10^{-8} Ω.m^3 in order to fit the ohmic region of the polarization curve. The dissimilarities between the measurement conditions of the two techniques could explain the difference in the estimation of R_Ω. Indeed, SECM is performed on very dispersed material, whereas in single cell conditions, the catalyst is embedded in a layer that is compressed within the cell. The connection between the particles is probably better in single cell measurements than in SECM conditions. This may explain the lower value of R_Ω estimated on the single cell polarization curve. As concerns the exchange current density i_0 and the number of electrons exchanged n_C, the values determined with SECM do not need to be adjusted by the numerical model. This is a good indicator of the quality of the estimations done with SECM. Figure 50 shows the experimental and the modeled polarization curves.

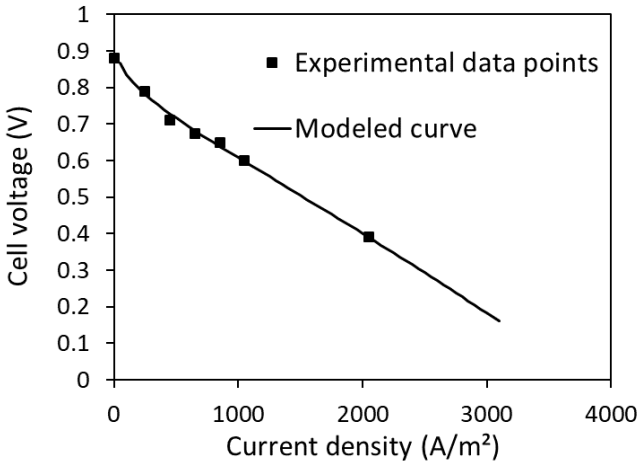

Figure 50: Experimental and modeled polarization curve of the MEA characterization of BRF02 catalyst performed by Heraeus Precious Metals – Hydrogen Systems.

IV.4.2. Investigation of the CL and agglomerate properties on the MEA performance

The influence of the cathodic CL composition and of the agglomerates dimensions on the cell performance are investigated in this part. Different parameters are varied and the polarization curves obtained are compared to the one fitted on the Heraeus Precious Metals – Hydrogen Systems experiment. The values of the parameters for this "base case" are summarized in Table 3.

Parameters that will be varied		**Deduced CL and agglomerate composition**	
m_S	0.022 kg.m^{-2}	L_S	0.325
$e_{CL,c}$	30 µm	L_i	0.22
I/C_c	0.67	ε	0.455
r_{agg}	1 µm	$L_{i,agg}$	0.4
$L_{i,agg}^{max}$	0.5	δ_{agg}	0 nm

Table 3: Main agglomerate and CL parameters at the cathode.

Figure 51 (a) shows the effect of varying the loading in catalyst m_S. Adding more carbon material in the layer for a constant thickness increases the amount of catalyst available for the electrochemical reaction but decreases the porosity. Here, the performance is increasing with the loading, indicating that the transport in gas phase is not limiting in this case. The porosity can thus be reduced without losing performance. This is also observed when the thickness of the cathode $e_{CL,c}$ is decreased without varying the loading of catalyst: the transport losses along the electrode are reduced and the performance is increasing despite the diminution of porosity (see Figure 51 (b)).

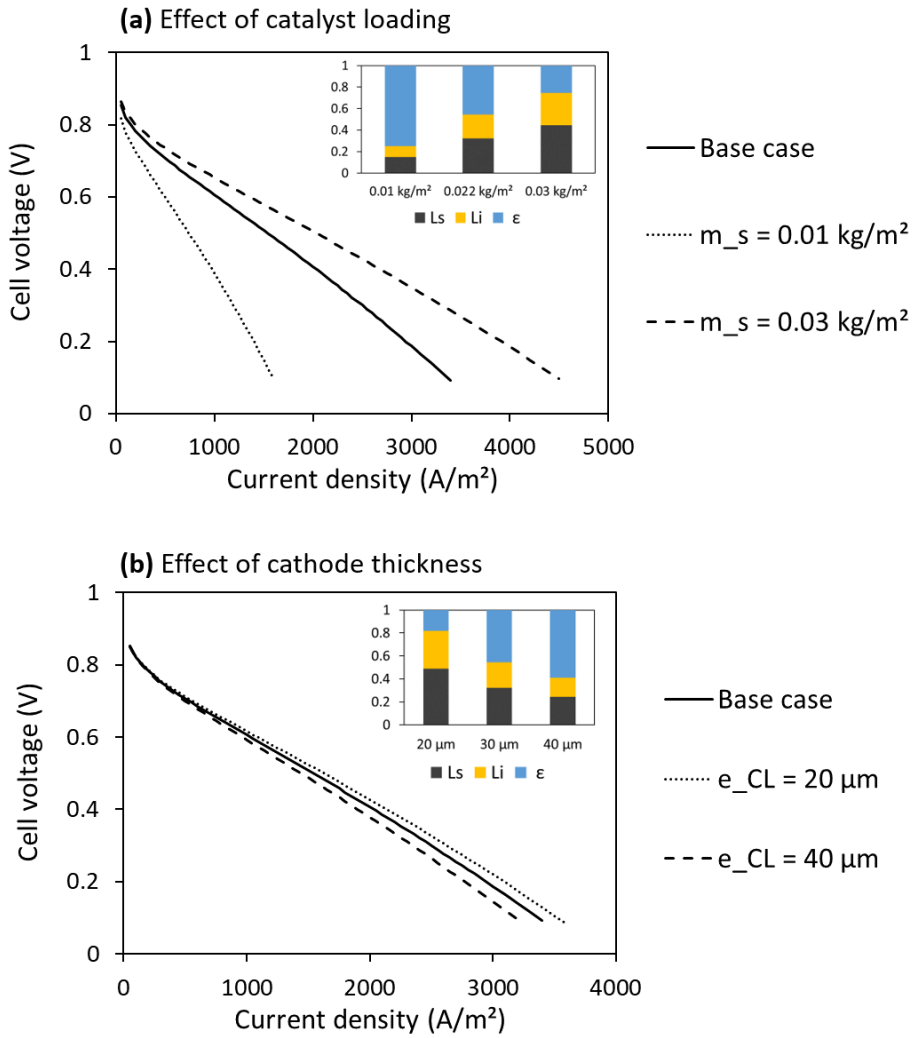

Figure 51: Influence of (a) the catalyst loading and (b) the cathodic CL thickness on the cell performance. The CL composition for each case is presented in the insets.

The effect of the ionomer to carbon ratio I/C_c is now studied (see Figure 52 (a)). Adding more ionomer decreases the porosity and increases the ionomer conductivity of the cathodic CL. As the transport in gas phase is not limiting, the performance is increasing. The ionomer can be embedded in the agglomerate core or it can

also form a thin layer surrounding the agglomerate. Different repartitions of the ionomer are studied in Figure 52 (b) by varying the maximal fraction of ionomer in the agglomerate core $L_{i,agg}^{max}$ for a value of $I/C_c = 2$. The less ionomer in the agglomerate core, the thicker is the ionomer layer surrounding the agglomerate and the worse is the performance. This means that the transport of oxygen is optimized when the ionomer phase is situated within the agglomerate core, instead of around it. Practically, the ability of the ionomer to penetrate the pores of the carbon structure depends on its equivalent weight, a smaller EW will allow the ionomer the penetrate more easily the micropores [220].

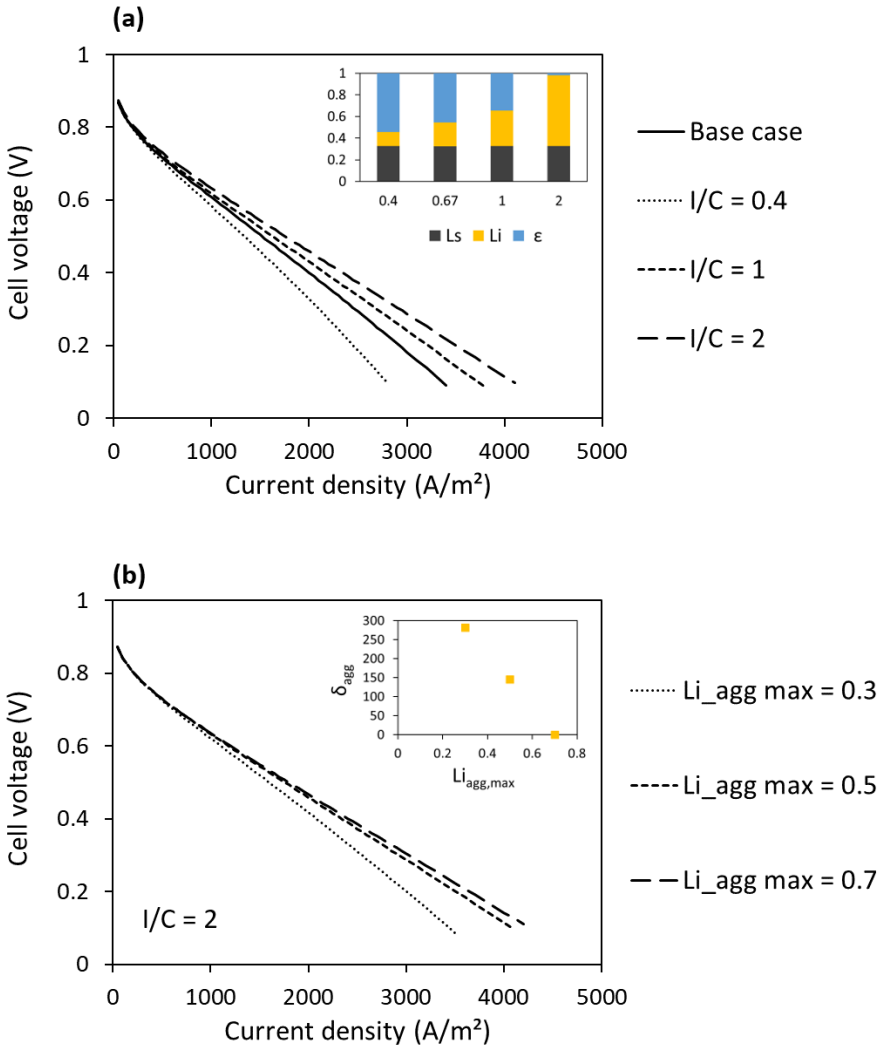

Figure 52: Influence on the cell performance of the amount of ionomer (a) and of its repartition within the agglomerate (b). Insets are showing the composition of the CL in (a) and the thickness of the ionomer layer surrounding the agglomerate in (b).

Finally, the radius of the agglomerates r_{agg} is investigated for the base case where all the ionomer is embedded in the agglomerate core. Figure 53 shows that decreasing the size of the agglomerate increases the

cell performance. Indeed, the catalytic sites are more accessible when the agglomerates are smaller, the core of the agglomerate being more easily reachable by the dissolved O_2.

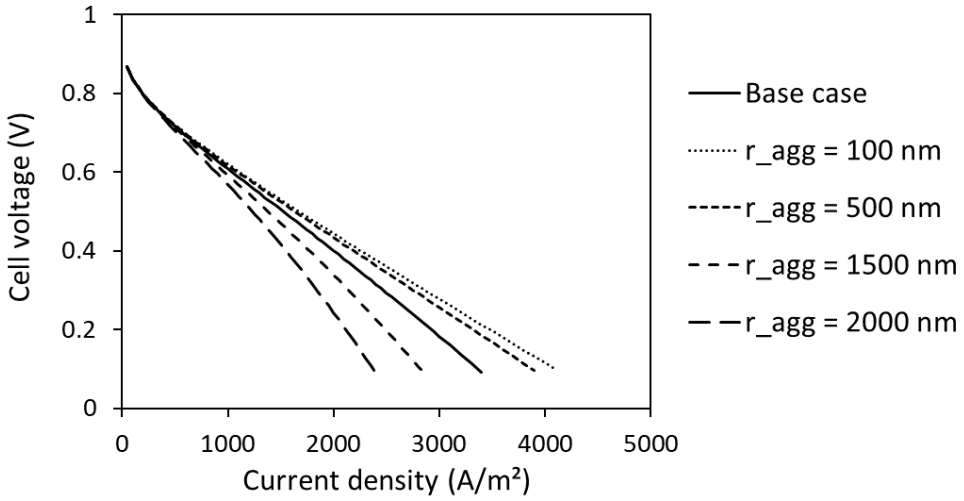

Figure 53: Influence of the agglomerate radius on the cell performance.

In conclusion, the variation of different CL and agglomerate parameters enabled to highlight that in the case studied here, the porosity of the layer is not limiting. Thus, more catalytic material could be embedded in the layer in order to increase the performance. However, the increase of the thickness has to be treated carefully as it will create supplementary transport losses along the cathode. The addition of more ionomer to the solid phase will increase the ionic conductivity of the layer and thus the performance. The optimal integration of the ionomer phase is to integrate it within the agglomerate core without forming a layer surrounding the agglomerate. A better dispersion of the catalyst is also wanted in order to decrease the size of the agglomerates and improve the diffusion of O_2 to the catalytic sites.

IV.5. Conclusion

This chapter aimed at building a PGM-free agglomerate model including the kinetic parameters determined with the SECM measurements. A 1D MEA model developed by the CEA-Grenoble was modified in order to simulate the diffusion of O_2 in the agglomerates at the cathode. The parameters i_0, n_C and R_Ω determined in the Chapter III were integrated in the model. A polarization curve performed by Heraeus Precious Metals – Hydrogen Systems served for the model validation. While the SECM-determined values of i_0 and n_C

did not need to be adjusted with the MEA model, the ohmic resistance R_{Ω} was lower in single cell condition compared to the value obtain with the SECM measurements. The reason for this lower value could be the higher compression of the material within the CL of the cell, which increase the connectivity between the catalyst particles. Finally, the model was used to investigate the effect of the CL and agglomerate parameters. Different compositions and different agglomerate sizes were compared and the best performance was achieved when the porosity and the agglomerate size were decreased. The importance to embed the ionomer within the agglomerate core instead of around it was also noticed. Similar conclusions were drawn in the literature: the PGM-free models presented in part IV.1.2. highlighted the important losses caused by large agglomerates [64] or by a thick Nafion film around them [61], [64]. A limitation of the model developed in this chapter would be the fact that the liquid water management was not resolved. This choice was made to limit the complexity of the numerical model. According to the literature, water flooding plays however a key role on the performance of PGM-free fuel cells [63], [65], [209], [211]. It would be thus interesting resolve the two phases water flow in future modeling works.

Conclusion and perspectives

Fuel cells and especially PEMFC are envisioned to take part in the replacement of thermal vehicles in the coming years. Even if this technology is already commercially available, the research is still very active in order to reduce the costs and improve the efficiency of the PEMFC. Notably, the replacement of the Pt/C catalyst by non-PGM materials creates new challenges towards the materials synthesis, characterization and integration into the catalyst layers. The complex architecture of the CL makes it difficult to process and to characterize, especially with PGM-free catalysts.

In this context, this thesis aimed at investigating the link between the structural properties and the electrocatalytic activity of PGM-free ORR catalysts for PEMFC fuel cells. In the framework of the European project PEGASUS, two approaches were explored. First, an experimental methodology based on local probe techniques (SECM and AFM) enabled the investigation of different materials at agglomerate scale, as well as the extraction of kinetic parameters. Then, the link between the structural properties and the electrocatalytic activity of the materials was explored at the single cell scale through numerical simulations involving the experimental parameters determined with the SECM and AFM protocol.

The first chapter gave an overview on the main issues regarding the development of PEMFC with PGM-free materials. The place of hydrogen and fuel cells in the energetic transition was briefly discussed and the importance of reducing the costs of the PEMFC was highlighted. Different research strategies for reducing the amount of platinum or replacing it with cheaper and more abundant materials were presented. The focus was put on the PGM-free catalysts, since these materials were investigated within the PEGASUS project. The various morphologies obtained with the different synthesis methods raised the issue of their integration into catalyst layers. Different fabrication processes and characterization methods were rewieved and the importance of being able to characterize the materials and the structures at several scales was brought to light.

The second chapter presented the development of an experimental methodology based on local probe techniques in order to characterize ORR PGM-free catalysts at agglomerate scale. Scanning electrochemical microscopy and atomic force microscopy were introduced and their interest for the characterization of an ensemble of catalyst particles was discussed. The implementation of the measurement protocol was detailed. The methodology was demonstrated with a benchmarking study of several catalysts provided by partners of the PEGASUS project. A different agglomeration of the materials towards the same ink formulation was highlighted. Despite the non-optimal ink formulation of some of the materials, the SECM and AFM

measurements enabled to link the agglomeration state to the electrochemical activity of the deposits, and to explain the measurements on specific deposits. The effects of the intrinsic activity and of the agglomeration state on the performance of the deposits were identified. Notably, the amplification of the performance differences towards an increase of the loading was attributed to the different agglomeration states of the materials. The effect of the dispersion method and of the Nafion content were investigated on the material developed in the LICSEN (CEA-BRF02). The decantation in the Sonotek affects the amount of material deposited on the substrate. As long as the catalytic activity was expressed towards the exact volume of material measured with AFM, this phenomenon did not affect the investigation of the activity of the catalysts. This study showed that the formulation and deposition process of a material has a strong influence on its performance, even at agglomerate scale.

The third chapter broadened the methodology presented in the second chapter with the development of a numerical modeling approach of the SECM set-up in order to extract kinetic parameters from SECM and AFM characterizations on the CEA-BRF02 catalyst. The experimental protocol was completed with SECM measurements of the H_2O_2 produced by the ORR in order to investigate the selectivity of the catalyst. After a review of the modeling approachs existing in the literature, the model developed in this work was described. The determination procedure of the exchange current density and the ORR selectivity was detailed. An ohmic phenomenon was observed and quantified. It was interpreted as local ohmic drop at the catalyst agglomerates due to resistive paths inside the particles or contact resistances between the particles and the substrate.

The fourth chapter aimed at studying the relationship between the structure and the activity of PGM-free materials at the single cell scale, by performing numerical simulations of a membrane electrode assembly. A model developed in the CEA-Grenoble was modified in order to include the kinetic parameters determined in the third chapter. Moreover, an agglomerate model was integrated to describe more finely the crucial phenomena occurring in the cathodic CL. The ability to fit an experimental polarization curve with the SECM-derived parameters implemented in the MEA model gave an additional confirmation of the accuracy of the method developed in the third chapter. Important ohmic losses were observed on the experimental polarization curve and a similar resistance than in chapter III was included in the model. Simulations were performed in order to investigate the effect of the CL composition and the agglomerates parameters. The reduction of the porosity through the addition of catalytic material or ionomer led to higher performance. The importance of decreasing the size of the agglomerates and embed the ionomer in their core was highlighted.

By studying the link between the structural properties and the electrocatalytic activity of PGM-free materials with different approaches, this thesis highlighted the importance of controlling the fabrication process of the materials from agglomerate scale to MEA scale. Transport losses caused by the agglomeration

of the particles is one of the major reasons for the decrease in performance of a material. While the SECM and AFM based characterization method is interesting to investigate the effect of agglomeration on the intrinsic parameters at a micrometric scale, MEA modeling gives a larger overview on the global phenomena affecting the performance in a constituted CL. Combining the two approaches enables to get a deeper understanding on this subject.

The methodology developed during the PhD can be adapted to various applications, from the investigation of the intrinsic activity of materials to the optimization of a formulation process. The link between the agglomerates morphology and their activity could be further studied by analyzing for example the ratio between the surface and the volume of the agglomerates. The stability of PGM-free catalysts could also be studied with this method at agglomerate scale. Indeed, stability is one important bottleneck of the development of these materials [221]. Finally, many other electrocatalytic reactions can be studied with this technique, such as the hydrogen oxidation reaction (HOR), the hydrogen evolution reaction (HER) or oxygen evolution reaction (OER).

Annex 1: AFM data treatment

The treatment of the AFM data consists in two steps. First, the image processing software Gwyddion is used on each image to detect the particles and extract their height (m), volume (m^3), projected area (number of pixels) and external surface (m^2). These data are exported in a *.txt* file where each line represents a particle. Then, a Python routine is used to calculate the volume of material in the deposit and build the distribution of particles sizes. The code creates an Excel file on which the information whether a sufficient number of AFM images were acquired is easily identifiable. This file can be easily saved and modified in a later time. The code is detailed as follows:

```
import os
import xlsxwriter
import numpy
import matplotlib
from pylab import *

os.chdir(r"C:\Users\ab252876\Documents\Thèse\Manips\Manips septembre 2020\200831-Dépôt billes\200929-AFM depôt billes du 3108\25% 2p")    ### Txt files location

# Creation of an Excel file

classeur_spot = xlsxwriter.Workbook('201002-Billes 25% 2p.xlsx')
feuille1 = classeur_spot.add_worksheet('infos_générales')
feuille2 = classeur_spot.add_worksheet('distribution_volumes')


# Information on the images to process

longueur_spot=195 # en µm     #### Deposit dimensions
largeur_spot=206 # en µm
surface_spot=longueur_spot*largeur_spot

surface_image=[100*100]*0+[50*50]*5 # en µm²       ### Size and number of AFM images to process
poids=[4]*0+[1]*5          ### Weights for calculating the mean value : 1 for 50µm images and 4 for 100 µm images
liste_images=["201001-Billes du 3108-25% 2p-000"  ### Txt files for each AFM image
        ,"201001-Billes du 3108-25% 2p-001"
        ,"201001-Billes du 3108-25% 2p-002"
        ,"201001-Billes du 3108-25% 2p-003"
        ,"201001-Billes du 3108-25% 2p-004"
       ]

noms_images=['000'  ### Name of the AFM images
             ,'001'
             ,'002'
             ,'003'
             ,'004'
             ]


# Data extraction from the txt files

nbel=len(liste_images)
volumes_images=[0]*nbel
données=[]

for k in range(nbel) :
    if poids[k]==1:
        x=9.54e-15  # 1 pixel = 9.54e-15 m² (conversion of the projected surface area from pixels to m²)
    else:
        x=3.81e-14  # 1 pixel = 3.81e-14 m² (conversion of the projected surface area from pixels to m²)
    nomtxt=liste_images[k] + '.txt'
    with open(nomtxt,"r") as fichier:
        contenu=loadtxt(fichier)

    for i in range(shape(contenu)[0]) :
```

```
        haut=contenu[i,0]  ### Data extraction (only the volume serves for the method presented in the manuscript)
        pix=contenu[i,1]
        surf=contenu[i,2]
        vol=contenu[i,3]
        surf_proj=pix*x
        données=données+[(haut,pix,surf_proj,surf,vol)]   ### Creation of an array regrouping the data from all the images
        volumes_images[k]=volumes_images[k]+vol   ### Total volume in each image

nbpart=len(données)


# Sheet 1 : Estimation of the total volume of material in the deposit + determination of the number of images necessary to get an accurate estimation

volume_extrapole_1=[0]*nbel
volume_extrapole_err=[0]*nbel
moyenne_volume=[0]*nbel
pre_std_vol=[0]*nbel
std_volume=[0]*nbel
ecsurmoy_vol=[0]*nbel

for k in range (nbel):
    volume_extrapole_1[k]=volumes_images[k]*surface_spot/surface_image[k]   ### Volume in the deposit extrapolated from one AFM image
    moyenne_volume[k]=dot(volume_extrapole_1[0:k+1],poids[0:k+1])/sum(poids[0:k+1])   ### Volume in the deposit extrapolated from the first k AFM images
    pre_std_vol[k]=(volume_extrapole_1[k]-moyenne_volume[k])**2
for k in range (1,nbel):
    std_volume[k]=sqrt(dot(pre_std_vol[0:k+1],poids[0:k+1])/(k/(k+1)*sum(poids[0:k+1])))  ### Standard deviation of the volume estimation
    ecsurmoy_vol[k]=std_volume[k]/moyenne_volume[k]*100   ### Standard deviation of the volume estimation (in % of the average value)
for k in range (nbel-1):
    volume_extrapole_err[k+1]=(moyenne_volume[k+1]-moyenne_volume[k])/moyenne_volume[k+1]*100  ### Variation of the extrapolated volume towards the number of AFM images

volume_total=sum(volumes_images)*surface_spot/sum(surface_image)  ### Volume in the deposit extrapolated from all the AFM images
voltotum=volume_total*1e18


# Sheet 1 : Writing in the Excel file

headings1=['Nombre d images prises en compte','Image','Vol extr 1 image (m3)','Poids','Moyenne vol extr k images','Variation des moyennes (%)','Ecart type (%)']
feuille1.write_row(0,0,headings1)
feuille1.write_column(1,0,arange(1,nbel+1,1))
feuille1.write_column(1,1,noms_images)
feuille1.write_column(1,2,volume_extrapole_1)
feuille1.write_column(1,3,poids)
feuille1.write_column(1,4,moyenne_volume)
feuille1.write_column(1,5,volume_extrapole_err)
feuille1.write_column(1,6,ecsurmoy_vol)
feuille1.write_column(1,12,[1]*nbel)
feuille1.write column(1,13,[nbel-1]*nbel)
feuille1.write_row(0,15,['Volume total (m3)'])
feuille1.write_row(1,15,[volume_total])
feuille1.write_row(2,15,[voltotum])

# Sheet 1 : Graphs creation in the Excel file

chart1=classeur_spot.add_chart({'type': 'scatter'})
chart1.add_series({'categories':['infos_générales',1,0,nbel,0],'values':['infos_générales',1,4,nbel,4],'name':'Extrapolated volume of catalyst (m3)'})
chart1.set_x_axis({'name': 'Number of images','name_font':{'size':12},'num_font':{'size':12},'line':{'color':'black'}})
chart1.set_y_axis({'name': 'Extrapolated volume (µm3)','name_font':{'size':12},'num_font':{'size':12},'major_gridlines':{'visible':False},'line':{'color':'black'}})
chart1.set_legend({'font':{'size':12},'position':'overlay_right','layout':{'x':0.2,'y':0.5,'width':0.7,'height':0.25}})
chart1.set_title({'none':True})
chart1.set plotarea({'border':{'color':'black'}})
chart1.set_chartarea({'border':{'none':True},'layout':{'x':0.2,'y':0.5,'width':0.7,'height':0.25}})
chart1.set_size({'y_scale':1.35,'x_scale':1.35})
feuille1.insert_chart('B12',chart1)


# Sheet 2 : Calculation of the particles sizes distribution

plages_volumes=logspace(-23,-14,50)  ### Definition of the ranges of particles volume
volumes nombre=[0]*len(plages volumes)
pourcentage_vol=[0]*len(plages_volumes)

for i in range (len(plages_volumes)-1): ### Particles sorting and counting
    compteur=0
    voltot=0
    for k in range(nbpart):
        if données[k][4] >= plages_volumes[i] and données[k][4] < plages_volumes[i+1]:
            compteur+=1
            voltot+=données[k][4]
    volumes_nombre[i]=compteur*surface_spot/sum(surface_image)
    pourcentage_vol[i]=voltot*surface_spot/sum(surface_image)/volume_total

plages_volumes_um=plages_volumes*1e18

feuille2.write_row(0,0,['Plage des volumes (µm3)','Nombre de particules dans la plage','Pourcentage du volume total dans la plage']) ### Writing in the Excel file
feuille2.write_column(1,0,plages_volumes_um)
feuille2.write_column(1,1,volumes_nombre)
feuille2.write_column(1,2,pourcentage_vol)


classeur_spot.close()
```

Annex 2: SECM model parameters

Negative feedback

Active specie: O_2

Boundary condition at the probe active part: $C_{O2} = 0$

Boundary condition at the deposit of catalyst: no flux

Parameter	Value	Source
r_T	6.2 µm	Fitted on approach curves in negative feedback mode
RG	11	Fitted on approach curves in negative feedback mode
n_T	2.7	Fitted on approach curves in negative feedback mode
d	30 µm	SECM device
r_C	≈ 110 µm	Calculated from the surface of the deposit
C_0	1.27 mol.m^{-3}	[222]
D_{O2}	1.9 x 10^{-9} m^2.s^{-1}	[223]
T	293 K	Temperature during the SECM experiments

Table 4: SECM model parameters in negative feedback mode.

Substrate generation-tip collection (SG-TC)

Active specie: H_2O_2

Boundary condition at the probe active part: $C_{H2O2} = 0$

Simplified boundary condition at the deposit of catalyst: $C_{H2O2} = C_{O2}^{ref}$

Parameter	Value	Source
r_T	3.5 µm	Fitted on approach curves in negative feedback mode
RG	10.4	Fitted on approach curves in negative feedback mode
n_T	2.47	Fitted on approach curves in negative feedback mode
d	30 µm	SECM device
r_C	≈ 110 µm	Calculated from the surface of the deposit
C_0	0 mol.m^{-3}	No H_2O_2 in solution initially
D_{H2O2}	1.5 x 10^{-9} m^2.s^{-1}	[224]
T	293 K	Temperature during the SECM experiments
n_C	2	Fixed when the 2e$^-$ pathway is studied

Table 5: SECM model parameters in SG-TC mode.

Redox competition

Active specie: O_2

Boundary condition at the probe active part: $C_{O2} = 0$

Simplified boundary condition at the deposit of catalyst: $C_{O2} = 0$

Full boundary condition at the deposit of catalyst:

$$W_{O2} = \frac{i_0}{n_C F}\frac{C_{O2}}{C_{O2}^{ref}}\left[\exp\left(\frac{\alpha n_C F}{RT}(\eta - R_\Omega i_C)\right) - \exp\left(\frac{-(1-\alpha) n_C F}{RT}(\eta - R_\Omega i_C)\right)\right]\frac{V_{catalyst}}{S_{deposit}}$$

Parameter	Value	Source
r_T	6.2 µm	Fitted on approach curves in negative feedback mode
RG	11	Fitted on approach curves in negative feedback mode
n_T	2.7	Fitted on approach curves in negative feedback mode

d	30 µm	Fixed by SECM protocol
r_C	≈ 110 µm	Calculated from the surface of the deposit
C_0	1.27 mol.m^{-3}	[222]
D_{O2}	1.9 x 10^{-9} m^2.s^{-1}	[223]
T	293 K	Temperature during the SECM experiments
F	96 485 C.mol^{-1}	Faraday constant
R	8.314 J.mol^{-1}.K^{-1}	Universal gas constant
$S_{deposit}$	≈ 40 000 µm^2	Measured by optical microscope imaging
$V_{catalyst}$	1750 µm^3 – 35 400 µm^3	Determined from the AFM images
n_C	3.88	Calculated from the RC and SG-TC measurements
i_0	670 A.m^{-3}	Fitted with the model
R_Ω	1.94 x 10^{-8} Ω.m^3	Fitted with the model
α	0.5	Assumed
C_{O2}^{ref}	1.27 mol.m^{-3}	[222]

Table 6: SECM model parameters in RC mode.

Annex 3: MEA model parameters and operating conditions

Domains parameters	Cathode			Membrane	Anode		
	BP	GDL	CL	MB	CL	GDL	BP
Thickness e (m)	1.4 x 10^{-3}	2.3 x 10^{-4}	30 x 10^{-6}	1.5 x 10^{-5}	20 x 10^{-6}	2.3 x 10^{-4}	1.4 x 10^{-3}
Ionomer to carbon ratio I/C	-	-	0.67	-	1	-	-
Porosity ε	-	0.74	0.455	-	0.505	0.74	-
Tortuosity τ	-	1.7	1.5	1	1.5	1.7	-
Pores radius R_p (m)	-	1 x 10^{-5}	8.34 x 10^{-7}	-	1 x 10^{-7}	1 x 10^{-5}	-
Permeability k (m^2)	-	1.2 x 10^{-14}	1 x 10^{-12}	-	1 x 10^{-12}	1.2 x 10^{-14}	-
Electronic conductivity σ ($S.m^{-1}$)	1 x 10^5	206.8	20	-	20	206.8	1 x 10^5
Ionic conductivity κ ($S.m^{-1}$)	-	-	≈ 0.48	≈ 2.2	≈ 0.33	-	-

Thermal conductivity λ ($W.m^{-1}.K^{-1}$)	-	0.475	3	0.186	3	0.475	-

Table 7: MEA properties.

Parameter	**Value**
Anode inlet pressure (Pa)	3×10^5
Cathode inlet pressure (Pa)	3×10^5
Anode inlet relative humidity (%)	50
Cathode inlet relative humidity (%)	30
Anode inlet H_2 molar fraction	1
Cathode inlet O_2 molar fraction	0.21
Cell temperature (K)	353

Table 8: Operating conditions used during the characterizations done by Heraeus Precious Metals – Hydrogen Systems.

References

[1] « Fuel Cells and Hydrogen Joint Undertaking ». https://www.fch.europa.eu/

[2] « PEGASUS project ». https://www.pegasus-pemfc.eu/

[3] J. Wang, H. Wang, et Y. Fan, « Techno-Economic Challenges of Fuel Cell Commercialization », *Engineering*, vol. 4, nº 3, p. 352-360, juin 2018, doi: 10.1016/j.eng.2018.05.007.

[4] A. Morozan, P. Jégou, B. Jousselme, et S. Palacin, « Electrochemical performance of annealed cobalt–benzotriazole/CNTs catalysts towards the oxygen reduction reaction », *Phys. Chem. Chem. Phys.*, vol. 13, nº 48, p. 21600, 2011, doi: 10.1039/c1cp23199e.

[5] O. Henrotte *et al.*, « Electronic Transport of MoS_2 Monolayered Flakes Investigated by Scanning Electrochemical Microscopy », *ChemPhysChem*, vol. 18, nº 19, p. 2777-2781, oct. 2017, doi: 10.1002/cphc.201700343.

[6] O. Henrotte *et al.*, « Steady-State Electrocatalytic Activity Evaluation with the Redox Competition Mode of Scanning Electrochemical Microscopy: A Gold Probe and a Boron-Doped Diamond Substrate », *ChemElectroChem*, vol. 7, nº 22, p. 4633-4640, nov. 2020, doi: 10.1002/celc.202001088.

[7] V. Masson-Delmotte, Intergovernmental Panel on Climate Change, WMO, et United Nations Environment Programme, *Global warming of 1.5 ºC: an IPCC special report on the impacts of global warming of 1.5 °C above pre-industrial levels and related global greenhouse gas emission pathways, in the context of strengthening the global response to the threat of climate change, sustainable development, and efforts to eradicate poverty: summary for policy-makers*. Geneva: Intergovernmental Panel on Climate Change, 2018.

[8] Fuel Cells and Hydrogen 2 Joint Undertaking., *Hydrogen roadmap Europe: a sustainable pathway for the European energy transition.* LU: Publications Office, 2019. Consulté le: juin 06, 2021. [En ligne]. Disponible sur: https://data.europa.eu/doi/10.2843/341510

[9] IEA, « Tracking Transport 2020 », Paris, 2020. [En ligne]. Disponible sur: https://www.iea.org/reports/tracking-transport-2020

[10] J. Walkowiak-Kulikowska, J. Wolska, et H. Koroniak, « Polymers application in proton exchange membranes for fuel cells (PEMFCs) », *Physical Sciences Reviews*, vol. 2, nº 8, août 2017, doi: 10.1515/psr-2017-0018.

[11] S. Mekhilef, R. Saidur, et A. Safari, « Comparative study of different fuel cell technologies », *Renewable and Sustainable Energy Reviews*, vol. 16, nº 1, p. 981-989, janv. 2012, doi: 10.1016/j.rser.2011.09.020.

[12] A. Kongkanand et M. F. Mathias, « The Priority and Challenge of High-Power Performance of Low-Platinum Proton-Exchange Membrane Fuel Cells », *J. Phys. Chem. Lett.*, vol. 7, nº 7, p. 1127-1137, avr. 2016, doi: 10.1021/acs.jpclett.6b00216.

[13] European Commission, « Critical materials for strategic technologies and sectors in the EU - a foresight study ». 2020.

[14] W. Xia, A. Mahmood, Z. Liang, R. Zou, et S. Guo, « Earth-Abundant Nanomaterials for Oxygen Reduction », *Angew. Chem. Int. Ed.*, vol. 55, nº 8, p. 2650-2676, févr. 2016, doi: 10.1002/anie.201504830.

[15] X. Ren *et al.*, « Current progress of Pt and Pt-based electrocatalysts used for fuel cells », *Sustainable Energy Fuels*, vol. 4, nº 1, p. 15-30, 2020, doi: 10.1039/C9SE00460B.

[16] K. Bhunia, S. Khilari, et D. Pradhan, « Trimetallic PtAuNi alloy nanoparticles as an efficient electrocatalyst for the methanol electrooxidation reaction », *Dalton Trans.*, vol. 46, nº 44, p. 15558-15566, 2017, doi: 10.1039/C7DT02608K.

[17] A. Jackson, A. Strickler, D. Higgins, et T. Jaramillo, « Engineering Ru@Pt Core-Shell Catalysts for Enhanced Electrochemical Oxygen Reduction Mass Activity and Stability », *Nanomaterials*, vol. 8, nº 1, p. 38, janv. 2018, doi: 10.3390/nano8010038.

[18] N. Becknell *et al.*, « Control of Architecture in Rhombic Dodecahedral Pt–Ni Nanoframe Electrocatalysts »,

J. Am. Chem. Soc., vol. 139, nº 34, p. 11678-11681, août 2017, doi: 10.1021/jacs.7b05584.
[19] L. B. Venarusso, C. V. Boone, J. Bettini, et G. Maia, « Carbon-supported metal nanodendrites as efficient, stable catalysts for the oxygen reduction reaction », *J. Mater. Chem. A*, vol. 6, nº 4, p. 1714-1726, 2018, doi: 10.1039/C7TA08964C.
[20] H. You, F. Zhang, Z. Liu, et J. Fang, « Free-Standing Pt–Au Hollow Nanourchins with Enhanced Activity and Stability for Catalytic Methanol Oxidation », *ACS Catal.*, vol. 4, nº 9, p. 2829-2835, sept. 2014, doi: 10.1021/cs500390s.
[21] J.-Y. Park *et al.*, « Enhanced oxygen reduction reaction of Pt deposited Fe/N-doped bimodal porous carbon nanostructure catalysts », *Journal of Catalysis*, vol. 359, p. 46-54, mars 2018, doi: 10.1016/j.jcat.2017.12.033.
[22] T. Tsukihara *et al.*, « The Whole Structure of the 13-Subunit Oxidized Cytochrome c Oxidase at 2.8 A », *Science*, vol. 272, p. 1136-1144, 1996.
[23] R. Jasinski, « A New Fuel Cell Cathode Catalyst », *Nature*, vol. 201, p. 1212, 1964.
[24] S. Gupta, D. Tryk, I. Bae, W. Aldred, et E. Yeager, « Heat-treated polyacrylonitrile-based catalysts for oxygen electroreduction », *J Appl Electrochem*, vol. 19, nº 1, p. 19-27, janv. 1989, doi: 10.1007/BF01039385.
[25] E. Proietti *et al.*, « Iron-based cathode catalyst with enhanced power density in polymer electrolyte membrane fuel cells », *Nat Commun*, vol. 2, nº 1, p. 416, sept. 2011, doi: 10.1038/ncomms1427.
[26] Y. Deng *et al.*, « Atomic Fe-Doped MOF-Derived Carbon Polyhedrons with High Active-Center Density and Ultra-High Performance toward PEM Fuel Cells », *Adv. Energy Mater.*, vol. 9, nº 13, p. 1802856, avr. 2019, doi: 10.1002/aenm.201802856.
[27] J. Shui, C. Chen, L. Grabstanowicz, D. Zhao, et D.-J. Liu, « Highly efficient nonprecious metal catalyst prepared with metal–organic framework in a continuous carbon nanofibrous network », *Proc Natl Acad Sci USA*, vol. 112, nº 34, p. 10629-10634, août 2015, doi: 10.1073/pnas.1507159112.
[28] A. Serov *et al.*, « Highly stable precious metal-free cathode catalyst for fuel cell application », *Journal of Power Sources*, vol. 327, p. 557-564, sept. 2016, doi: 10.1016/j.jpowsour.2016.07.087.
[29] A. Serov, K. Artyushkova, et P. Atanassov, « Fe-N-C Oxygen Reduction Fuel Cell Catalyst Derived from Carbendazim: Synthesis, Structure, and Reactivity », *Adv. Energy Mater.*, vol. 4, nº 10, p. 1301735, juill. 2014, doi: 10.1002/aenm.201301735.
[30] A. Serov, M. H. Robson, M. Smolnik, et P. Atanassov, « Templated bi-metallic non-PGM catalysts for oxygen reduction », *Electrochimica Acta*, vol. 80, p. 213-218, oct. 2012, doi: 10.1016/j.electacta.2012.07.008.
[31] G. Wu, K. L. More, C. M. Johnston, et P. Zelenay, « High-Performance Electrocatalysts for Oxygen Reduction Derived from Polyaniline, Iron, and Cobalt », *Science*, vol. 332, nº 6028, p. 443-447, avr. 2011, doi: 10.1126/science.1200832.
[32] H. T. Chung *et al.*, « Direct atomic-level insight into the active sites of a high-performance PGM-free ORR catalyst », *Science*, vol. 357, nº 6350, p. 479-484, août 2017, doi: 10.1126/science.aan2255.
[33] Y. Wang et S. Berthon-Fabry, « One-Pot Synthesis of Fe-N-Containing Carbon Aerogel for Oxygen Reduction Reaction », *Electrocatalysis*, vol. 12, nº 1, p. 78-90, janv. 2021, doi: 10.1007/s12678-020-00633-8.
[34] Á. García *et al.*, « Fe doped porous triazine as efficient electrocatalysts for the oxygen reduction reaction in acid electrolyte », *Applied Catalysis B: Environmental*, vol. 264, p. 118507, mai 2020, doi: 10.1016/j.apcatb.2019.118507.
[35] A. Boudet *et al.*, « Unraveling the Link between Catalytic Activity and Agglomeration State with SECM and AFM », *submitted*.
[36] H. Zhang *et al.*, « High-performance fuel cell cathodes exclusively containing atomically dispersed iron active sites », *Energy Environ. Sci.*, vol. 12, nº 8, p. 2548-2558, 2019, doi: 10.1039/C9EE00877B.
[37] H. Tang, S. Peikang, S. P. Jiang, F. Wang, et M. Pan, « A degradation study of Nafion proton exchange membrane of PEM fuel cells », *Journal of Power Sources*, vol. 170, nº 1, p. 85-92, juin 2007, doi: 10.1016/j.jpowsour.2007.03.061.

[38] F. Jaouen, D. Jones, N. Coutard, V. Artero, P. Strasser, et A. Kucernak, « Toward Platinum Group Metal-Free Catalysts for Hydrogen/Air Proton-Exchange Membrane Fuel Cells », *Johnson Matthey Technology Review*, vol. 62, nº 2, p. 231-255, avr. 2018, doi: 10.1595/205651318X696828.
[39] Y. Guo *et al.*, « The Controllable Design of Catalyst Inks to Enhance PEMFC Performance: A Review », *Electrochem. Energ. Rev.*, nov. 2020, doi: 10.1007/s41918-020-00083-2.
[40] K. Artyushkova *et al.*, « Role of Surface Chemistry on Catalyst/Ionomer Interactions for Transition Metal–Nitrogen–Carbon Electrocatalysts », *ACS Appl. Energy Mater.*, vol. 1, nº 1, p. 68-77, janv. 2018, doi: 10.1021/acsaem.7b00002.
[41] G. Wang, L. Osmieri, A. G. Star, J. Pfeilsticker, et K. C. Neyerlin, « Elucidating the Role of Ionomer in the Performance of Platinum Group Metal-free Catalyst Layer via in situ Electrochemical Diagnostics », *J. Electrochem. Soc.*, vol. 167, nº 4, p. 044519, mars 2020, doi: 10.1149/1945-7111/ab7aa1.
[42] L. Osmieri *et al.*, « Utilizing ink composition to tune bulk-electrode gas transport, performance, and operational robustness for a Fe–N–C catalyst in polymer electrolyte fuel cell », *Nano Energy*, vol. 75, p. 104943, sept. 2020, doi: 10.1016/j.nanoen.2020.104943.
[43] P. Toudret, J.-F. Blachot, M. Heitzmann, et P.-A. Jacques, « Impact of the Cathode Layer Printing Process on the Performance of MEA Integrating PGM Free Catalyst », *Catalysts*, vol. 11, nº 6, p. 669, mai 2021, doi: 10.3390/catal11060669.
[44] L. Guo *et al.*, « Promoting Atomically Dispersed MnN_4 Sites *via* Sulfur Doping for Oxygen Reduction: Unveiling Intrinsic Activity and Degradation in Fuel Cells », *ACS Nano*, vol. 15, nº 4, p. 6886-6899, avr. 2021, doi: 10.1021/acsnano.0c10637.
[45] L. Osmieri, H. Wang, et K. C. Neyerlin, « Impact of Fabrication and Testing Parameters on the Performance of a Polymer Electrolyte Fuel Cell with Platinum Group Metal (PGM)-Free Cathode Catalyst », *J. Electrochem. Soc.*, vol. 168, nº 1, p. 014503, janv. 2021, doi: 10.1149/1945-7111/abd48e.
[46] J. Park et D. J. Myers, « Novel platinum group metal-free catalyst ink deposition system for combinatorial polymer electrolyte fuel cell performance evaluation », *Journal of Power Sources*, vol. 480, p. 228801, déc. 2020, doi: 10.1016/j.jpowsour.2020.228801.
[47] X. Yang *et al.*, « PGM-Free Fe/N/C and Ultralow Loading Pt/C Hybrid Cathode Catalysts with Enhanced Stability and Activity in PEM Fuel Cells », *ACS Appl. Mater. Interfaces*, vol. 12, nº 12, p. 13739-13749, mars 2020, doi: 10.1021/acsami.9b18085.
[48] L. Osmieri *et al.*, « Elucidation of Fe-N-C electrocatalyst active site functionality via in-situ X-ray absorption and operando determination of oxygen reduction reaction kinetics in a PEFC », *Applied Catalysis B: Environmental*, vol. 257, p. 117929, nov. 2019, doi: 10.1016/j.apcatb.2019.117929.
[49] T. Hottinen et O. Himanen, « PEMFC temperature distribution caused by inhomogeneous compression of GDL », *Electrochemistry Communications*, vol. 9, nº 5, p. 1047-1052, mai 2007, doi: 10.1016/j.elecom.2006.12.018.
[50] T. Agaësse, « Simulations of one and two-phase flows in porous microstructures, from tomographic images of gas diffusion layers of proton exchange membrane fuel cells. », Université de Toulouse, 2016.
[51] S. A. Vilekar et R. Datta, « The effect of hydrogen crossover on open-circuit voltage in polymer electrolyte membrane fuel cells », *Journal of Power Sources*, vol. 195, nº 8, p. 2241-2247, avr. 2010, doi: 10.1016/j.jpowsour.2009.10.023.
[52] S. S. Kocha *et al.*, « Best Practices and Testing Protocols for Benchmarking ORR Activities of Fuel Cell Electrocatalysts Using Rotating Disk Electrode », *Electrocatalysis*, vol. 8, nº 4, p. 366-374, juill. 2017, doi: 10.1007/s12678-017-0378-6.
[53] Y. Lv, H. Liu, J. Li, J. Chen, et Y. Song, « A convenient protocol for the evaluation of commercial Pt/C electrocatalysts toward oxygen reduction reaction », *Journal of Electroanalytical Chemistry*, p. 11, 2020.
[54] M. Mazzucato *et al.*, « Effects of the induced micro- and meso-porosity on the single site density and turn over frequency of Fe-N-C carbon electrodes for the oxygen reduction reaction », *Applied Catalysis B: Environmental*, vol. 291, p. 120068, août 2021, doi: 10.1016/j.apcatb.2021.120068.
[55] X. Zhang *et al.*, « Nitrogen and Phosphate Co-doped Graphene as Efficient Bifunctional Electrocatalysts by Precursor Modulation Strategy for Oxygen Reduction and Evolution Reactions », *ChemElectroChem*, p.

celc.202100599, juin 2021, doi: 10.1002/celc.202100599.
[56] F. Jaouen, V. Goellner, M. Lefèvre, J. Herranz, E. Proietti, et J. P. Dodelet, « Oxygen reduction activities compared in rotating-disk electrode and proton exchange membrane fuel cells for highly active FeNC catalysts », *Electrochimica Acta*, vol. 87, p. 619-628, janv. 2013, doi: 10.1016/j.electacta.2012.09.057.
[57] A. R. Zeradjanin, « Frequent Pitfalls in the Characterization of Electrodes Designed for Electrochemical Energy Conversion and Storage », *ChemSusChem*, vol. 11, nº 8, p. 1278-1284, avr. 2018, doi: 10.1002/cssc.201702287.
[58] X. Meng, D. Yang, S. Wang, X. Liu, et W. Wang, « A high performance ORR electrocatalyst—Mn-N5-C/G: design, synthesis, and related mechanism », *Ionics*, juin 2021, doi: 10.1007/s11581-021-04154-2.
[59] A. Serov *et al.*, « Nano-structured platinum group metal-free catalysts and their integration in fuel cell electrode architectures », *Applied Catalysis B: Environmental*, vol. 237, p. 1139-1147, déc. 2018, doi: 10.1016/j.apcatb.2017.08.067.
[60] U. Martinez, S. Komini Babu, E. F. Holby, H. T. Chung, X. Yin, et P. Zelenay, « Progress in the Development of Fe-Based PGM-Free Electrocatalysts for the Oxygen Reduction Reaction », *Adv. Mater.*, vol. 31, nº 31, p. 1806545, août 2019, doi: 10.1002/adma.201806545.
[61] S. Komini Babu, H. T. Chung, P. Zelenay, et S. Litster, « Resolving Electrode Morphology's Impact on Platinum Group Metal-Free Cathode Performance Using Nano-CT of 3D Hierarchical Pore and Ionomer Distribution », *ACS Appl. Mater. Interfaces*, vol. 8, nº 48, p. 32764-32777, déc. 2016, doi: 10.1021/acsami.6b08844.
[62] S. Stariha *et al.*, « PGM-free Fe-N-C catalysts for oxygen reduction reaction: Catalyst layer design », *Journal of Power Sources*, vol. 326, p. 43-49, sept. 2016, doi: 10.1016/j.jpowsour.2016.06.098.
[63] S. Komini Babu, H. T. Chung, G. Wu, P. Zelenay, et S. Litster, « Modeling Hierarchical Non-Precious Metal Catalyst Cathodes for PEFCs Using Multi-Scale X-ray CT Imaging », *ECS Transactions*, vol. 64, nº 3, p. 281-292, août 2014, doi: 10.1149/06403.0281ecst.
[64] S. Komini Babu, H. T. Chung, P. Zelenay, et S. Litster, « Modeling Electrochemical Performance of the Hierarchical Morphology of Precious Group Metal-Free Cathode for Polymer Electrolyte Fuel Cell », *J. Electrochem. Soc.*, vol. 164, nº 9, p. F1037-F1049, 2017, doi: 10.1149/2.0041712jes.
[65] J. Liu *et al.*, « Understanding the Role of Interfaces for Water Management in Platinum Group Metal-Free Electrodes in Polymer Electrolyte Fuel Cells », *ACS Appl. Energy Mater.*, vol. 2, nº 5, p. 3542-3553, mai 2019, doi: 10.1021/acsaem.9b00292.
[66] Y. Liang *et al.*, « Electrochemical Scanning Probe Microscopies in Electrocatalysis », *Small Methods*, vol. 3, nº 8, p. 1800387, août 2019, doi: 10.1002/smtd.201800387.
[67] R. Kempaiah, G. Vasudevamurthy, et A. Subramanian, « Scanning probe microscopy based characterization of battery materials, interfaces, and processes », *Nano Energy*, vol. 65, p. 103925, nov. 2019, doi: 10.1016/j.nanoen.2019.103925.
[68] C. G. Zoski et M. V. Mirkin, « Steady-State Limiting Currents at Finite Conical Microelectrodes », *Anal. Chem.*, vol. 74, p. 1986-1992, 2002, doi: 10.1021/ac015669i.
[69] R. Cornut et C. Lefrou, « A unified new analytical approximation for negative feedback currents with a microdisk SECM tip », *Journal of Electroanalytical Chemistry*, vol. 608, nº 1, p. 59-66, sept. 2007, doi: 10.1016/j.jelechem.2007.05.007.
[70] N. L. Ritzert, J. Rodríguez-López, C. Tan, et H. D. Abruña, « Kinetics of Interfacial Electron Transfer at Single-Layer Graphene Electrodes in Aqueous and Nonaqueous Solutions », *Langmuir*, vol. 29, nº 5, p. 1683-1694, févr. 2013, doi: 10.1021/la3042549.
[71] J. Zhang, J. Guo, D. Chen, J.-H. Zhong, J.-Y. Liu, et D. Zhan, « Heterogeneous electron transfer kinetics of defective graphene investigated by scanning electrochemical microscopy », *Applied Surface Science*, vol. 491, p. 553-559, oct. 2019, doi: 10.1016/j.apsusc.2019.06.181.
[72] A. Asserghine, M. Medvidović-Kosanović, A. Stanković, L. Nagy, R. M. Souto, et G. Nagy, « A scanning electrochemical microscopy characterization of the localized corrosion reactions occurring on nitinol in saline solution after anodic polarization », *Sensors and Actuators B: Chemical*, vol. 321, p. 128610, oct. 2020, doi: 10.1016/j.snb.2020.128610.

[73] R. M. P. Silva, M. X. Milagre, L. A. Oliveira, U. Donatus, R. A. Antunes, et I. Costa, « The local electrochemical behavior of the AA2098-T351 and surface preparation effects investigated by scanning electrochemical microscopy », *Surf Interface Anal*, vol. 51, nº 10, p. 982-992, oct. 2019, doi: 10.1002/sia.6682.

[74] J. Zhang *et al.*, « Kinetic Investigation on the Confined Etching System of n-Type Gallium Arsenide by Scanning Electrochemical Microscopy », *J. Phys. Chem. C*, vol. 118, nº 32, p. 18604-18611, août 2014, doi: 10.1021/jp5056446.

[75] M. A. Brites Helú et J. L. Fernández, « Strategies for fabrication of highly-dense ordered arrays of metal microdisks by the scanning electrochemical microscopy microwriting approach », *Sensors and Actuators B: Chemical*, vol. 250, p. 420-428, oct. 2017, doi: 10.1016/j.snb.2017.04.155.

[76] K. Eckhard, X. Chen, F. Turcu, et W. Schuhmann, « Redox competition mode of scanning electrochemical microscopy (RC-SECM) for visualisation of local catalytic activity », *Phys. Chem. Chem. Phys.*, vol. 8, nº 45, p. 5359, 2006, doi: 10.1039/b609511a.

[77] A. Asserghine, M. Medvidović-Kosanović, L. Nagy, R. M. Souto, et G. Nagy, « A study of the electrochemical reactivity of titanium under cathodic polarization by means of combined feedback and redox competition modes of scanning electrochemical microscopy », *Sensors and Actuators B: Chemical*, vol. 320, p. 128339, oct. 2020, doi: 10.1016/j.snb.2020.128339.

[78] C. X. Li, B. Q. Qiu, W. L. Wang, J. L. Zhuang, et J. Tang, « Electrochemical deposition of organic semiconductor thin film and screening by scanning electrochemical microscopy », *Thin Solid Films*, vol. 698, p. 137855, mars 2020, doi: 10.1016/j.tsf.2020.137855.

[79] D. Polcari, P. Dauphin-Ducharme, et J. Mauzeroll, « Scanning Electrochemical Microscopy: A Comprehensive Review of Experimental Parameters from 1989 to 2015 », *Chem. Rev.*, vol. 116, nº 22, p. 13234-13278, nov. 2016, doi: 10.1021/acs.chemrev.6b00067.

[80] L. Han *et al.*, « Direct Nanomachining on Semiconductor Wafer By Scanning Electrochemical Microscopy », *Angew. Chem. Int. Ed.*, vol. 59, nº 47, p. 21129-21134, nov. 2020, doi: 10.1002/anie.202008697.

[81] A. Hamzehloei, S. Zahra Bathaie, et M. F. Mousavi, « Probing redox reaction of azurin protein immobilized on hydroxyl-terminated self-assembled monolayers with different lengths », *Journal of Electroanalytical Chemistry*, vol. 755, p. 27-38, oct. 2015, doi: 10.1016/j.jelechem.2015.07.005.

[82] A. Doménech-Carbó *et al.*, « dsDNA, ssDNA, G-quadruplex DNA, and nucleosomal DNA electrochemical screening using canthin-6-one alkaloid-modified electrodes », *Electrochimica Acta*, vol. 115, p. 546-552, janv. 2014, doi: 10.1016/j.electacta.2013.11.025.

[83] N. M. Jayathilake et D. Koley, « Glucose Microsensor with Covalently Immobilized Glucose Oxidase for Probing Bacterial Glucose Uptake by Scanning Electrochemical Microscopy », *Anal. Chem.*, vol. 92, nº 5, p. 3589-3597, mars 2020, doi: 10.1021/acs.analchem.9b04284.

[84] S. Darvishi *et al.*, « Tape-Stripping Electrochemical Detection of Melanoma », *Anal. Chem.*, vol. 91, nº 20, p. 12900-12908, oct. 2019, doi: 10.1021/acs.analchem.9b02819.

[85] S. Darvishi, H. Pick, E. Oveisi, H. H. Girault, et A. Lesch, « Soft-probe-scanning electrochemical microscopy reveals electrochemical surface reactivity of E. coli biofilms », *Sensors and Actuators B: Chemical*, vol. 334, p. 129669, mai 2021, doi: 10.1016/j.snb.2021.129669.

[86] P. Schwager, H. Bülter, I. Plettenberg, et G. Wittstock, « Review of Local In Situ Probing Techniques for the Interfaces of Lithium-Ion and Lithium-Oxygen Batteries », *Energy Technol.*, vol. 4, nº 12, p. 1472-1485, déc. 2016, doi: 10.1002/ente.201600141.

[87] L. Danis, S. M. Gateman, C. Kuss, S. B. Schougaard, et J. Mauzeroll, « Nanoscale Measurements of Lithium-Ion-Battery Materials using Scanning Probe Techniques », *ChemElectroChem*, vol. 4, nº 1, p. 6-19, janv. 2017, doi: 10.1002/celc.201600571.

[88] X. Zhang, M. Liu, W. Kong, et H. Fan, « Recent advances in solar cells and photo-electrochemical water splitting by scanning electrochemical microscopy », *Front. Optoelectron.*, vol. 11, nº 4, p. 333-347, déc. 2018, doi: 10.1007/s12200-018-0852-7.

[89] J. Park, V. Kumar, X. Wang, P. S. Lee, et W. Kim, « Investigation of Charge Transfer Kinetics at

Carbon/Hydroquinone Interfaces for Redox-Active-Electrolyte Supercapacitors », *ACS Appl. Mater. Interfaces*, vol. 9, nº 39, p. 33728-33734, oct. 2017, doi: 10.1021/acsami.7b06863.

[90] M. K. Dey, P. K. Sahoo, et A. K. Satpati, « Electrochemically deposited layered MnO 2 films for improved supercapacitor », *Journal of Electroanalytical Chemistry*, vol. 788, p. 175-183, mars 2017, doi: 10.1016/j.jelechem.2017.01.063.

[91] W. Schulte *et al.*, « Local Evaluation of Processed Membrane Electrode Assemblies by Scanning Electrochemical Microscopy », *J. Electrochem. Soc.*, vol. 164, nº 7, p. F873-F878, 2017, doi: 10.1149/2.0061709jes.

[92] S. Ben Jadi *et al.*, « Analyses of scanning electrochemical microscopy and electrochemical impedance spectroscopy in direct methanol fuel cells: permeability resistance and proton conductivity of polyaniline modified membrane », *J Solid State Electrochem*, vol. 24, nº 7, p. 1551-1565, juill. 2020, doi: 10.1007/s10008-020-04659-2.

[93] N. Limani, A. Boudet, N. Blanchard, B. Jousselme, et R. Cornut, « Local probe investigation of electrocatalytic activity », *Chem. Sci.*, vol. 12, nº 1, p. 71-98, 2021, doi: 10.1039/D0SC04319B.

[94] P. Hansma, B. Drake, O. Marti, S. Gould, et C. Prater, « The scanning ion-conductance microscope », *Science*, vol. 243, nº 4891, p. 641-643, févr. 1989, doi: 10.1126/science.2464851.

[95] M. Gruening *et al.*, « Automatic Actin Filament Quantification and Cell Shape Modeling of Osteoblasts on Charged Ti Surfaces », *Applied Sciences*, vol. 11, nº 12, p. 5689, juin 2021, doi: 10.3390/app11125689.

[96] J. Rheinlaender, H. Wirbel, et T. E. Schäffer, « Spatial correlation of cell stiffness and traction forces in cancer cells measured with combined SICM and TFM », *RSC Adv.*, vol. 11, nº 23, p. 13951-13956, 2021, doi: 10.1039/D1RA01277K.

[97] C.-C. Chen, Y. Zhou, et L. A. Baker, « Single-Nanopore Investigations with Ion Conductance Microscopy », *ACS Nano*, vol. 5, nº 10, p. 8404-8411, oct. 2011, doi: 10.1021/nn203205s.

[98] N. Ebejer, M. Schnippering, A. W. Colburn, M. A. Edwards, et P. R. Unwin, « Localized High Resolution Electrochemistry and Multifunctional Imaging: Scanning Electrochemical Cell Microscopy », *Anal. Chem.*, vol. 82, nº 22, p. 9141-9145, nov. 2010, doi: 10.1021/ac102191u.

[99] J. Edgecomb, X. Xie, Y. Shao, P. Z. El-Khoury, G. E. Johnson, et V. Prabhakaran, « Mapping Localized Peroxyl Radical Generation on a PEM Fuel Cell Catalyst Using Integrated Scanning Electrochemical Cell Microspectroscopy », *Front. Chem.*, vol. 8, p. 572563, oct. 2020, doi: 10.3389/fchem.2020.572563.

[100] P. Ciocci, J.-F. Lemineur, J.-M. Noël, C. Combellas, et F. Kanoufi, « Differentiating electrochemically active regions of indium tin oxide electrodes for hydrogen evolution and reductive decomposition reactions. An in situ optical microscopy approach », *Electrochimica Acta*, vol. 386, p. 138498, août 2021, doi: 10.1016/j.electacta.2021.138498.

[101] M. Ludwig, C. Kranz, W. Schuhmann, et H. E. Gaub, « Topography feedback mechanism for the scanning electrochemical microscope based on hydrodynamic forces between tip and sample », *Review of Scientific Instruments*, vol. 66, nº 4, p. 2857-2860, avr. 1995, doi: 10.1063/1.1145568.

[102] K. MKelvey, M. A. Edwards, et P. R. Unwin, « Intermittent Contact−Scanning Electrochemical Microscopy (IC−SECM): A New Approach for Tip Positioning and Simultaneous Imaging of Interfacial Topography and Activity », *Anal. Chem.*, vol. 82, nº 15, p. 6334-6337, août 2010, doi: 10.1021/ac101099e.

[103] S. Dieckhöfer, D. Öhl, J. R. C. Junqueira, T. Quast, T. Turek, et W. Schuhmann, « Probing the Local Reaction Environment During High Turnover Carbon Dioxide Reduction with Ag-Based Gas Diffusion Electrodes », *Chem. Eur. J.*, vol. 27, nº 19, p. 5906-5912, avr. 2021, doi: 10.1002/chem.202100387.

[104] I. Schmidt *et al.*, « Spatially Resolved Analysis of Screen Printed Photoanodes of Dye-Sensitized Solar Cells by Scanning Electrochemical Microscopy », *Electrochimica Acta*, vol. 222, p. 735-746, déc. 2016, doi: 10.1016/j.electacta.2016.11.030.

[105] L. I. Tomlinson *et al.*, « Intermittent-contact Scanning Electrochemical Microscopy (IC-SECM) as a Quantitative Probe of Defects in Single Crystal Boron Doped Diamond Electrodes », *Electroanalysis*, vol. 28, nº 10, p. 2297-2302, oct. 2016, doi: 10.1002/elan.201600291.

[106] S. R. Catarelli, D. Lonsdale, L. Cheng, J. Syzdek, et M. Doeff, « Intermittent Contact Alternating Current Scanning Electrochemical Microscopy: A Method for Mapping Conductivities in Solid Li Ion Conducting

Electrolyte Samples », *Front. Energy Res.*, vol. 4, mars 2016, doi: 10.3389/fenrg.2016.00014.

[107] G. Haugstad, *Atomic Force Microscopy: Understanding Basic Modes and Advanced Applications*, Wiley. 2012. [En ligne]. Disponible sur: 10.1002/9781118360668

[108] J. J. Alvear-Daza *et al.*, « Facile photocatalytic immobilization strategy for P-25 TiO2 nanoparticles on low density polyethylene films and their UV-A photo-induced super hydrophilicity and photocatalytic activity », *Catalysis Today*, vol. 372, p. 11-19, juill. 2021, doi: 10.1016/j.cattod.2020.07.029.

[109] S. Toprak Döşlü, A. Döner, et R. Yıldız, « Electrocatalysis property of CuZn electrode with Pt and Ru decoration », *International Journal of Hydrogen Energy*, vol. 46, nº 43, p. 22409-22421, juin 2021, doi: 10.1016/j.ijhydene.2021.04.064.

[110] A. Naeimi, M.-S. Ekrami-Kakhki, et F. Donyagard, « Enhanced electrocatalytic performance of Pt nanoparticles immobilized on novel electrospun PVA@Ni/NiO/Cu complex bio-nanofiber/chitosan based on Calotropis procera plant for methanol electro-oxidation », *International Journal of Hydrogen Energy*, vol. 46, nº 36, p. 18949-18963, mai 2021, doi: 10.1016/j.ijhydene.2021.03.043.

[111] L. Rakočević, I. Srejić, A. Maksić, J. Golubović, et S. Štrbac, « Hydrogen Evolution on Reduced Graphene Oxide-Supported PdAu Nanoparticles », *Catalysts*, vol. 11, nº 4, p. 481, avr. 2021, doi: 10.3390/catal11040481.

[112] F. G. Davia, N. P. Johner, E. J. Calvo, et F. J. Williams, « Growth and electrochemical stability of a layer-by-layer thin film containing tetrasulfonated Fe phthalocyanine », *Journal of Electroanalytical Chemistry*, vol. 877, p. 114485, nov. 2020, doi: 10.1016/j.jelechem.2020.114485.

[113] Y. Bao, M. Kitta, T. Ichii, T. Utsunomiya, et H. Sugimura, « Visualization of solvation structure on $Li_4Ti_5O_{12}$ (111)/ ionic liquid-based electrolyte interface by atomic force microscopy », *Jpn. J. Appl. Phys.*, vol. 60, nº SE, p. SE1004, sept. 2021, doi: 10.35848/1347-4065/abf3a3.

[114] S. Yadav *et al.*, « Interfacial Interactions and Tribological Behavior of Metal-Oxide/2D-Material Contacts », *Tribol Lett*, vol. 69, nº 3, p. 91, sept. 2021, doi: 10.1007/s11249-021-01464-4.

[115] I. Sokolović *et al.*, « Quest for a pristine unreconstructed SrTiO 3 (001) surface: An atomically resolved study via noncontact atomic force microscopy », *Phys. Rev. B*, vol. 103, nº 24, p. L241406, juin 2021, doi: 10.1103/PhysRevB.103.L241406.

[116] M. H. Hassan, M. H. Alkordi, et A. Hassanien, « Probing the conductivity of metal-organic framework-graphene nanocomposite », *Materials Letters*, vol. 246, p. 13-16, juill. 2019, doi: 10.1016/j.matlet.2019.02.124.

[117] Y. Sun, Z. Hu, D. Zhao, et K. Zeng, « Mechanical Properties of Microcrystalline Metal–Organic Frameworks (MOFs) Measured by Bimodal Amplitude Modulated-Frequency Modulated Atomic Force Microscopy », *ACS Appl. Mater. Interfaces*, vol. 9, nº 37, p. 32202-32210, sept. 2017, doi: 10.1021/acsami.7b06809.

[118] T. Morawietz, M. Handl, C. Oldani, K. A. Friedrich, et R. Hiesgen, « Quantitative in Situ Analysis of Ionomer Structure in Fuel Cell Catalytic Layers », *ACS Appl. Mater. Interfaces*, vol. 8, nº 40, p. 27044-27054, oct. 2016, doi: 10.1021/acsami.6b07188.

[119] W. Melitz, J. Shen, A. C. Kummel, et S. Lee, « Kelvin probe force microscopy and its application », *Surface Science Reports*, vol. 66, nº 1, p. 1-27, janv. 2011, doi: 10.1016/j.surfrep.2010.10.001.

[120] H. Masuda, N. Ishida, Y. Ogata, D. Ito, et D. Fujita, « Internal potential mapping of charged solid-state-lithium ion batteries using in situ Kelvin probe force microscopy », *Nanoscale*, vol. 9, nº 2, p. 893-898, 2017, doi: 10.1039/C6NR07971G.

[121] J. Zhu, L. Lu, et K. Zeng, « Nanoscale Mapping of Lithium-Ion Diffusion in a Cathode within an All-Solid-State Lithium-Ion Battery by Advanced Scanning Probe Microscopy Techniques », *ACS Nano*, vol. 7, nº 2, p. 1666-1675, févr. 2013, doi: 10.1021/nn305648j.

[122] H. Zhang, D. Wang, et C. Shen, « In-situ EC-AFM and ex-situ XPS characterization to investigate the mechanism of SEI formation in highly concentrated aqueous electrolyte for Li-ion batteries », *Applied Surface Science*, vol. 507, p. 145059, mars 2020, doi: 10.1016/j.apsusc.2019.145059.

[123] K. Chennit *et al.*, « Electrochemical Imaging of Dense Molecular Nanoarrays », *Anal. Chem.*, vol. 89, nº 20, p. 11061-11069, oct. 2017, doi: 10.1021/acs.analchem.7b03111.

[124] S. Kolagatla, P. Subramanian, et A. Schechter, « Catalytic current mapping of oxygen reduction on isolated Pt particles by atomic force microscopy-scanning electrochemical microscopy », *Applied Catalysis B: Environmental*, vol. 256, p. 117843, nov. 2019, doi: 10.1016/j.apcatb.2019.117843.

[125] K. Mahankali, N. K. Thangavel, et L. M. Reddy Arava, « In Situ Electrochemical Mapping of Lithium–Sulfur Battery Interfaces Using AFM–SECM », *Nano Lett.*, vol. 19, nº 8, p. 5229-5236, août 2019, doi: 10.1021/acs.nanolett.9b01636.

[126] L. Nault *et al.*, « Electrochemical Atomic Force Microscopy Imaging of Redox-Immunomarked Proteins on Native Potyviruses: From Subparticle to Single-Protein Resolution », *ACS Nano*, vol. 9, nº 5, p. 4911-4924, mai 2015, doi: 10.1021/acsnano.5b00952.

[127] P. Knittel, H. Zhang, C. Kranz, G. G. Wallace, et M. J. Higgins, « Probing the PEDOT:PSS/cell interface with conductive colloidal probe AFM-SECM », *Nanoscale*, vol. 8, nº 8, p. 4475-4481, 2016, doi: 10.1039/C5NR07155K.

[128] K. Torbensen *et al.*, « Immuno-Based Molecular Scaffolding of Glucose Dehydrogenase and Ferrocene Mediator on *fd* Viral Particles Yields Enhanced Bioelectrocatalysis », *ACS Catal.*, vol. 9, nº 6, p. 5783-5796, juin 2019, doi: 10.1021/acscatal.9b01263.

[129] X. Shi, W. Qing, T. Marhaba, et W. Zhang, « Atomic force microscopy - Scanning electrochemical microscopy (AFM-SECM) for nanoscale topographical and electrochemical characterization: Principles, applications and perspectives », *Electrochimica Acta*, vol. 332, p. 135472, févr. 2020, doi: 10.1016/j.electacta.2019.135472.

[130] G. Zampardi *et al.*, « Combined AFM/SECM Investigation of the Solid Electrolyte Interphase in Li-Ion Batteries », *ChemElectroChem*, vol. 2, nº 10, p. 1607-1611, oct. 2015, doi: 10.1002/celc.201500085.

[131] T. S. Watkins *et al.*, « A combined SECM and electrochemical AFM approach to probe interfacial processes affecting molecular reactivity at redox flow battery electrodes », *J. Mater. Chem. A*, vol. 8, nº 31, p. 15734-15745, 2020, doi: 10.1039/D0TA00836B.

[132] A. K. Satpati, N. Arroyo-Currás, L. Ji, E. T. Yu, et A. J. Bard, « Electrochemical Monitoring of TiO_2 Atomic Layer Deposition by Chronoamperometry and Scanning Electrochemical Microscopy », *Chem. Mater.*, vol. 25, nº 21, p. 4165-4172, nov. 2013, doi: 10.1021/cm401635v.

[133] C. L. Bentley *et al.*, « Correlating the Local Electrocatalytic Activity of Amorphous Molybdenum Sulfide Thin Films with Microscopic Composition, Structure, and Porosity », *ACS Appl. Mater. Interfaces*, vol. 12, nº 39, p. 44307-44316, sept. 2020, doi: 10.1021/acsami.0c11759.

[134] J. Jiang *et al.*, « Nanoelectrical and Nanoelectrochemical Imaging of Pt/p-Si and Pt/p^+-Si Electrodes », *ChemSusChem*, vol. 10, nº 22, p. 4657-4663, nov. 2017, doi: 10.1002/cssc.201700893.

[135] O. Henrotte, « Méthode pour l'analyse de l'activité de la réduction de l'oxygène de catalyseurs sans métaux nobles par microscopie électrochimique. », UniversitéParisSaclay (COmUE), 2018.

[136] P. Klapetek et I. Ohlídal, « Theoretical analysis of the atomic force microscopy characterization of columnar thin films », *Ultramicroscopy*, vol. 94, nº 1, p. 19-29, janv. 2003, doi: 10.1016/S0304-3991(02)00159-6.

[137] D. R. Lide, G. Baysinger, S. Chemistry, L. I. Berger, R. N. Goldberg, et H. V. Kehiaian, « CRC Handbook of Chemistry and Physics », p. 2661.

[138] Juhyoun. Kwak et A. J. Bard, « Scanning electrochemical microscopy. Theory of the feedback mode », *Anal. Chem.*, vol. 61, nº 11, p. 1221-1227, juin 1989, doi: 10.1021/ac00186a009.

[139] P. R. Unwin et A. J. Bard, « Scanning electrochemical microscopy. 9. Theory and application of the feedback mode to the measurement of following chemical reaction rates in electrode processes », *J. Phys. Chem.*, vol. 95, nº 20, p. 7814-7824, oct. 1991, doi: 10.1021/j100173a049.

[140] A. J. Bard, M. V. Mirkin, P. R. Unwin, et D. O. Wipf, « Scanning electrochemical microscopy. 12. Theory and experiment of the feedback mode with finite heterogeneous electron-transfer kinetics and arbitrary substrate size », *J. Phys. Chem.*, vol. 96, nº 4, p. 1861-1868, févr. 1992, doi: 10.1021/j100183a064.

[141] C. Lefrou, « A unified new analytical approximation for positive feedback currents with a microdisk SECM tip », *Journal of Electroanalytical Chemistry*, vol. 592, nº 1, p. 103-112, juill. 2006, doi: 10.1016/j.jelechem.2006.05.003.

[142] S. Daniele, I. Ciani, et D. Battistel, « Effect of the Insulating Shield Thickness on the Steady-State Diffusion-Limiting Current of Sphere Cap Microelectrodes », *Anal. Chem.*, vol. 80, nº 1, p. 253-259, janv. 2008, doi: 10.1021/ac701631y.

[143] D. A. Treichel, M. V. Mirkin, et A. J. Bard, « Scanning Electrochemical Microscopy. 27. Application of a Simplified Treatment of an Irreversible Homogeneous Reaction following Electron Transfer to the Oxidative Dimerization of 4-Nitrophenolate in Acetonitrile », *J. Phys. Chem.*, vol. 98, nº 22, p. 5751-5757, juin 1994, doi: 10.1021/j100073a030.

[144] S. K. Haram et A. J. Bard, « Scanning Electrochemical Microscopy. 42. Studies of the Kinetics and Photoelectrochemistry of Thin Film CdS/Electrolyte Interfaces », *J. Phys. Chem. B*, vol. 105, nº 34, p. 8192-8195, août 2001, doi: 10.1021/jp011068j.

[145] Y. Shen, M. Träuble, et G. Wittstock, « Electrodeposited noble metal particles in polyelectrolyte multilayer matrix as electrocatalyst for oxygen reduction studied using SECM », *Phys. Chem. Chem. Phys.*, vol. 10, nº 25, p. 3635, 2008, doi: 10.1039/b802688b.

[146] J.-F. Masson, C. Kranz, et B. Mizaikoff, « Modeling the Response Function of Dual-Enzyme Microbiosensors », *Anal. Chem.*, vol. 79, nº 22, p. 8531-8538, nov. 2007, doi: 10.1021/ac071090u.

[147] M. Burchardt et G. Wittstock, « Kinetic studies of glucose oxidase in polyelectrolyte multilayer films by means of scanning electrochemical microscopy (SECM) », *Bioelectrochemistry*, vol. 72, nº 1, p. 66-76, févr. 2008, doi: 10.1016/j.bioelechem.2007.11.010.

[148] Y. Shen, M. Träuble, et G. Wittstock, « Detection of Hydrogen Peroxide Produced during Electrochemical Oxygen Reduction Using Scanning Electrochemical Microscopy », *Anal. Chem.*, vol. 80, nº 3, p. 750-759, févr. 2008, doi: 10.1021/ac0711889.

[149] A. Dobrzeniecka *et al.*, « Evaluation of kinetic constants on porous, non-noble catalyst layers for oxygen reduction—A comparative study between SECM and hydrodynamic methods », *Catalysis Today*, vol. 262, p. 74-81, mars 2016, doi: 10.1016/j.cattod.2015.07.043.

[150] G. Seiffarth, M. Steimecke, T. Walther, M. Kühhirt, S. Rümmler, et M. Bron, « Mixed Transition Metal Oxide Supported on Nitrogen Doped Carbon Nanotubes – a Simple Bifunctional Electrocatalyst Studied with Scanning Electrochemical Microscopy », *Electroanalysis*, p. 11, 2016.

[151] R. Cornut, A. Bhasin, S. Lhenry, M. Etienne, et C. Lefrou, « Accurate and Simplified Consideration of the Probe Geometrical Defaults in Scanning Electrochemical Microscopy: Theoretical and Experimental Investigations », *Anal. Chem.*, vol. 83, nº 24, p. 9669-9675, déc. 2011, doi: 10.1021/ac2026018.

[152] R. Astrauskas, F. Ivanauskas, I. Morkvenaite-Vilkonciene, et A. Ramanavicius, « Mathematical Modelling of the Influence of Ultra-micro Electrode Geometry on Approach Curves Registered by Scanning Electrochemical Microscopy », *Electroanalysis*, vol. 31, nº 11, p. 2214-2223, nov. 2019, doi: 10.1002/elan.201900313.

[153] F. P. Filice, M. S. M. Li, J. D. Henderson, et Z. Ding, « Three-Dimensional Electrochemical Functionality of an Interdigitated Array Electrode by Scanning Electrochemical Microscopy », *J. Phys. Chem. C*, vol. 119, nº 37, p. 21473-21482, sept. 2015, doi: 10.1021/acs.jpcc.5b05568.

[154] M. R. Nellist *et al.*, « Atomic force microscopy with nanoelectrode tips for high resolution electrochemical, nanoadhesion and nanoelectrical imaging », *Nanotechnology*, vol. 28, nº 9, p. 095711, mars 2017, doi: 10.1088/1361-6528/aa5839.

[155] J. Rheinlaender et T. E. Schäffer, « An Accurate Model for the Ion Current–Distance Behavior in Scanning Ion Conductance Microscopy Allows for Calibration of Pipet Tip Geometry and Tip–Sample Distance », *Anal. Chem.*, vol. 89, nº 21, p. 11875-11880, nov. 2017, doi: 10.1021/acs.analchem.7b03871.

[156] L. I. Stephens et J. Mauzeroll, « Altered Spatial Resolution of Scanning Electrochemical Microscopy Induced by Multifunctional Dual-Barrel Microelectrodes », *Anal. Chem.*, vol. 90, nº 11, p. 6796-6803, juin 2018, doi: 10.1021/acs.analchem.8b00821.

[157] F. Li et P. R. Unwin, « Scanning Electrochemical Microscopy (SECM) of Photoinduced Electron Transfer Kinetics at Liquid/Liquid Interfaces », *J. Phys. Chem. C*, vol. 119, nº 8, p. 4031-4043, févr. 2015, doi: 10.1021/jp510333d.

[158] L. Yao, K. Chen, et B. Su, « Unraveling Mass and Electron Transfer Kinetics at Silica Nanochannel

Membrane Modified Electrodes by Scanning Electrochemical Microscopy », *Anal. Chem.*, vol. 91, nº 24, p. 15436-15443, déc. 2019, doi: 10.1021/acs.analchem.9b03044.

[159] Md. S. Hossain *et al.*, « Effective Mass Transport Properties in Lithium Battery Electrodes », *ACS Appl. Energy Mater.*, vol. 3, nº 1, p. 440-446, janv. 2020, doi: 10.1021/acsaem.9b01695.

[160] D. T. Jantz, T. E. Seuferling, et K. C. Leonard, « Numerical Deconvolution of Surface Interrogation Scanning Electrochemical Microscopy Experiments on Platinum During Hydrogen Evolution », *ChemElectroChem*, vol. 7, nº 24, p. 4863-4872, déc. 2020, doi: 10.1002/celc.202001082.

[161] M. A. Brites Helú et J. L. Fernández, « Analysis of the hydrogen electrode reaction mechanism in thin-layer cells. 3. Study of hydrogen electro-oxidation by scanning electrochemical microscopy », *Journal of Electroanalytical Chemistry*, vol. 784, p. 33-40, janv. 2017, doi: 10.1016/j.jelechem.2016.11.065.

[162] Z. Liang, H. S. Ahn, et A. J. Bard, « A Study of the Mechanism of the Hydrogen Evolution Reaction on Nickel by Surface Interrogation Scanning Electrochemical Microscopy », *J. Am. Chem. Soc.*, vol. 139, nº 13, p. 4854-4858, avr. 2017, doi: 10.1021/jacs.7b00279.

[163] Q. Zhang, Z. Ye, Z. Zhu, X. Liu, J. Zhang, et F. Cao, « Separation and kinetic study of iron corrosion in acidic solution via a modified tip generation/substrate collection mode by SECM », *Corrosion Science*, vol. 139, p. 403-409, juill. 2018, doi: 10.1016/j.corsci.2018.05.021.

[164] L. C. Abodi *et al.*, « Simulated and measured response of oxygen SECM-measurements in presence of a corrosion process », *Electrochimica Acta*, vol. 146, p. 556-563, nov. 2014, doi: 10.1016/j.electacta.2014.09.010.

[165] F. P. Filice, M. S. M. Li, et Z. Ding, « Simulation Assisted Nanoscale Imaging of Single Live Cells with Scanning Electrochemical Microscopy », *Adv. Theory Simul.*, vol. 2, nº 2, p. 1800124, févr. 2019, doi: 10.1002/adts.201800124.

[166] C. S. Santos *et al.*, « Unveiling the contribution of the reproductive system of individual Caenorhabditis elegans on oxygen consumption by single-point scanning electrochemical microscopy measurements », *Analytica Chimica Acta*, vol. 1146, p. 88-97, févr. 2021, doi: 10.1016/j.aca.2020.12.030.

[167] R. Mukomoto *et al.*, « Oxygen consumption rate of tumour spheroids during necrotic-like core formation », *Analyst*, vol. 145, nº 19, p. 6342-6348, 2020, doi: 10.1039/D0AN00979B.

[168] F. Ivanauskas, I. Morkvenaite-Vilkonciene, R. Astrauskas, et A. Ramanavicius, « Modelling of Scanning Electrochemical Microscopy at Redox Competition Mode Using Diffusion and Reaction Equations », *Electrochimica Acta*, vol. 222, p. 347-354, déc. 2016, doi: 10.1016/j.electacta.2016.10.179.

[169] R. Čiegis, P. Katauskis, et V. Skakauskas, « Modelling competition of the enzyme-catalysed glucose oxidation and redox reactions in scanning electrochemical microscopy », *Reaction Kinetics, Mechanisms and Catalysis*, vol. 127, p. 543-559, 2019.

[170] C. M. Sánchez-Sánchez, J. Rodríguez-López, et A. J. Bard, « Scanning Electrochemical Microscopy. 60. Quantitative Calibration of the SECM Substrate Generation/Tip Collection Mode and Its Use for the Study of the Oxygen Reduction Mechanism », *Anal. Chem.*, vol. 80, nº 9, p. 3254-3260, mai 2008, doi: 10.1021/ac702453n.

[171] C. M. Sánchez-Sánchez et A. J. Bard, « Hydrogen Peroxide Production in the Oxygen Reduction Reaction at Different Electrocatalysts as Quantified by Scanning Electrochemical Microscopy », *Anal. Chem.*, vol. 81, nº 19, p. 8094-8100, oct. 2009, doi: 10.1021/ac901291v.

[172] A. Dobrzeniecka *et al.*, « Application of SECM in tracing of hydrogen peroxide at multicomponent non-noble electrocatalyst films for the oxygen reduction reaction », *Catalysis Today*, vol. 202, p. 55-62, mars 2013, doi: 10.1016/j.cattod.2012.03.060.

[173] A. Baricci, A. Bisello, A. Serov, M. Odgaard, P. Atanassov, et A. Casalegno, « Analysis of the effect of catalyst layer thickness on the performance and durability of platinum group metal-free catalysts for polymer electrolyte membrane fuel cells », *Sustainable Energy Fuels*, vol. 3, nº 12, p. 3375-3386, 2019, doi: 10.1039/C9SE00252A.

[174] P.-C. Sui, X. Zhu, et N. Djilali, « Modeling of PEM Fuel Cell Catalyst Layers: Status and Outlook », *Electrochem. Energ. Rev.*, vol. 2, nº 3, p. 428-466, sept. 2019, doi: 10.1007/s41918-019-00043-5.

[175] B. Bai et Y.-T. Chen, « Simulation of the Oxygen Reduction Reaction (ORR) Inside the Cathode

Catalyst Layer (CCL) of Proton Exchange Membrane Fuel Cells Using the Kinetic Monte Carlo Method », *Energies*, vol. 11, nº 10, p. 2529, sept. 2018, doi: 10.3390/en11102529.

[176] A. Pournemat, F. Wilhelm, et J. Scholta, « Effect of Current Density on the Dynamical Evolution of Liquid Water Distribution within the Gas Diffusion Layers of PEMFC Employing a Multi-Timescale Kinetic Monte Carlo Method », *J. Electrochem. Soc.*, vol. 166, nº 4, p. F334-F342, 2019, doi: 10.1149/2.0981904jes.

[177] K. N. Kim, J. H. Kang, S. G. Lee, J. H. Nam, et C.-J. Kim, « Lattice Boltzmann simulation of liquid water transport in microporous and gas diffusion layers of polymer electrolyte membrane fuel cells », *Journal of Power Sources*, vol. 278, p. 703-717, mars 2015, doi: 10.1016/j.jpowsour.2014.12.044.

[178] G. R. Molaeimanesh, M. A. Bamdehz, et M. Nazemian, « Impact of catalyst layer morphology on the performance of PEM fuel cell cathode via lattice Boltzmann simulation », *International Journal of Hydrogen Energy*, vol. 43, p. 20959-20975, 2018, doi: https://doi.org/10.1016/j.ijhydene.2018.09.076.

[179] R. Bradean, K. Promislow, et B. Wetton, « TRANSPORT PHENOMENA IN THE POROUS CATHODE OF A PROTON EXCHANGE MEMBRANE FUEL CELL », *Numer. Heat Transf. Part A Appl*, vol. 42, p. 121-138, 2002, doi: https :// doi.org/10.1080/10407 78029 00594 68.

[180] A. A. Kulikovsky, « Quasi-3D Modeling of Water Transport in Polymer Electrolyte Fuel Cells », *J. Electrochem. Soc.*, vol. 150, nº 11, p. A1432, 2003, doi: 10.1149/1.1611489.

[181] B. Randrianarizafy, P. Schott, M. Chandesris, M. Gerard, et Y. Bultel, « Design optimization of rib/channel patterns in a PEMFC through performance heterogeneities modelling », *International Journal of Hydrogen Energy*, vol. 43, nº 18, p. 8907-8926, mai 2018, doi: 10.1016/j.ijhydene.2018.03.036.

[182] D. Zhou, T. Trang Nguyen, E. Breaz, D. Zhao, S. Clénet, et F. Gao, « Global parameters sensitivity analysis and development of a two-dimensional real-time model of proton-exchange-membrane fuel cells », *Energy Conversion and Management*, vol. 162, p. 276-292, avr. 2018, doi: 10.1016/j.enconman.2018.02.036.

[183] S. Mohanty, A. N. Desai, S. Singh, V. Ramadesigan, et S. M, « Effects of the membrane thickness and ionomer volume fraction on the performance of PEMFC with U-shaped serpentine channel », *International Journal of Hydrogen Energy*, vol. 46, nº 39, p. 20650-20663, juin 2021, doi: 10.1016/j.ijhydene.2021.03.252.

[184] H. Zhang, M. A. Rahman, F. Mojica, P. Sui, et P. A. Chuang, « A comprehensive two-phase proton exchange membrane fuel cell model coupled with anisotropic properties and mechanical deformation of the gas diffusion layer », *Electrochimica Acta*, vol. 382, p. 138273, juin 2021, doi: 10.1016/j.electacta.2021.138273.

[185] M. S. Ismail, D. B. Ingham, L. Ma, K. J. Hughes, et M. Pourkashanian, « Effects of catalyst agglomerate shape in polymer electrolyte fuel cells investigated by a multi-scale modelling framework », *Energy*, vol. 122, p. 420-430, mars 2017, doi: 10.1016/j.energy.2017.01.092.

[186] L. Xing, M. Mamlouk, et K. Scott, « A two dimensional agglomerate model for a proton exchange membrane fuel cell », *Energy*, vol. 61, p. 196-210, nov. 2013, doi: 10.1016/j.energy.2013.08.026.

[187] S. Kamarajugadda et S. Mazumder, « Generalized flooded agglomerate model for the cathode catalyst layer of a polymer electrolyte membrane fuel cell », *Journal of Power Sources*, vol. 208, p. 328-339, juin 2012, doi: 10.1016/j.jpowsour.2012.02.063.

[188] S. Li, J. Yuan, M. Andersson, G. Xie, et B. Sundén, « Wavy Surface Cathode Gas Flow Channel Effects on Transport Processes in a Proton Exchange Membrane Fuel Cell », *Journal of Electrochemical Energy Conversion and Storage*, vol. 14, nº 3, p. 031007, août 2017, doi: 10.1115/1.4036810.

[189] C. Cosse, M. Schumann, F. Grumm, D. Becker, et D. Schulz, « Numerical Investigation of PEMFC Short-Circuit Behaviour Using an Agglomerate Model Approach », *Energies*, vol. 13, nº 16, p. 4108, août 2020, doi: 10.3390/en13164108.

[190] R. M. Darling, « A Hierarchical Model for Oxygen Transport in Agglomerates in the Cathode Catalyst Layer of a Polymer-Electrolyte Fuel Cell », *J. Electrochem. Soc.*, vol. 165, nº 9, p. F571-F580, 2018, doi: 10.1149/2.1231807jes.

[191] J. Liang, Y. Li, R. Wang, et J. Jiang, « Cross-dimensional model of the oxygen transport behavior in low-Pt proton exchange membrane fuel cells », *Chemical Engineering Journal*, vol. 400, p. 125796, nov.

2020, doi: 10.1016/j.cej.2020.125796.
[192] I. V. Zenyuk, P. K. Das, et A. Z. Weber, « Understanding Impacts of Catalyst-Layer Thickness on Fuel-Cell Performance via Mathematical Modeling », *J. Electrochem. Soc.*, vol. 163, nº 7, p. F691-F703, 2016, doi: 10.1149/2.1161607jes.
[193] L. Hao, K. Moriyama, W. Gu, et C.-Y. Wang, « Modeling and Experimental Validation of Pt Loading and Electrode Composition Effects in PEM Fuel Cells », *J. Electrochem. Soc.*, vol. 162, nº 8, p. F854-F867, 2015, doi: 10.1149/2.0221508jes.
[194] M. Hosseini, H. H. Afrouzi, H. Arasteh, et D. Toghraie, « Energy analysis of a proton exchange membrane fuel cell (PEMFC) with an open-ended anode using agglomerate model: A CFD study », *Energy*, vol. 188, p. 116090, déc. 2019, doi: 10.1016/j.energy.2019.116090.
[195] K. J. Lange, P.-C. Sui, et N. Djilali, « Pore scale modeling of a proton exchange membrane fuel cell catalyst layer: Effects of water vapor and temperature », *Journal of Power Sources*, vol. 196, nº 6, p. 3195-3203, mars 2011, doi: 10.1016/j.jpowsour.2010.11.118.
[196] L. Holzer *et al.*, « Microstructure-property relationships in a gas diffusion layer (GDL) for Polymer Electrolyte Fuel Cells, Part II: pressure-induced water injection and liquid permeability », *Electrochimica Acta*, vol. 241, p. 414-432, juill. 2017, doi: 10.1016/j.electacta.2017.04.141.
[197] F. C. Cetinbas, R. K. Ahluwalia, N. N. Kariuki, V. De Andrade, et D. J. Myers, « Effects of Porous Carbon Morphology, Agglomerate Structure and Relative Humidity on Local Oxygen Transport Resistance », *J. Electrochem. Soc.*, vol. 167, nº 1, p. 013508, 2020, doi: 10.1149/2.0082001JES.
[198] Y. Gao, W. Qu, et R. Zhu, « Impact of ionomer film on effective transport properties and performance of cathode catalyst layer of proton-exchange membrane fuel cells », *Ionics*, vol. 26, nº 7, p. 3425-3435, juill. 2020, doi: 10.1007/s11581-020-03524-6.
[199] M. Barreiros Salvado, P. Schott, L. Guétaz, M. Gerard, T. David, et Y. Bultel, « Towards the understanding of transport limitations in a proton-exchange membrane fuel cell catalyst layer: Performing agglomerate scale direct numerical simulations on electron-microscopy-based geometries », *Journal of Power Sources*, vol. 482, p. 228893, janv. 2021, doi: 10.1016/j.jpowsour.2020.228893.
[200] N. Ramaswamy *et al.*, « High-Current Density Durability of Pt/C and PtCo/C Catalysts at Similar Particle Sizes in PEMFCs », *J. Electrochem. Soc.*, vol. 168, nº 2, p. 024519, févr. 2021, doi: 10.1149/1945-7111/abe5ea.
[201] M. A. Rahman, F. Mojica, M. Sarker, et P.-Y. A. Chuang, « Development of 1-D multiphysics PEMFC model with dry limiting current experimental validation », *Electrochimica Acta*, vol. 320, p. 134601, oct. 2019, doi: 10.1016/j.electacta.2019.134601.
[202] M. Sajid Hossain, B. Shabani, et C. P. Cheung, « Enhanced gas flow uniformity across parallel channel cathode flow field of Proton Exchange Membrane fuel cells », *International Journal of Hydrogen Energy*, vol. 42, nº 8, p. 5272-5283, févr. 2017, doi: 10.1016/j.ijhydene.2016.11.042.
[203] S. Barati, B. Khoshandam, et M. M. Ghazi, « An investigation of channel blockage effects on hydrogen mass transfer in a proton exchange membrane fuel cell with various geometries and optimization by response surface methodology », *International Journal of Hydrogen Energy*, vol. 43, nº 48, p. 21928-21939, nov. 2018, doi: 10.1016/j.ijhydene.2018.10.032.
[204] G. A. Futter, P. Gazdzicki, K. A. Friedrich, A. Latz, et T. Jahnke, « Physical modeling of polymer-electrolyte membrane fuel cells: Understanding water management and impedance spectra », *Journal of Power Sources*, vol. 391, p. 148-161, juill. 2018, doi: 10.1016/j.jpowsour.2018.04.070.
[205] S. I. Nefedkin, M. A. Klimova, V. S. Glasov, V. I. Pavlov, et Y. V. Tolmachev, « Effect of the corrugated bipolar plate design on the self-humidification of a high power density PEMFC stack for UAVs », *Fuel Cells*, p. fuce.202000163, avr. 2021, doi: 10.1002/fuce.202000163.
[206] Y. Cai, D. Wu, J. Sun, et B. Chen, « The effect of cathode channel blockages on the enhanced mass transfer and performance of PEMFC », *Energy*, vol. 222, p. 119951, mai 2021, doi: 10.1016/j.energy.2021.119951.
[207] J. Shen, Z. Tu, et S. H. Chan, « Effect of gas purging on the performance of a proton exchange membrane fuel cell with dead-ended anode and cathode », *Int J Energy Res*, p. er.6757, avr. 2021, doi:

10.1002/er.6757.
[208] Y. Liu, S. Bai, P. Wei, P. Pei, S. Yao, et H. Sun, « Numerical and Experimental Investigation of the Asymmetric Humidification and Dynamic Temperature in Proton Exchange Membrane Fuel Cell », *Fuel Cells*, vol. 20, nº 1, p. 48-59, févr. 2020, doi: 10.1002/fuce.201900140.
[209] N. D. Leonard, K. Artyushkova, B. Halevi, A. Serov, P. Atanassov, et S. C. Barton, « Modeling of Low-Temperature Fuel Cell Electrodes Using Non-Precious Metal Catalysts », *J. Electrochem. Soc.*, vol. 162, nº 10, p. F1253-F1261, 2015, doi: 10.1149/2.0311510jes.
[210] R. Pavlicek *et al.*, « Resolving Challenges of Mass Transport in Non Pt-Group Metal Catalysts for Oxygen Reduction in Proton Exchange Membrane Fuel Cells », *J. Electrochem. Soc.*, vol. 165, nº 9, p. F589-F596, 2018, doi: 10.1149/2.0141809jes.
[211] L. Xing, « An agglomerate model for PEM fuel cells operated with non-precious carbon-based ORR catalysts », *Chemical Engineering Science*, vol. 179, p. 198-213, avr. 2018, doi: 10.1016/j.ces.2018.01.026.
[212] J. Liu, P. A. García-Salaberri, et I. V. Zenyuk, « Bridging Scales to Model Reactive Diffusive Transport in Porous Media », *J. Electrochem. Soc.*, vol. 167, nº 1, p. 013524, janv. 2020, doi: 10.1149/2.0242001JES.
[213] J. B. Young et B. Todd, « Modelling of multi-component gas flows in capillaries and porous solids », *International Journal of Heat and Mass Transfer*, vol. 48, nº 25-26, p. 5338-5353, déc. 2005, doi: 10.1016/j.ijheatmasstransfer.2005.07.034.
[214] G. Lin et T. V. Nguyen, « A Two-Dimensional Two-Phase Model of a PEM Fuel Cell », *J. Electrochem. Soc.*, vol. 153, nº 2, p. A372, 2006, doi: 10.1149/1.2142267.
[215] M. J. Lampinen et M. Fomino, « Analysis of Free Energy and Entropy Changes for Half-Cell Reactions », *J. Electrochem. Soc.*, vol. 140, nº 12, p. 3537-3546, déc. 1993, doi: 10.1149/1.2221123.
[216] T. Bednarek et G. Tsotridis, « Issues associated with modelling of proton exchange membrane fuel cell by computational fluid dynamics », *Journal of Power Sources*, vol. 343, p. 550-563, mars 2017, doi: 10.1016/j.jpowsour.2017.01.059.
[217] M. Arif, S. C. P. Cheung, et J. Andrews, « Different Approaches Used for Modeling and Simulation of Polymer Electrolyte Membrane Fuel Cells: A Review », *Energy Fuels*, vol. 34, nº 10, p. 11897-11915, oct. 2020, doi: 10.1021/acs.energyfuels.0c02414.
[218] M. Ohenoja et K. Leiviskä, « Observations on the Parameter Estimation Problem of Polymer Electrolyte Membrane Fuel Cell Polarization Curves », *Fuel Cells*, vol. 20, nº 5, p. 516-526, oct. 2020, doi: 10.1002/fuce.201900155.
[219] R. B. Bird, W. E. Stewart, et E. N. Lightfoot, *Transport phenomena*, 2nd, Wiley international ed éd. New York: J. Wiley, 2002.
[220] N. Ramaswamy *et al.*, « Editors' Choice—Ionomer Side Chain Length and Equivalent Weight Impact on High Current Density Transport Resistances in PEMFC Cathodes », *J. Electrochem. Soc.*, vol. 168, nº 2, p. 024518, févr. 2021, doi: 10.1149/1945-7111/abe5eb.
[221] X. Wan, X. Liu, et J. Shui, « Stability of PGM-free fuel cell catalysts: Degradation mechanisms and mitigation strategies », *Progress in Natural Science: Materials International*, vol. 30, nº 6, p. 721-731, déc. 2020, doi: 10.1016/j.pnsc.2020.08.010.
[222] R. N. Itoe, G. D. Wesson, et E. E. Kalu, « Evaluation of Oxygen Transport Parameters in H2 SO4 - CH3 OH Mixtures Using Electrochemical Methods », *Journal of The Electrochemical Society*, p. 7, 2000.
[223] C. G. Zoski, *Handbook of Electrochemistry*, Elsevier Science. Amsterdam, 2007.
[224] A. Ø. Tjell et K. Almdal, « Diffusion rate of hydrogen peroxide through water-swelled polyurethane membranes », *Sensing and Bio-Sensing Research*, vol. 21, p. 35-39, nov. 2018, doi: 10.1016/j.sbsr.2018.10.001.

université PARIS-SACLAY
ÉCOLE DOCTORALE
Sciences Chimiques: Molécules, Matériaux, Instrumentation et Biosystèmes (2MIB)

Titre : Etude à l'échelle de l'agglomérat de catalyseurs sans platine pour l'ORR : caractérisations à sonde locale et modélisation en pile

Mots clés : PEMFC, Catalyseurs sans platine pour l'ORR, Agglomérats, SECM, AFM, Modélisation

Résumé : Les véhicules électriques à pile à combustible font partie des solutions envisagées pour remplacer les actuels et polluants véhicules thermiques. Cependant, la réduction de leur coût nécessite de développer des catalyseurs sans platine qui entraînent des problématiques liées à leur intégration au sein des piles à combustible de type PEMFC. Ces nouveaux matériaux forment des couches catalytiques épaisses au sein desquelles le transport des espèces électroactives est délicat. L'agglomérat notamment, est une structure clé dont la maîtrise pourrait mener à une meilleure utilisation des sites catalytiques et donc à de meilleures performances en pile. Un besoin de nouvelles techniques de caractérisation se fait ressentir, afin de pouvoir étudier directement les catalyseurs à l'échelle de l'agglomérat.
Nous proposons dans cette thèse d'étudier des matériaux sans platine pour l'ORR à l'échelle de l'agglomérat à l'aide de deux techniques de caractérisation à sonde locale : la microscopie électrochimique à balayage (SECM) et la microscopie à force atomique (AFM). Ces deux techniques permettent de relier expérimentalement l'activité catalytique d'un matériau à son état d'agglomération. Un protocole de caractérisation est développé et plusieurs catalyseurs fournis par les partenaires du projet européen PEGASUS sont étudiés afin de comparer leurs performances.
De plus, caractériser le matériau à l'échelle de l'agglomérat permet d'accéder à ses propriétés catalytiques intrinsèques. Une méthode pour extraire des paramètres cinétiques à partir des mesures SECM et à l'aide d'un modèle numérique est donc mise en place. La densité de courant d'échange et la sélectivité d'un catalyseur sont déterminées et comparées à la littérature. Une résistance ohmique entraînant d'importantes pertes de performance est mise en évidence et interprétée comme un phénomène local de chute ohmique à l'intérieur des agglomérats.
Enfin, un modèle numérique de pile à combustible incluant les paramètres déterminés par SECM est développé afin d'étudier les paramètres d'agglomérat et de couche active influençant les performances globales en pile. Ce modèle confirme l'importance de contrôler la structure des agglomérats pour optimiser les performances.

Title : Investigation of platinum-free ORR catalysts at agglomerate scale: from local probe characterizations to modeling studies

Keywords : PEMFC, Platinum-free ORR catalysts, Agglomerates, SECM, AFM, Modeling

Abstract : Fuel cell electric vehicles are envisioned to take part in the replacement of the current carbon-emitting thermal vehicles. However, the reduction of their cost implies the development of platinum-free catalysts, which involve specific issues concerning their integration into the PEMFC fuel cells. Notably, these new materials form thick catalyst layers in which the transportation of the electroactive species needs to be carefully managed. The agglomerate is a key feature affecting the accessibility of the active sites and there is a need to develop characterization techniques enabling to study catalytic materials directly at the scale of the agglomerate.
In this thesis, we propose to study platinum-free materials for ORR at agglomerate scale with two local probe characterization techniques: scanning electrochemical microscopy (SECM) and atomic force microscopy (AFM). These two techniques enable to link experimentally the electrocatalytic activity of a material to its agglomeration state. A protocol of characterization is developed and several platinum-free catalysts provided by partners of the European project PEGASUS are studied in order to compare their performances.
Moreover, characterizing a material at agglomerate scale gives access to its intrinsic catalytic properties. Thus, a method for extracting kinetic parameters from the SECM measurements with the help of numerical modeling is developed. The exchange current density and the selectivity of the catalyst are determined and compared to the literature. An ohmic resistance leading to important performance losses is brought to light and interpreted as local ohmic drop at the catalyst agglomerates.
Finally, a numerical model at single cell scale including the parameters determined with SECM is built in order to study the catalyst layer and agglomerate parameters affecting the global cell performance. This model confirms the importance of controlling the agglomerate structure in order to optimize the global performance in a fuel cell.

Maison du doctorat de l'Université Paris-Saclay
2ème étage aile ouest, Ecole normale supérieure Paris-Saclay
4 avenue des Sciences,
91190 Gif sur Yvette, France